Experiments on spontaneous Rayleigh-Brillouin scattering in air

Dissertation

zur Erlangung des akademischen Grades
doctor rerum naturalium (Dr. rer. nat.)

vorgelegt dem Rat der Physikalisch-Astronomischen Fakultät
der Friedrich-Schiller-Universität Jena

von
Dipl. Ing. (FH) Benjamin Witschas
geboren am 08.03.1982 in München

Gutachter:

1. **Prof. Dr. Andreas Tünnermann**
   Institut für Angewandte Physik
   Friedrich-Schiller-Universität Jena

2. **apl. Prof. Dr.-Ing. Dr. rer. nat. habil. Ulrich Schumann**
   Institut für Physik der Atmosphäre
   Deutsches Zentrum für Luft- und Raumfahrt, Oberpfaffenhofen
   und
   Meteorologisches Institut
   Ludwig-Maximilians-Universität München

3. **Dr. habil. Albert Ansmann**
   Leibniz-Institut für Troposphärenforschung e.V.
   Leipzig

Tag der Verteidigung: Dienstag, der 25.10.2011

Abstract

Atmospheric lidar techniques for the measurement of wind, temperature, and optical properties of aerosols as well as non-intrusive measurement techniques for temperature, density and bulk velocity in gas flow rely on the exact knowledge of the spectral line shape of the scattered laser light on molecules. The best model currently available to describe these line shapes is the Tenti S6 model which, however, has not yet been validated in air. In this thesis, high-precision spontaneous Rayleigh-Brillouin (SRB) scattering experiments on N_2 as well as on dry and humid air are presented and used to prove the accuracy of the Tenti S6 line shape model and to investigate the influence of water vapor on the SRB line shape. The measurements were performed in controlled laboratory experiments as well as in the atmosphere. In contrast to earlier SRB scattering experiments in the visible spectral region, the measurements were carried out with ultraviolet light, which is used by the lidars on the satellite missions ADM-Aeolus and EarthCARE. The laboratory SRBS measurements were performed at a wavelength of 366.5 nm and a scattering angle of 90°. The comparison of the measured SRB line shapes and the Tenti S6 model under atmospheric pressures shows a deviation of less than $\pm$ 2 % with respect to the peak intensity. It is demonstrated that the SRB line shapes of N_2 and air under equal pressure and temperature conditions differ significantly, which is due mainly to the difference in their molecular masses, but also to the difference in their transport properties. Furthermore it is shown that the Gaussian approximation for SRB line shapes of molecular scattered light in air is inadequate for pressures down to 300 hPa. In addition, SRB line shapes are used in combination with the Tenti S6 model to determine the bulk viscosity of N_2 and air for frequencies in the Gigahertz-range. The obtained values are larger than the values published for acoustic frequencies by a factor of 1.6 and 1.3. Moreover, it is shown that high amounts of water vapor in the atmosphere, up to a volume fraction of 3.6 vol. %, have no influence on the SRB line shape of the scattered light. During the course of the field campaign BRAINS (Brillouin scattering - atmospheric investigation on Schneefernerhaus), horizontal lidar measurements (λ = 354.89 nm, θ = 180°) for the investigation of SRB scattering in the atmosphere were performed from the environmental research station Schneefernerhaus (UFS, 2650 m), located at the mountain Zugspitze. The atmospheric temperatures and pressures during BRAINS were between 250 K - 272 K and 702 hPa - 736 hPa, respectively. The horizontal lidar measurements were used to demonstrate the effect of Brillouin scattering within the atmosphere for the first time, using a specifically developed analysis technique. The atmospheric measurements confirmed that the Tenti S6 model can be used to describe SRB line shapes in air, also in case of backscattering geometry (θ = 180°) and under real air conditions. Additionally, it was verified that trace and noble gases in air do not have a significant influence on the SRB line shape and that the transport coefficients of air derived from temperatures of 297 - 300 K are also suitable for temperatures down to 263 K.

Contents

Chapter 1

Introduction

The invention of the laser by Maiman (1960) laid the groundwork for the use of spontaneous Rayleigh-Brillouin scattering (SRBS) in the study of fluid and gas dynamics (Boley et al., 1972; Mountain, 1966; Sugawara and Yip, 1967; Tenti et al., 1974), as well as in the development of non-intrusive diagnostic methods in atmospheric applications such as light detection and ranging (lidar) measurements for temperature (Liu et al., 2009b; Shimizu et al., 1986), aerosol content (Eloranta, 2005; Esselborn et al., 2008; Fiocco and DeWolf, 1968; Liu et al., 2009a) and wind velocity (Dabas et al., 2008; Gentry et al., 2000; McGill et al., 1997b; Reitebuch et al., 2009). The underlying concept of these measurement techniques is based on the idea to resolve the spontaneous Rayleigh-Brillouin (SRB) spectral line shape with high-resolution interferometers and relate it to theoretical SRB line shape models. Hence, the accuracy of these measurements depends directly on the precision of theoretical line shape models.

SRBS in molecular gases originates from thermal density fluctuations which spontaneously arise due to the random thermal motion of molecules. These density fluctuations lead to a fluctuating dielectric constant, which in turn leads to fluctuations in the index of refraction, and finally to the scattering of light (Fabelinskii, 1968). Density fluctuations in molecular gases have two different origins. They are either caused by temperature fluctuations at constant pressure due to the thermal motion of the molecules, or by pressure fluctuations at constant temperature due to collisions between molecules. Light scattering on temperature fluctuations is called Rayleigh scattering in honor of Lord Rayleigh who made fundamental contributions to the invention of molecular light scattering (Rayleigh, 1871, 1881, 1899, 1918). Light scattering on pressure fluctuations is called Brillouin scattering according to Leon Brillouin (1922) who theoretically described this kind of scattering mechanism for the first time. SRBS therefore describes light scattering on temperature and pressure fluctuations which spontaneously arise in gases.

For atmospheric applications that utilize SRB scattering, the spectrum of the scattered light is of special interest. Basically, it is an image of the velocity distribution of the molecules within the scattering medium, and therefore contains information on gas density, pressure, temperature and bulk velocity, as well as on gas transport properties like heat capacity, thermal conductivity, shear and bulk viscosity, as all of these quantities influence the motion of molecules. Thus, all these quantities can be determined by comparing measured SRB spectra with an appropriate line shape model. For instance in a very dilute gas where the motion of a single molecule is not affected by its neighbors, the spectrum of the scattered light can be described by a Gaussian function due to the Maxwell-velocity distribution of the molecules. However, at gas pressures relevant for atmospheric applications, collisions between molecules have to be considered as they lead to a change in the velocity distribution. Thus, the SRB line shape can no longer be represented by a Gaussian function for atmospheric applications (Fiocco and DeWolf, 1968). For example, in the retrieval of atmospheric optical properties from observations of airborne high-spectral resolution lidar (HSRL), errors between 3 % to 20 % can occur for the aerosol backscatter coefficient for unaccounted Brillouin scattering in case of medium to high aerosol content (Liu et al., 2009a). The errors are even a factor of 2 larger for a spaceborne HSRL, as it is planned on the ESA space mission EarthCARE (Earth Clouds, Aerosols, and Radiation Explorer), which aims to improve the representation and understanding of the Earth's radiative balance in climate and numerical weather forecast models by acquiring vertical profiles of clouds and aerosols, as well as the radiances at the top of the atmosphere (European Space Agency, 2004).

A further example for the importance of considering the Brillouin effect for atmospheric applications is the wind measurement by using a direct-detection Doppler wind lidar (DWL) based on molecular scattering. For such a DWL, a systematic, wind speed dependent error in the retrieved wind speed occurs if the scattered frequency spectrum is assumed to be Gaussian and Brillouin scattering is neglected. The wind speed is overestimated by 10 % at sea level and still by 3 % for 10 km altitude (Dabas et al., 2008; Flamant et al., 2005). In the framework of the Atmospheric Dynamics Mission ADM-Aeolus, a DWL is going to be used to provide global observations of wind profiles from space to improve the quality of weather forecasts, and to advance the understanding of atmospheric dynamics and climate processes (European Space Agency, 2008; Stoffelen et al., 2005). For ADM, the systematic error in wind speed determination should be below 0.7 % of the measured wind speed. This challenging goal can only be achieved by taking Brillouin scattering into account for the wind retrievals up to altitudes of 30 km (Dabas et al., 2008; Tan et al., 2008).

For a correct SRB line shape description it is necessary to model the density fluctuations within the scattering medium, which is commonly done using the general kinetic Boltzmann equation (Gombosi, 1994). However, because of its mathematical complexity, it is not possible to evaluate the Boltzmann equation and approximate models must be derived. Based on an approximate solution of the linearized Boltzmann equation, Boley et al. (1972) and Tenti et al. (1974) described a model (from now on called Tenti S6 model) for the spectral line shape of SRB scattered light, that has since then widely been applied for the retrieval of optical properties with HSRL (Esselborn et al., 2008; Hair et al., 2001, 2008; Liu et al., 2009a) and wind speeds with DWL (Cézard et al., 2009; Dabas et al., 2008; Rye, 1998). Although the Tenti S6 model was developed for gases of a single-component molecular species, it is considered to be the most appropriate model for atmospheric conditions (Miles et al., 2001; Young and Kattawar, 1983). However, as air is a mixture of several gases with different properties the applicability of the Tenti S6 model in air is questionable and has to be verified by measurements. A few laboratory experiments aiming at deriving the SRB line shape have been performed in several atomic and molecular gases (Ghaem-Maghami and May, 1980; Greytak and Benedek, 1966; Hara et al., 1971; Lao et al., 1976; Letamendia et al., 1982; Lock et al., 1992; Pan et al., 2002, 2004b; Sandoval and Armstrong, 1976). However, up to now, no SRBS measurements have been performed in air; neither in a laboratory experiment nor in the atmosphere. Currently available SRB line shape models have been verified by SRBS measurements: Tenti et al. (1974) compared their S6 model to measurements on the hydrogen molecule and its deuterium containing isotopologues by Hara et al. (1971), whereas Sandoval and Armstrong (1976) compared their N_2 measurements with a line shape model by Sugawara and Yip (1967). Lao et al. (1976) used N_2 measurements at a pressure of 11000 hPa and CO_2 measurements down to 200 hPa for their comparison to the Tenti S6 model. However, none of the performed measurements on N_2 at atmospheric conditions were compared to the Tenti S6 model.

The need for an exact description of the SRB line shape in atmospheric applications and the associated demand of validating the commonly used Tenti S6 model for its applicability in air defines the main objective of this thesis. To validate the Tenti S6 line shape model in air, SRBS experiments are performed in two different ways aiming to cover different issues. On the one hand they are performed within a controlled laboratory experiment and on the other hand within the atmosphere.

High-precision laboratory SRBS experiments on N_2 as well as on dry and humid air are presented and used to proof the accuracy of the Tenti S6 model and to investigate the influence of water vapor to the SRB line shape. In contrast to earlier SRBS experiments in the visible spectral region, these measurements are performed in the ultraviolet, which is widely used for direct-detection DWL and HSRL, including the lidar on ADM-Aeolus and EarthCARE. In order to use the obtained laboratory results for the data retrieval of atmospheric applications, they have to be further validated by measurements in the real atmosphere under real conditions. This was done in the framework of the measurement campaign BRAINS (Brillouin scattering - atmospheric investigation on Schneefernerhaus), where horizontal lidar measurements were performed from the environmental research station Schneefernerhaus. Horizontal lidar measurements in the atmosphere thereby offer the unique possibility to investigate the SRB line shape at a scattering angle of 180°, whereas the laboratory measurements were performed at a scattering angle of 90°. However, SRBS measurements under atmospheric conditions are challenging and have not been successfully performed yet.

In summary, the scientific questions addressed in this thesis are:

- Is the description of SRB line shapes in air using the Tenti S6 model accurate?
- Does water vapor influence the SRB line shape in air?
- Is it possible to demonstrate the effect of Brillouin scattering in the atmosphere?
- Do any effects in the atmosphere restrict the application of the Tenti S6 model?

Chapter 2 deals with the fundamentals of light scattering on molecules. The various molecular light scattering mechanisms (section 2.1) and their characteristic imprint on the spectrum of the scattered light (section 2.2) are presented. The derivation of the Tenti S6 model as well as its possible limitations with respect to atmospheric applications are reviewed (section 2.3), followed by a summary of Chapter 2 in section 2.4. In chapter 3, the performed laboratory experiments on SRBS in nitrogen, dry and humid air are discussed. First, an overview of previous performed SRBS measurements is given (section 3.1), followed by the description of the experimental details of the setup (section 3.2). Thereafter, the results of this study are shown (section 3.3) and summarized (section 3.4). In chapter 4, the performed study on SRBS in the real atmosphere is presented. The experimental details including setup, measurement geometry, measurement procedure and data analysis are given in section 4.2. After that, the results of these experiments are discussed (section 4.3) and summarized (section 4.4). A final conclusion of the present thesis and an outlook are given in chapter 5.

Chapter 2

Light scattering on molecules

Especially since the invention of the laser by Maiman (1960), light scattering has become a widespread non-intrusive diagnostic tool in atmospheric applications such as lidar measurements (Browell et al., 1998; Dabas et al., 2008; Eloranta, 2005; Fiocco and DeWolf, 1968; Gentry et al., 2000; Liu et al., 2009a,b; McGill et al., 1997b; Measures, 1984; Reitebuch et al., 2009; Shimizu et al., 1986; Vogelmann and Trickl, 2008; Weitkamp, 2005), as well as in aerospace applications such as combustion (Elliott et al., 2001) and flow measurements (Seasholtz et al., 1997). Thereby, the characteristic of the scattered light is used to derive gas properties like temperature, density, and bulk velocity. To achieve precise results using the various kinds of this measurement technique, an accurate understanding of the underlying scattering process is needed.

In this chapter, the basic scattering mechanisms arising in molecular gases are discussed concerning their origin (section 2.1) and their influence on the spectrum of the scattered light (section 2.2). In section 2.3, the spectral line shape of the Cabannes line as the result of Rayleigh-Brillouin scattering is considered for different gas conditions. This is followed by a detailed discussion of the widespread Tenti S6 model which is commonly used for modeling the Cabannes line of light scattered on air at atmospheric conditions (Dabas et al., 2008; Elliott et al., 2001; Liu et al., 2009a,b; Seasholtz et al., 1997).

2.1 Physical description of different molecular light scattering mechanisms

When light travels through matter, various scattering processes occur. Independent of the aggregate state of the matter, the origin of scattering processes is a result of the

fluctuations in the optical properties of the medium. For atmospheric applications the propagation medium is air, which is mainly composed of the diatomic gases nitrogen (N_2) and oxygen (O_2). In such molecular gases, such fluctuations are caused by statistical fluctuations in the arrangement of the molecules which can lead to different kinds of scattering processes. Thereby, each physical contribution to the generation of scattered light makes its characteristic imprint on the intensity, polarization and spectral composition of the scattered light. For the characterization of the different scattering mechanisms, a chief distinction is drawn between elastic and inelastic scattering, where elastic scattering denotes scattering with and inelastic scattering without a change in the scattered light's frequency. Furthermore, it can be distinguished between light scattering from single molecules (e.g. Raman scattering, section 2.1.2), or light scattering because of collective effects (e.g. Rayleigh-Brillouin scattering, section 2.1.3). The most prominent scattering mechanisms in molecular gases are Rayleigh scattering, Raman scattering and Brillouin scattering, all of them named after their discoverer. However, the terminology used to describe the different scattering mechanisms is not consistent in literature. In the early 1980s, Young (1980, 1981) gave a review about the history of discoveries concerning molecular light scattering and suggested the terminology sketched in Fig. 2.1.

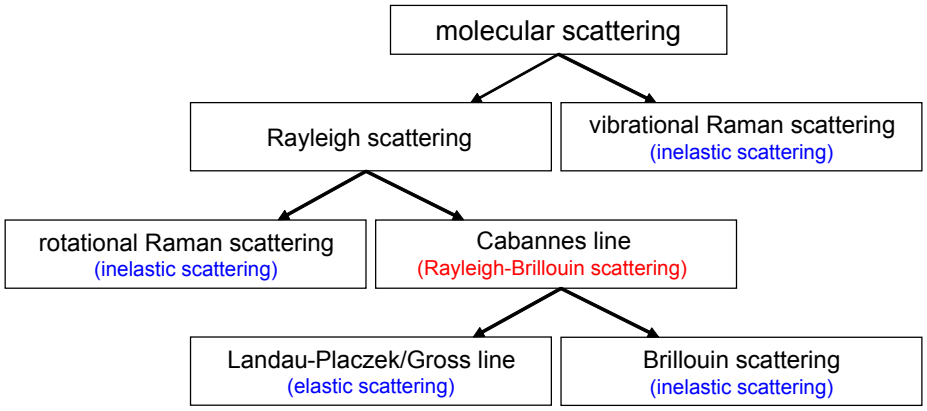

Figure 2.1: Overview of different scattering mechanisms in molecular gases according to the nomenclature suggested by Young (1980, 1981).

It is noticeable that, according to Young, Rayleigh scattering not only covers elastic light scattering, as it is often mentioned in literature, but it also contains the inelastic rotational Raman scattering and the Cabannes line, which can be divided into the Landau-Placzek or Gross line, which arises from light scattering on temperature fluctuations at constant pressure, and Brillouin scattering, which arises from light scattering

on pressure fluctuations at constant temperature (see section 2.1.3). It is worth mentioning that the Cabannes line is commonly regarded as the result of Rayleigh-Brillouin scattering. Although this naming is not covered by the nomenclature of Young, it will be used throughout this thesis as it is common in the "light–scattering community" (e. g. (Ghaem-Maghami and May, 1980; Hara et al., 1971; Lao et al., 1976; Lock et al., 1992; Pan et al., 2005; Sandoval and Armstrong, 1976; She et al., 1983; Tenti et al., 1974)).

2.1.1 Rayleigh scattering

The invention of the concept of molecular light scattering traces back to Lord Rayleigh who used the word scattering (instead of reflection) for the first time (Rayleigh, 1871). By considering light scattering on small particles accelerated by an incident light wave, Rayleigh derived the λ^{-4} dependence of the intensity of scattered light and used this result to explain the blue color of the sky. 10 years later, Rayleigh (1881) re-derived this result using the laws of Maxwell, still considering spherical particles as the origin for the scattering mechanism. In 1899, for the first time, he suggested that not particles but the molecules in air are responsible for light scattering in the atmosphere (Rayleigh, 1899). It took almost 20 more years until Rayleigh developed the theory of a cloud of small particles of any shape and random orientation (Rayleigh, 1918).

When light scatters on molecules, the scatterers are much smaller than the wavelength of the incident light[1], and therefore, the scattering process can be described by the model of induced dipole radiation. That is, the incident electromagnetic radiation drives a dipole oscillation within the molecule, and as a result, the molecule re-emits radiation in all directions and with the same frequency as that of the incident light.

The electric field E_s and the intensity I_s which is emitted by a dipole is given by (Miles et al., 2001)

$$|\boldsymbol{E}_\mathbf{s}| = \frac{\omega^2\, p\, \sin(\Phi)}{4\,\pi\, r\, \epsilon_0\, c^2}, \quad I_\mathrm{s} = \frac{\epsilon_0\, c\, |\boldsymbol{E}_\mathbf{s}|^2}{2} \tag{2.1}$$

where ω is the oscillation angular frequency, p the magnitude of the oscillation dipole moment induced by the incident field, r the distance from the dipole, c the velocity of light in vacuum, ϵ_0 the vacuum permittivity, and Φ the angle of observation with respect to the dipole vector. In the case of the simplified assumption of a radial symmetric molecule, the dipole moment $\boldsymbol{p}$ is induced in the same direction as the incident field

[1] In case of visible light scattered on nitrogen molecules, the wavelength ($\sim$ 500 nm) is about 3 orders of magnitude larger than the diameter of the molecules ($\sim$ 300 pm).

polarization, and is linearly proportional to the incident electric field $\boldsymbol{E}_\mathbf{i}$. The scalar proportionality is termed the polarizability α

$$\boldsymbol{p} = \alpha\, \boldsymbol{E}_\mathbf{i} \tag{2.2}$$

By substituting $p^2 = \alpha^2\, |E_\mathrm{i}|^2$, $I_\mathrm{s} = (\epsilon_0\, c/2)\, |E_\mathrm{s}|^2$, and $I_\mathrm{i} = (\epsilon_0\, c/2)\, |E_\mathrm{i}|^2$, the scattering intensity of one molecule is

$$I_\mathrm{s} = \frac{\pi^2\, \alpha^2}{\epsilon_0^2\, \lambda^4\, r^2}\, I_\mathrm{i}\, \sin^2 \Phi \tag{2.3}$$

A more general description of the light scattering process leading to the same result goes back to Einstein (1910). In his approach, the origin of light scattering is described by density fluctuations in the propagation medium. Density fluctuations in the medium lead to a fluctuating index of refraction, which in turn leads to the scattering of light (Fabelinskii, 1968). In particular, it can be shown that the component of scattered light polarized in the same direction as the incident light yields the space-time Fourier transformation of the density-density correlation function (Van Hove, 1954). This being true, it is possible to calculate the spectrum of scattered light by modeling the density fluctuations in the propagation medium and then calculate its Fourier transformation. This approach is also applied when deriving the Tenti-S6 model, as it is partly discussed in section 2.3.

For further discussion of the spectral contribution of the various scattering processes, it is useful to define the differential scattering cross section $\partial\sigma/\partial\Omega$, which can be interpreted as the probability that light is scattered. The differential scattering cross section is defined according to (Miles et al., 2001)

$$I_\mathrm{s} = \frac{\partial\sigma}{\partial\Omega}\, \frac{1}{r^2}\, I_\mathrm{i} \tag{2.4}$$

Using Eq. 2.4 in combination with Eq. 2.3 it is possible to calculate the differential cross section for spherically symmetric molecules, however, real molecules are not spherically symmetric, they are slightly elongated. This fact leads to a more complicated description of the scattering process. More precisely, the elongated shape of real molecules leads to rotational and vibrational Raman scattering and a slight depolarization in the scattered light, as the induced dipole moment is not necessarily in the direction of the applied field. To describe the scattering process on real molecules, it is necessary to express the polarizability mentioned in Eq. 2.2 as a tensor $\boldsymbol{\alpha}$, which is described by the mean polarizability a and the anisotropy γ (Miles et al., 2001)[2].

[2]Since the molecules in a sample volume are randomly orientated, the scattering has to be averaged over all molecular angles. This averaging can be expressed in terms of two parameters which are invariant with respect to rotation: the mean polarizability a and the anisotropy γ.

The differential scattering cross section according to Rayleigh is

$$\left(\frac{\partial\sigma}{\partial\Omega}\right)_{\text{Rayleigh}} = \frac{\pi^2}{\epsilon_0{}^2\,\lambda^4}\left(a^2 + \frac{7}{45}\gamma^2\right)\sin^2\Phi \tag{2.5}$$

As already implied with Fig. 2.1, the Rayleigh differential cross section is composed of the rotational Raman differential cross section which is covered by the $(7/45)\gamma^2$-term, and the Cabannes differential scattering cross section which is covered by the a^2-term in Eq. 2.5. Considering $a^2 = 3.92 \cdot 10^{-80}$ m^6 and $\gamma^2 = 6.44 \cdot 10^{-81}$ m^6 for molecular nitrogen (N_2) (Wandinger, 2005), one can immediately see that the contribution of the complete rotational Raman scattering to the Rayleigh cross section is only about 2.5 %.

2.1.2 Raman scattering

The phenomenon of Raman scattering was discovered and first described by the Indian physicists Raman and Krishnan (1928). Raman scattering in molecular gases is an inelastic scattering process which originates from light interaction with resonant modes of a molecule, and thus, a quantum mechanical description of the scattering process is needed. If an incident photon is scattered by a molecule which thereby simultaneously undergoes a transition between vibrational or rotational states, its frequency is changed. If the molecule absorbs energy during the scattering process, i.e., a higher energy level is excited, the frequency of the scattered photon is decreased (wavelength red-shift). This process is called Stokes Raman scattering, in the style of the Stokes shift to longer wavelengths for the fluorescence process by molecules. If the molecule transfers energy to the scattered photon by decreasing its internal energy, the frequency of the scattered photon is increased (wavelength blue-shift), and the process is called anti-Stokes Raman scattering.

To be able to compare the different spectral influences of the various scattering mechanisms (section 2.2), some details of the Raman scattering process on diatomic molecules are discussed as follows. A more detailed overview is given by Long (2002) and Wandinger (2005).

If f_i and f_s are the frequencies of the incident and the scattered light, respectively, the frequency shift Δf which occurs during the Raman scattering process is given by

$$\Delta f = f_\text{i} - f_\text{s} = \frac{\Delta E}{h} \tag{2.6}$$

where h is the Planck's constant, and ΔE the energy difference between the involved molecular energy levels. The possible energy levels can be calculated by modeling the diatomic molecule as a freely rotating harmonic oscillator. By doing so, the different vibrational and rotational energy levels result in (Wandinger, 2005):

$$E_{\mathrm{vib},v} = h\, f_{\mathrm{vib}}\,(v + 1/2)\,, \quad v = 0, 1, 2, ... \tag{2.7}$$

and

$$E_{\mathrm{rot},J,v} = h\,\left[B_v\, J\,(J+1) - D_v\, J^2\,(J+1)^2\right], \quad J = 0, 1, 2, ... \tag{2.8}$$

where f_{vib} is the specific vibrational oscillator frequency of the molecule, and v and J the vibrational and rotational quantum numbers, respectively. B_v is the molecular specific rotational constant and D_v the stretching constant (Wandinger, 2005). Considering the selection rules for vibrational and rotational transitions ($\Delta v = 0, \pm 1$ and $\Delta J = 0, \pm 2$), the occurring frequency shifts Δf can be calculated. Here, $\Delta J = J' - J''$, with J' as the quantum number of the higher and J'' the one of the lower energy level, and Δv is the difference of the vibrational quantum numbers of the final and the initial vibrational states.

Transitions with $\Delta v = +1,\ \Delta J = 0$ lead to the so-called Q-branch of the Stokes vibration-rotation band (Fig. 2.4, green diamond), those with $\Delta v = -1,\ \Delta J = 0$ to the Q-branch of the anti-Stokes vibration-rotation band (Fig. 2.4, dark green diamond). The transitions with $\Delta J = \pm 2$ lead to the rotational Raman lines for $\Delta v = 0$, and to the vibration-rotation Raman lines for $\Delta v = \pm 1$ (Fig. 2.4, black dots, gray lines). Transitions with $\Delta J = \Delta v = 0$ lead to the Q-branch of the rotational Raman band (Fig. 2.4, red diamond), which contributes to the Cabannes line (section 2.1.3) with an incoherent and unpolarized part of the scattered radiation[3].

To derive the intensity of each observed line, the differential scattering cross section must be calculated. The Raman differential cross section of the rotational Raman Q-branch (unshifted), and the rotational Raman lines (shifted) are determined by the anisotropy of the polarizability γ and can be expressed by (Miles et al., 2001)

$$\left(\frac{\partial\sigma}{\partial\Omega}\right)_{\mathrm{Q-branch}} = \frac{\pi^2}{{\epsilon_0}^2\,\lambda^4}\,\frac{7}{180}\,\gamma^2\sin^2\Phi \quad \text{and} \quad \left(\frac{\partial\sigma}{\partial\Omega}\right)_{\mathrm{Rot}} = \frac{\pi^2}{{\epsilon_0}^2\,\lambda^4}\,\frac{7}{60}\,\gamma^2\sin^2\Phi \tag{2.9}$$

[3]The Q-branch of the rotational Raman line is due to transitions between degenerate states with different magnetic quantum numbers but the same rotational (J) and vibrational (v) numbers. Therefore, the frequency of the scattered light is not changed within this scattering process.

Using Eq. 2.9 one can immediately see, that the differential cross section of the frequency unshifted Q-branch is exactly one third of the one of the frequency shifted rotational Raman lines, and one fourth of the total rotational Raman differential cross section.

For a more detailed derivation of the spectral distribution, it is necessary to consider the population distribution of the internal energy levels, the degeneracy $2J + 1$ of the initial rotational energy level J, the nuclear-spin degeneracy $2I + 1$ and the nuclear-spin statistical weight factor (Wandinger, 2005). If this is done, the Raman differential scattering cross section, and therefore, the spectral distribution for molecular scattered light can be calculated. An example of the Raman spectrum for N_2, at an ambient temperature of 300 K and a scattering angle of $\theta = 180°$ is illustrated in Fig. 2.4 (Top and middle)[4]. The single components of the spectrum of molecular scattered light are discussed in more detail in section 2.2.

2.1.3 The Cabannes line (Rayleigh–Brillouin scattering)

According to Einstein (1910), light scattering can be described to originate from density fluctuations in inhomogeneous media. The spectral component of the scattered light which is caused by these density fluctuations is called Cabannes line, according to Cabannes and Rocard (1929), who first derived the intensities of the central and rotational Raman shifted lines, and showed that the sum of both is exactly Rayleigh's result (Eq. 2.5). The process which yields the Cabannes line is commonly described as Rayleigh-Brillouin scattering, although this naming is not correct according to the nomenclature of Young (1981).

Density fluctuations in media arise from the thermal motion of molecules and lead to fluctuations in the optical dielectric constant, which in turn leads to fluctuations in the index of refraction, and finally, to the scattering of light. The density fluctuations in a molecular gas can be divided into pressure fluctuations and temperature fluctuations (Fabelinskii, 1968). In addition, the pressure fluctuations can be viewed as random local compressions and rarefactions which, as a consequence of the elastic properties of the medium, do not remain fixed in position but travel throughout the volume of the medium. Thus, the numerous random compressions and rarefactions can be considered as elastic sound waves (acoustic phonons) of various different frequencies, which propagate with the corresponding velocity of sound in all possible directions inside the

[4]The spectrum is calculated by using Eq. 2.5 to Eq. 2.9 with $a^2 = 3.92 \cdot 10^{-80}$ m^6 and $\gamma^2 = 6.44 \cdot 10^{-81}$ m^6 and the corresponding equations for the differential cross section of the vibration-rotation Raman lines according to Wandinger (2005).

volume under study (Damzen, 2003). When laser light enters the medium, every sound wave scatters the incident light wave at angles for which constructive interference occurs (Bragg-condition) (Figgins, 1971). Furthermore, the frequency of the scattered light is shifted by the Doppler effect due to the motion of the scattering sound wave. This type of inelastic scattering mechanism was independently described by Brillouin (1922) and Mandelstam (1926) and is therefore commonly called Brillouin scattering in literature. The term Brillouin scattering is also used in connection with light scattering in solid states, where lattice fluctuations (e. g. acoustic phonons) are the origin for the scattering process (Kittel and McEuen, 1986).

For the further analysis of the Brillouin scattering process, the Bragg scattering analogy is considered as it is pictured in Fig. 2.2.

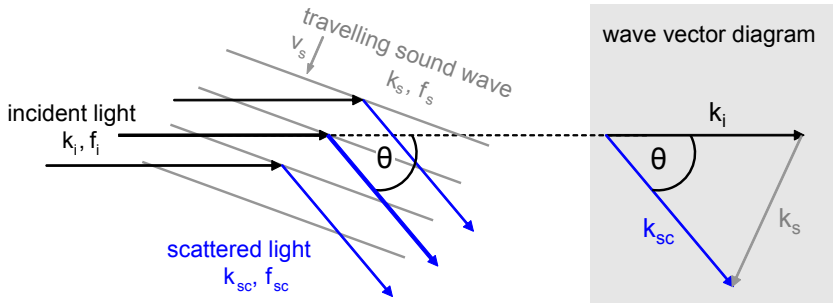

Figure 2.2: left: Schematic diagram of the Brillouin scattering process. The black arrows indicate the incident light, the blue arrows the scattered light, and the gray lines the traveling sound wave caused by pressure fluctuations which are responsible for the scattering process. right: Corresponding wave vector diagram.

The incident and the scattered light is defined by their wave vectors $\boldsymbol{k_i}$, $\boldsymbol{k_{sc}}$ and frequencies f_i, f_sc, respectively, and are pictured as black and blue arrows. The scattering angle is denoted by θ. The traveling sound wave which is responsible for the scattering of $\boldsymbol{k_i}$ is defined by wave vector $\boldsymbol{k_s}$, frequency f_s and phase velocity v_s, and is indicated with gray lines. Because of momentum conservation within the scattering process ($\boldsymbol{k_s} = \boldsymbol{k_i} - \boldsymbol{k_{sc}}$), the wave vector of acoustic phonons can be calculated using the law of cosine (Fig 2.2, wave vector diagram)

$$|\boldsymbol{k}_\mathrm{s}|^2 = |\boldsymbol{k_i}|^2 + |\boldsymbol{k_{sc}}|^2 - 2\,|\boldsymbol{k_i}|\,|\boldsymbol{k_{sc}}|\,\cos(\theta) \tag{2.10}$$

As the change in frequency of the scattered light is small ($\approx 10^{-5}$) (Figgins, 1971), one can approximate $|\boldsymbol{k_{sc}}| \approx |\boldsymbol{k_i}|$. By further using $1-\cos(\theta) = 2\,\sin^2(\theta/2)$, Eq. 2.10 reduces to

$$|\boldsymbol{k}_\mathrm{s}| = \pm\,2\,|\boldsymbol{k_i}|\,\sin(\theta/2) \tag{2.11}$$

This enables the possibility to calculate the frequency shift f_s between incident and scattered light, and therefore, the spectral location of the Brillouin peaks. Per definition, $|\boldsymbol{k}_\mathbf{i}| = 2\pi\, n/\lambda_\mathrm{i}$, with λ_i the wavelength of the incident light and n the index of refraction of the medium, and $\lambda_\mathrm{s} = c_\mathrm{s}/f_\mathrm{s}$, with c_s and f_s as sound velocity and sound frequency, respectively. Thus, f_s is

$$f_\mathrm{s} = 2\,\frac{c_\mathrm{s}\, n}{\lambda_\mathrm{i}}\,\sin(\theta/2) \tag{2.12}$$

From Eq. 2.12, it can be seen that f_s reduces to zero in the forward direction ($\theta = 0°$) and is maximum in the backward direction ($\theta = 180°$). Therefore, the frequency shift due to Brillouin scattering is largest for lidar applications in backscattering geometry. With $c_\mathrm{s} = (\gamma\, k_B\, T/M)^{1/2}$, M the mass of a molecule, $\gamma = 1.4$ the heat capacity ratio when no vibrational degrees of freedom are excited, $k_B = 1.38 \cdot 10^{-23}$ J/K the Boltzmann constant, the frequency shift f_s is about 1.8 GHz for lidars operating at a wavelength of 355 nm.

In addition to Brillouin scattering which arises from pressure fluctuations in the medium, there is a scattering mechanism associated with temperature fluctuations. These temperature fluctuations can again be viewed as waves which lead to a scattering of light if the Bragg condition is fulfilled. However, the temperature fluctuations are static in space and therefore do not produce a frequency Doppler shift for the scattered light. This part of the Cabannes line was first resolved by Gross (1930) and theoretically described by Landau and Placzek (1934). It is therefore commonly called Gross or Landau-Placzek line (Fig. 2.1) and leads to the elastic part of the spectrum of molecular scattered light.

The Cabannes line differential scattering cross section is given by (Miles et al., 2001)

$$\left(\frac{\partial\sigma}{\partial\Omega}\right)_\mathrm{Cabannes} = \frac{\pi^2}{{\epsilon_0}^2\,\lambda^4}\, a^2 \sin^2\Phi \tag{2.13}$$

As obvious from the discussion above, there are two different kinds of density fluctuations (pressure and temperature) which lead to different parts in the spectrum of the scattered light (Brillouin doublet and Landau-Placzek line). Whereas the temperature fluctuations are caused by the thermal motions of the molecules, pressure fluctuations actually arise from collisions between different molecules. Thus, the effect of Brillouin scattering becomes more prominent when the number of collisions between molecules increases, or rather the mean free path between molecules decreases. A key parameter

for describing which of these two scattering mechanisms is dominant is the ratio y of the scattering wavelength $2\pi/k_\mathrm{s}$ to the mean free path of collisions (Boley et al., 1972; Tenti et al., 1974),

$$y = \frac{p}{k_\mathrm{s}\, v_0\, \eta} = \frac{n\, k_B\, T}{k_\mathrm{s}\, v_0\, \eta} \tag{2.14}$$

with n the number density, T the temperature, p the pressure, v_0 the most probable thermal velocity, $v_0 = (2\, k_B\, T/M)^{1/2}$, and η the viscosity. The definition of y is based on the dimensional relation between the mean free path between collisions and the shear viscosity η [5].

For the description of the spectral distribution of the Cabannes line, one uses the y parameter to define different scattering regimes in order to apply approximations in the calculation of the respective spectra.

For $y \gg 1$, the so-called hydrodynamic regime, the mean free path between collisions is much smaller than the scattering wavelength. In that case, the molecular gas can be treated as a continuum, and the density fluctuations within the gas can be calculated using the Navier-Stokes equations. The resulting spectrum of the scattered light can be well approximated by the sum of three Lorentzian functions displaced by f_s (Boon and Yip, 1991), where the central peak is due to scattering on temperature fluctuations (Landau-Placzek), and the shifted peaks due to scattering on pressure fluctuations (Brillouin scattering). This situation is indicated with the black area in Fig. 2.3.

In the Knudsen regime, $y \ll 1$, the mean free path between collisions is much larger than the scattering wavelength. Scattering is solely due to individual molecules, and the scattering due to pressure fluctuations is negligible. The line profile of the scattered light is described by a Gaussian function derived from a Maxwell velocity distribution of the molecules as it is given in Eq. 2.17. A spectrum which is representative for the Knudsen regime is indicated with the red area in Fig. 2.3.

In the kinetic regime $0.3 \lesssim y \lesssim 3$, which is the relevant regime for atmospheric scattering (e.g. $y \approx 0.1$ to 1.1 for standard tropospheric conditions according to the US Standard Atmosphere (1976), $\lambda = 355$ to 1064 nm, $\theta = 180°$), neither the individual particle approach nor the continuum approach applies, and one has to resort to solutions of the Boltzmann equation for describing the density fluctuations in the propagation medium (Gombosi, 1994). As there are no analytical solutions possible for this equation, approximate models have to be derived. The most popular model for that purpose is

[5] The y parameter is defined as the ratio of the scattering wavelength $2\pi/k_\mathrm{s}$ to the mean free path of collisions l_f. The mean free path l_f can be expressed by the ratio of the thermal velocity v_0 to the collision frequency ν_c which itself is given by $\nu_c = p/\eta$ (Hänel, 2004). Therefore $y = (p)/(2\,\pi\, k_s\, v_0\, \eta)$. The factor 2π is not considered in the y parameter definition given by Boley et al. (1972) and Tenti et al. (1974) and used within this thesis.

the Tenti S6 model which is discussed in section 2.3. In Fig. 2.3, the Tenti S6 model is already used to calculate the Cabannes lines within the kinetic regime (blue area). It is obvious that this is a intermediate region where neither the Gaussian nor the sum of three Lorentzian functions can be used for line shape description.

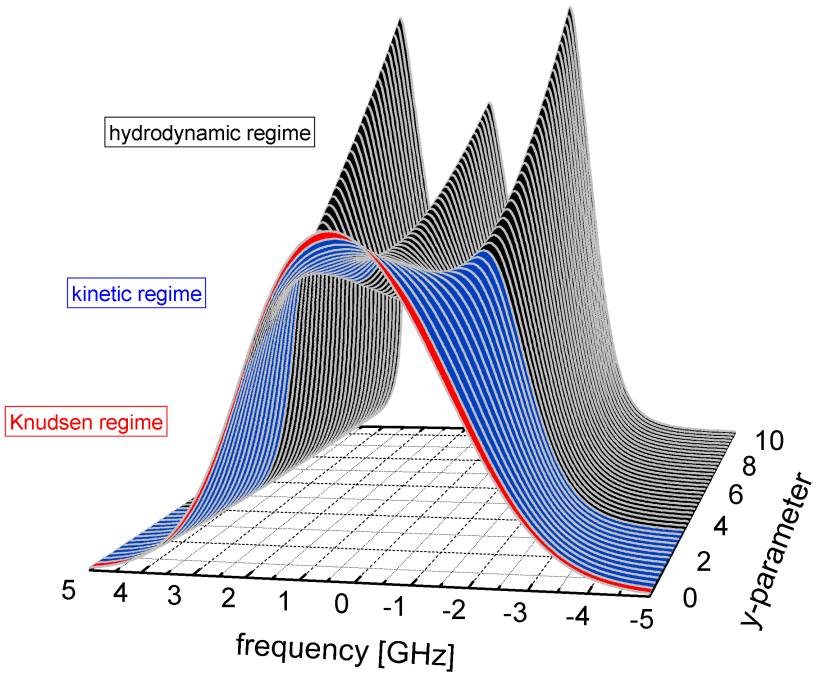

Figure 2.3: Evolution of the Cabannes line shape of spontaneous Rayleigh-Brillouin scattered light in nitrogen (wavelength $\lambda = 355$ nm, scattering angle $\theta = 180°$), calculated by using the Tenti S6 model (Tenti et al., 1974). Pressure values are varied to cover the region from $y = 0$ (Knudsen regime is indicated in red) to $y = 10.3$ (hydrodynamic regime is indicated in black). The intermediate regime, which is of special interest for atmospheric applications, is called kinetic regime (valid for $y \approx 0.3$–3 and indicated in blue). The gas transport parameters of nitrogen which are used for simulation can be found in Table A.1.

2.2 Comparison of the different spectral components of molecular scattered light

For better illustration of the spectral characteristics and the intensity ratios of the different scattering mechanisms, the spectrum of molecular scattered light is discussed for the example of ultraviolet light scattered in nitrogen ($\lambda = 355$ nm, $T = 300$ K, $\theta = 180°$). The corresponding spectrum is plotted in Fig. 2.4. The differential cross sections are calculated using Eq. 2.5 to Eq. 2.9 with $a^2 = 3.92 \cdot 10^{-80}$ m^6 and $\gamma^2 = 6.44 \cdot 10^{-81}$ m^6 and the corresponding equations for the differential cross section of the vibration-rotation Raman lines according to Wandinger (2005). The Cabannes line (Fig. 2.4, bottom) was calculated using the Tenti S6 model (Tenti et al., 1974).

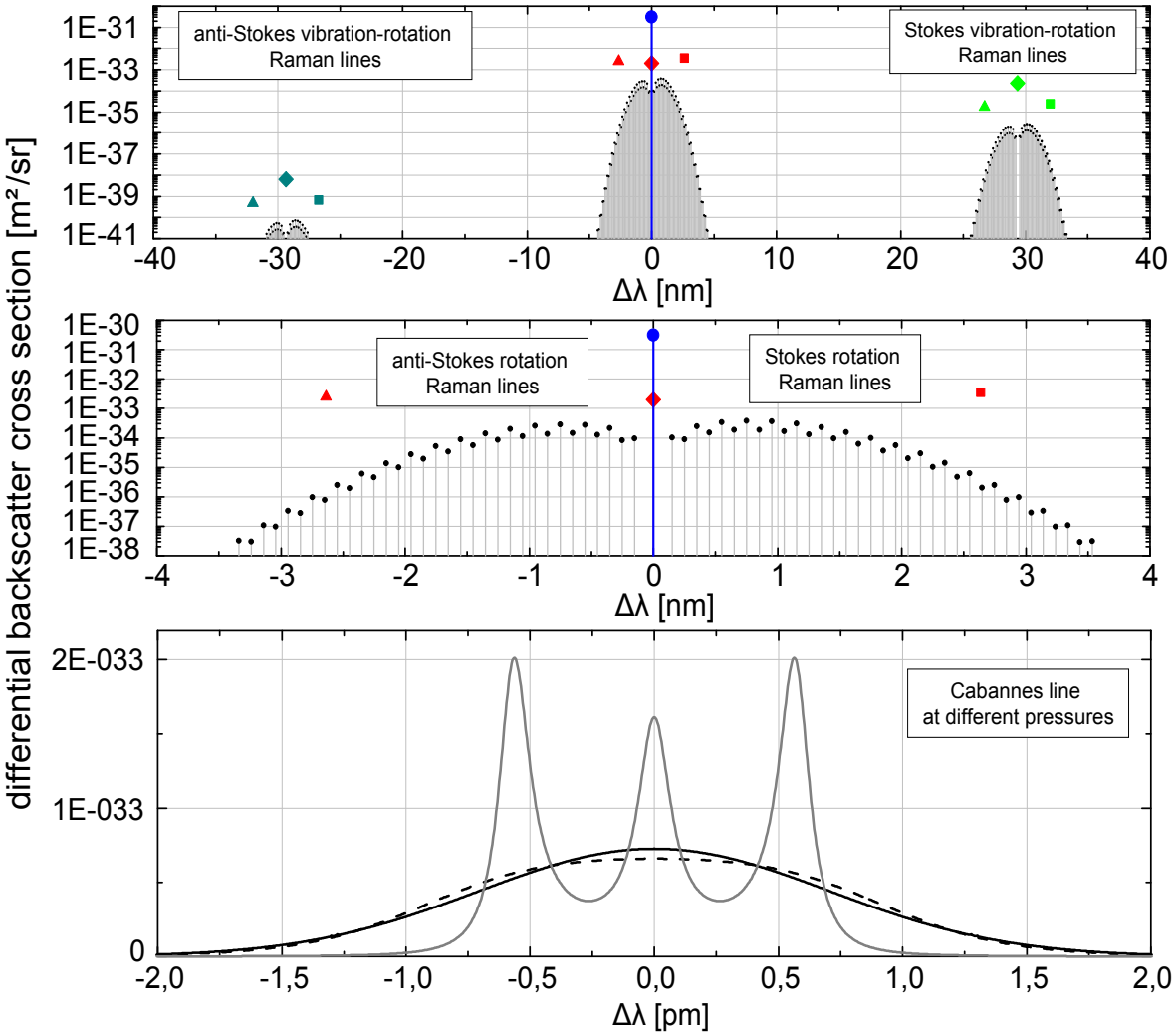

Figure 2.4: Simulated differential scattering cross section of light scattered in nitrogen (λ = 355 nm, $\theta = 180°$, T = 300 K). Top, middle: Resolved vibration-rotation and rotation Raman lines (log-scale). Shown are the sum of the differential cross sections: Cabannes line (blue dot), rotational Raman Q-branch (red diamond), rotational Stokes Raman lines (red square), rotational anti-Stokes Raman lines (red triangle), anti-Stokes vibration-rotation Raman Q-branch (dark green diamond), anti-Stokes vibration-rotation Raman lines (dark green triangle and square), Stokes vibration-rotation Raman Q-branch (green diamond), and Stokes vibration-rotation Raman lines (green triangle and square). The single rotation and vibration-rotation Raman lines are implied in light gray. Bottom: Resolved Cabannes line for different pressure values (linear scale). Cabannes lines representing the Knudsen regime ($p = 1 \cdot 10^{-6}$ hPa, black solid line), the kinetic regime ($p = 1000$ hPa, black dashed line) and the hydrodynamic regime ($p = 10000$ hPa, gray line) are shown.

The upper graph in Fig. 2.4 shows the resolved Stokes and anti-Stokes vibration-rotation Raman lines (black dots, gray lines) as well as their sum (green and dark green squares and triangles, respectively), and the sum of their Q-branches (green and dark green diamond). It is obvious that they are shifted by about 30 nm from the incident wavelength of 355 nm. This quite large wavelength shift is due to the large energy difference of the vibrational energy levels. Furthermore it can be seen that the scattering cross section of the anti-Stokes vibration-rotation Raman lines is about 6 orders of magnitude smaller than the one of the Stokes vibration-rotation Raman lines. This is characteristic for light scattering in gases with atmospheric relevant temperatures where almost all molecules are in the vibrational ground state. Therefore, vibrational Raman scattering mainly occurs when molecules absorb energy to excite a higher vibrational level, but not vice versa, as there are almost no vibrational levels excited. Whereas the anti-Stokes vibration rotation Raman lines do not play any role for atmospheric applications, the Stokes vibration rotation Raman lines can be used for temperature measurement by resolving their distribution and compare it to the Boltzmann population distribution (Behrendt et al., 2002; Wandinger, 2005). Furthermore, Rotational Raman scattering is also used to determine atmospheric water vapor content (Goldsmith et al., 1998), ozone concentrations (Donovan et al., 1995; Reichardt, 2000), and the extinction and backscatter coefficient (Ansmann et al., 1992; Tesche et al., 2009).

The middle graph shows the resolved Stokes and anti-Stokes rotation Raman lines (black dots, gray lines) as well as their sum (red square and triangle), and the sum of the rotation Raman Q-branch (red diamond). In contrast to the vibration-rotation Raman lines, the scattering cross section of the Stokes and anti-Stokes rotational Raman lines is almost equal. This is because the energy difference between rotational energy levels is quite low. This means that there are enough excited rotational energy levels, and the Raman scattering process can occur in both directions.

The wavelength shift of the first rotational Raman line is about 0.15 nm with respect to the fundamental wavelength of 355 nm, and therefore, narrow band filters can be used to resolve the Cabannes line without the influence of the rotational Raman lines (excluding the rotational Raman Q-branch). Moreover it is obvious that the scattering cross section of the unshifted rotational Q-branch is about two orders of magnitude smaller than the one of the Cabannes line (blue dot). In particular, considering the differential cross section of the rotation Raman Q-branch (Eq. 2.9, left), that of the Cabannes line (Eq. 2.13), and the polarizability a and anisotropy γ of nitrogen ($a^2 = 3.92 \cdot 10^{-80}$ m^6,

and $\gamma^2 = 6.44 \cdot 10^{-81}$ m^6 (Wandinger, 2005)), the contribution of the rotation Raman Q-branch to the Cabannes line is 0.64 % of the total intensity.

The lower graph shows the Cabannes lines for different gas pressure values simulated with the Tenti S6 model (Tenti et al., 1974). The black solid curve is representative for the Knudsen regime ($y \approx 0$). The spectrum is described by a Gaussian line shape according to the Maxwell velocity distribution. The gray curve shows the line shape representative for the hydrodynamic regime ($y = 5.6$). At such high pressures, the effect of Brillouin scattering is strongly pronounced, and the Landau-Placzek line can be easily distinguished from the Brillouin doublet. The wavelength shift of the Brillouin peaks is 0.55 nm which corresponds to a frequency shift of 1.8 GHz, and thus, to a sound velocity of 320 m/s [6]. The black dashed curve shows the line shape representative for the kinetic regime ($y = 0.56$). It is apparent that the line shape can neither be approximated by an ordinary Gaussian nor by the sum of three Lorentzians in that case. To describe the line shape in the kinetic regime, molecular gas dynamic equations have to be used. A common approach for describing the Cabannes line in the kinetic regime was introduced by Boley et al. (1972) and Tenti et al. (1974) and is described in section 2.3.

Summarized it can be concluded that the Cabannes line can be separated from the rotation and the vibration-rotation Raman lines, because of their large frequency shift with respect to the incident light. Such a filtering procedure is necessary for light scattering applications that use the characteristic line shape of the Cabannes lines for deriving gas properties like temperature, density and velocity. Furthermore, the scattering cross section of the Cabannes line is almost two orders of magnitude larger than the one of rotational Raman scattering and even three orders of magnitude in case of Stokes vibration-rotation Raman scattering. However, there is a contribution to the quasi frequency unshifted Cabannes line because of the Q-branch of rotational Raman scattering. This contribution is about 0.64 % of the total intensity of the Cabannes line.

2.3 The Cabannes line and the Tenti S6 model

Basically, the spectrum of scattered light is an image of the velocity distribution of the scatterers. Thus, if one had information about the location and the velocity vectors

[6] The connection between the light's wavelength and frequency, and the velocity of the sound wave responsible for scattering is given by the Doppler shift formula according to Eq. 2.12.

of all scatterers, the spectrum of the scattered light could be calculated. However, the large number of scatterers in a system is hard to handle[7], and a statistical description of the problem is necessary. Such a statistical description is given by the normalized phase space distribution function $f(\boldsymbol{v}, \boldsymbol{r}, t)$, which gives the probability of finding a particle with velocity $\boldsymbol{v}$ at the space location $\boldsymbol{r}$. To be able to describe dynamical processes in the scattering medium it is furthermore needed to describe the evolution of $f(\boldsymbol{v}, \boldsymbol{r}, t)$. This is done by the Boltzmann equation according to (Gombosi, 1994)

$$\left(\frac{\partial}{\partial t} + \boldsymbol{v}\frac{\partial}{\partial \boldsymbol{r}} + \boldsymbol{a}\frac{\partial}{\partial \boldsymbol{v}}\right) f(\boldsymbol{v}, \boldsymbol{r}, t) = \left(\frac{\delta f}{\delta t}\right)_{coll} \tag{2.15}$$

where $\boldsymbol{a}$ is the acceleration of an individual molecule caused by an external force and $(\delta f/\delta t)_{coll}$ is the collision term. Thus, the left hand side of the kinetic equation 2.15 accounts for rate of change because of particle movement and external force fields, whereas the right hand side accounts for the rate of change because of binary collisions between two particles.

In general, the collision term on the right hand side makes the Boltzmann equation a non-linear integro-differential equation which describes the dynamics of the distribution function $f(\boldsymbol{v}, \boldsymbol{r}, t)$ in the six dimensional phase space. It therefore depends on seven variables: time t, location $\boldsymbol{r}$ and velocity $\boldsymbol{v}$. However, because of the complexity of the collision term, it is not possible to evaluate the general kinetic Boltzmann equation, and approximate models must be derived.

The easiest and probably most famous solution is based on the assumption of an ideal (treating molecules as small, hard and perfectly elastic spheres) and homogeneous ($\partial f/\partial r = 0$) gas in absence of an external force ($\boldsymbol{a} = 0$) in equilibrium ($(\delta f/\delta t)_{coll} = 0$). These assumptions lead to the well known Maxwell-Boltzmann distribution $\phi_0(v)$, which describes the velocity distribution of non-interacting particles in a gas (Gombosi, 1994). In one dimension, the velocity distribution $\phi_0^{(1D)}(v)$ is given by (Hänel, 2004)

$$\phi_0^{(1D)}(v) = \frac{1}{\sqrt{2\pi}\, v_{th}} \exp\left(-\frac{v^2}{2\, {v_{th}}^2}\right) \tag{2.16}$$

where $v_{th} = (k_B\, T/M)^{1/2}$ is the thermal velocity, k_B the Boltzmann constant, T the gas temperature and M the mass of one molecule. Using the velocity distribution from

[7] A cubic centimeter on the Earth's surface contains $\approx 10^{19}$ molecules.

Eq. 2.16, it is possible to calculate the spectrum of scattered light $\mathcal{S}(f)$ by transforming the particle velocity into a frequency shift using the law of Doppler (Eq. 2.12; $\theta = 180°$, $n = 1$). If f is the frequency of the scattered light, λ_0 the wavelength of the incident light, and f_σ the standard deviation of the Gaussian function corresponding to v_{th}, the Doppler transformation is $v_{th} = (f_\sigma\,\lambda_0)/2$ and $v = (f\,\lambda_0)/2$. Therefore, $\mathcal{S}(f)$ is Gaussian function according to

$$\mathcal{S}(f) = \frac{1}{\sqrt{2\pi} f_\sigma} \frac{2}{\lambda_0} \exp\left(-\frac{f^2}{2\,{f_\sigma}^2}\right) \tag{2.17}$$

Although this equation is derived for an ideal gas, it also holds for dilute molecular gases in which the interaction between the different molecules are neglectable (Knudsen regime). However, the situation gets much more complicated for conditions in which collisions become dominant. In that case, the collision term on the right hand side of Eq. 2.15 has to be considered. Whereas one has only to consider translational energy conservation within the collision process in atomic gases, it is necessary to imply the internal energy (vibration and rotation) of the molecules and the possible change of it within the collision process in molecular gases. Thereby, one can distinguish between elastic collisions, in which the total translational energy of the colliding particles is conserved, and inelastic collisions, in which translational energy is transferred into internal energy (and vice versa). Therefore, in principle, the solution of the Boltzmann equation is determined by the cross section of elastic and inelastic collisions. But as no detailed knowledge about these cross sections is available, collision models must be devised.

Basically, collisions between molecules express the non-equilibrium state of the gas. In hydrodynamics it is this non-equilibrium state that leads to the macroscopic gas transport properties like thermal conductivity, shear and bulk viscosity (Curtiss, 1967). Therefore, a common approach is to construct the collision term in such a way that the different moments of the phase space distribution $f(\boldsymbol{v}, \boldsymbol{r}, t)$, which represent the dynamics of the gas under consideration (e.g., number density, flow velocity, internal energy, total energy, etc.), reproduce the known values of the transport coefficients (Gombosi, 1994). For the calculation of the transport coefficients of molecular gases, kinetic theories which take the internal degrees of freedom into account have to be used. The consideration of internal degrees of freedom can thereby be done in several ways.

A classical theory for describing the internal degrees of freedom of a molecule was first given by Taxman (1958), followed by a quantum mechanical treatment of molecules with internal degrees of freedom by Wang Chang et al. (1964). They carried the treat-

ment through to explicit expressions for the transport coefficients in terms of integrals of the differential cross sections. This treatment, however, is based on an assumed symmetry property of the differential cross section which is, in general, only true for non-degenerate molecular states. A more rigorous derivation of the quantum mechanical Boltzmann equation of a gas of rotating molecules was developed by Waldmann (1957) and Snider (1960).

Based on the linearized Wang-Chang-Uhlenbeck equation, Boley et al. (1972) and Tenti et al. (1974) described a model for the spectral line shape of scattered radiation, that has since then widely been applied for the retrieval of optical properties with high spectral resolution lidar (Esselborn et al., 2008; Hair et al., 2001, 2008) and wind speeds with Doppler wind lidar (Cézard et al., 2009; Dabas et al., 2008; Rye, 1998). Although the Tenti S6 model was developed for gases of a single-component molecular species, and not for gas mixtures such as air, it is considered as the most appropriate model for atmospheric conditions (Miles et al., 2001; Young and Kattawar, 1983).

2.3.1 Derivation of the Tenti S6 model

The intention of this section is to give an overview of the basic concept of deriving the Tenti S6 line shape model, which is commonly used to describe the spectra of molecular scattered light. The complete derivation is given by Boley et al. (1972) and Tenti et al. (1974).

Starting point for deriving the Tenti S6 line shape model is the kinetic equation by Wang Chang et al. (1964) (WCU) which delivers a set of equations that describe the dynamics of the distribution function $f_i(\boldsymbol{v}, \boldsymbol{r}, t)$ of each internal state i

$$\left(\frac{\partial}{\partial t} + \boldsymbol{v}\frac{\partial}{\partial \boldsymbol{r}}\right) f_i(\boldsymbol{v}, \boldsymbol{r}, t) = \sum_{jkl} \int_{-\infty}^{\infty} \int_{\Omega} \left(f'_k f'_l - f_i f_j\right) |v - v_1| \, \sigma_{ij}^{kl} \, d^3 v_1 \, d\Omega \tag{2.18}$$

where the subscript i labels the entire set of quantum numbers necessary to specify the internal state of the molecule, and $d\Omega$ is the solid angle element.

The left hand side of the WCU equation is already introduced by Eq. 2.15 (without considering any acceleration $\boldsymbol{a}$ due to an external force), and the collision term on the right hand side describes the change in particle number in the considered phase space. In particular, the collision integral considers the collision between two particles,

where one particle with velocity v and internal state i transits to state k and velocity v' after collision. The second particle has velocity v_1 and state j before the collision and transits to state l and velocity v_1' after collision. Thereby, the collision cross section $\sigma_{ij}^{kl}(v, v_1, v', v_1')$ depends on the internal energy levels involved in the collision, as well as on the relative velocity of the two particles. The collision term in Eq. 2.18 involves effects of elastic collisions, where $k = i$ and $l = j$, as well as inelastic collisions, where $k \neq i$ and $l \neq j$. To get the amount of particle number changes within the considered phase volume due to collisions, the collision term in Eq. 2.18 is integrated over all velocities v and all solid angles $d\Omega$ and additionally summed up over the internal states j, k, l. There is no summation over i.

The derivation of the WCU equation follows the same arguments used in the derivation of the Boltzmann equation. It is based on the assumption that only binary collisions between two particles are important and that previous collisions do not influence subsequent collision probabilities. Furthermore, the WCU equation satisfies the conservation of mass, momentum, and total energy. As the nonlinear WCU is hard to handle, further assumptions must be made to end up at a solution of Eq. 2.18:

- As the collisions between molecules only cause small deviations from equilibrium, $f_i(\boldsymbol{v}, \boldsymbol{r}, t)$ can be linearized around equilibrium according to

$$f_i(\boldsymbol{v}, \boldsymbol{r}, t) = n x_i \phi_0(v) \left[1 + h_i(\boldsymbol{v}, \boldsymbol{r}, t)\right] \tag{2.19}$$

  where $h_i(\boldsymbol{v}, \boldsymbol{r}, t)$ is the dimensionless deviation from equilibrium, n is the average number density, x_i the average fraction of molecules with internal energy E_i[8] with

$$x_i = \frac{\exp -E_i/k_B T}{\sum_j \exp -E_j/k_B T} \tag{2.20}$$

  and $\phi_0(v)$ is the Maxwell-Boltzmann distribution

$$\phi_0(v) = \left(\frac{1}{\pi {v_0}^2}\right)^{3/2} \exp\left(-\frac{v^2}{{v_0}^2}\right) \tag{2.21}$$

- The macroscopic transport properties such as shear viscosity, bulk viscosity and heat conductivity are determined by the velocity moments of the deviation from thermal equilibrium $h_i(\boldsymbol{v}, \boldsymbol{r}, t)$ (e.g., number density, flow velocity, translational

[8] It should be noted that there is no consideration of degeneracy of internal energy levels.

temperature (Boley et al., 1972)). As the collision cross section $\sigma_{ij}^{kl}(v, v_1, v', v_1')$ is not known, the entire collision integral is linearized and constructed such that it reproduces the known values of gas transport properties. The complicated and tedious development of the collision operator $\boldsymbol{J}$ is extensively described by Boley et al. (1972).

Therefore, the deviations $h_i(\boldsymbol{v}, \boldsymbol{r}, t)$ are only small, it is possible to plug Eq. 2.19 into Eq. 2.18 which leads to

$$\left(\frac{\partial}{\partial t} + \boldsymbol{v}\frac{\partial}{\partial \boldsymbol{r}}\right)\boldsymbol{h} = n\,\boldsymbol{J}\,\boldsymbol{h} \tag{2.22}$$

Now, Eq. 2.22 is used to generate a linear system of equations, by expanding $\boldsymbol{h}$ into eigenfunctions of $\boldsymbol{J}$. In other words: the microscopic deviations from equilibrium are defined such that they reproduce the macroscopic transport coefficients, as they are valid in hydrodynamics.

A line shape model results after truncation of the expansion to six or seven terms. The Tenti S6 model truncates, as the name implies, the expansion after 6 terms. Though Boley et al. (1972) first developed a 7 moment model[9], they showed that their 6 moment model provides the superior fit of experimental line shapes. This was recently confirmed by Vieitez et al. (2010b).

As all combinations of matrix elements which enter into Eq. 2.22 can be expressed in terms of the gas transport coefficients of shear viscosity η, bulk viscosity η_b, and thermal conductivity κ, the spectrum calculation contains no adjustable parameter. It is completely defined by four dimensionless parameters x, y, z, f, according to

$$x = \frac{\omega}{k_\mathrm{s}\, v_0}, \quad y = \frac{p}{k_\mathrm{s}\, v_0\, \eta}, \quad z = \frac{3\,\eta_b}{2\,\eta\,\gamma_\mathrm{int}}, \quad f = \frac{m\,\kappa}{\eta\, k_B (3/2 + c_\mathrm{int})} \tag{2.23}$$

where ω is the angular frequency of the incident light, p is the gas pressure, c_int the internal specific heat per molecule divided by k_B, $\gamma_\mathrm{int} = c_\mathrm{int}/(3/2 + c_\mathrm{int})$, k_s is the magnitude of the interacting wave vector (see also Eq. 2.10), and $v_0 = (2\,k_B\,T/M)^{(1/2)}$ the most probable thermal velocity (with k_B being the Boltzmann's constant, M the mass of one molecule and T the gas temperature).

The FORTRAN code which is used to calculate the Tenti S6 model was kindly provided by Xingguo Pan, and implemented and modified by Willem van de Water (consideration of temperature dependence of gas transport coefficients). The entire code of the Tenti S6 model can be found in the Appendix C of the PhD thesis by Forkey (1996).

[9] The 7 moment of Boley et al. (1972) additionally considers the traceless pressure tensor, which is not considered in their later developed 6 moment model (Tenti et al., 1974).

2.3.2 Physical limitations of the Tenti S6 model

In the 1960s and 1970s, a handful of line shape models for monoatomic and polyatomic gases were developed (Boley et al., 1972; Mountain, 1966; Sugawara and Yip, 1967; Tenti et al., 1974). In contrast to the models for monoatomic gases, the models for polyatomic gases must additionally consider the internal degrees of freedom of a molecule. Whereas Sugawara and Yip (1967) used the relaxation frequency of molecules as an adjustable parameter to achieve accordance between model and experimental data, Tenti et al. (1974) developed their model without considering any adjustable parameters[10].

Recently, Zheng (2007) theoretically developed a line shape model (Q9 model) which is based on the Waldmann-Snider equation, and therefore on the correct quantum mechanical kinetic theory for a molecular gas (section 2.3). He shows a comparison to the Tenti model and points out that there is no significant difference between both models for atmospheric relevant conditions. The Q9 model furthermore enables to calculate the depolarized part of the scattered light (rotational Raman Q-branch, section 2.2). However, Zheng makes no comparison to experimental data, which would be needed to verify if there is an improvement of describing SRB line shapes by using the Q9 model.

As the Tenti model is developed on solid physical background, and as it shows the best accordance to experimental data obtained in molecular gases (see section 3.1), it is viewed as the best model to describe the Cabannes line of molecular scattered light (Young and Kattawar, 1983). However, also the Tenti model has limitations because of its approximative nature. These limitations affect the application in both, molecular gases in general, and gas mixtures like air in particular. These limitations and their possible impacts are discussed in the following.

First to mention is, that the collision integral of the Tenti model is designed to describe the collisions between molecules of the same species. However, air is a mixture of several gases and each of the individual components has its own molecular structure and its own molecular cross section. Moreover, if the different components of the mixture have different masses, or different collision cross sections, another relaxation mechanism arises when equilibration of translational energy between the species requires several collision times. But as air is mainly composed of N_2 and O_2, which are quite similar molecules with respect to their structure, mass, and also their transport properties, the impact

[10] The Tenti model only depends on four dimensionless parameters (Eq. 2.23) which themselves only depend on gas transport properties.

of different collision effects is assumed to be small. Anyway, there is an urgent need to verify this circumstance. For comparing the presented SRB measurements in air (section 3.3) to the Tenti S6 model, we will treat air as an "effective" medium, consisting of molecules with an effective mass whose collisions are parametrized by effective transport coefficients. The gas transport properties of air, used for Tenti S6 model calculation can be found in Table A.1.

Secondly, the Tenti model does not account for molecules with degenerate internal states as they are not considered in the WCU equation (section 2.3.1). Degenerate states in molecules are shown to have an influence on the transport properties, in particular thermal conductivity and shear viscosity (Senftleben-Beenakker effect), and this may lead to a change in the SRB line shape. However, as there are only scalar properties of gas transport properties considered, the influence is assumed to be neglectable (Knaap and Lallemand, 1975). This assumption is supported by experiments on the Senftleben-Beenakker effect which show that the electric and magnetic field effects on the scalar transport coefficients are less than 1 % (Boley et al., 1972).

Thirdly, by deriving the Tenti model one makes use of the fact that the intensity of the scattered light is proportional to the space-time Fourier transform of the density-density correlation function (Van Hove, 1954). In particular, this is only true for the coherently scattered light[11]. As previously discussed in section 2.1.2, there is also an unshifted incoherently scattered part which is due to rotational Raman scattering (Q-branch of the rotational Raman scattering). This part makes about 0.7 % of the scattered light intensity and is not considered by the Tenti model.

Fourthly, the Tenti S6 model uses known values of the transport coefficients (shear viscosity, thermal conductivity, heat capacity, bulk viscosity) to parametrize the collision integral in the linearized WCU equation, and therefore, to describe the spectral distribution of the scattered light. This means that the calculated SRB line shape depends directly on the accurate knowledge of these transport coefficients. Wakeham (1986) reviewed the status of the study of transport properties of polyatomic gases and pointed out that the shear viscosity as well as the thermal conductivity can be measured with

[11] Here, "coherent" means that the light is scattered from "dipoles" which are oscillating in phase, and therefore, the differential cross section of the scattered light is proportional to N^2, where N is the number of scatterers. The scattering cross section of incoherent scattered light is proportional to N.

an accuracy of better than 1 % and that data is available for almost all diatomic gases. In contrast to that, the bulk viscosity determination for molecular gases is quite error-prone, which leads to a serious shortage in bulk viscosity data (Emanuel, 1990).

The bulk viscosity in a molecular gas quantifies the resistance to rapid compression, and has its origin in the relaxation of the energy involving internal degrees of freedom of molecules to a change of the kinetic energy. In case of thermal equilibrium, the internal and the kinetic temperature are the same, but it may take many collisions to equilibrate the two. Therefore, the bulk viscosity depends on the structure of a molecule and is essentially frequency-dependent (Graves and Argrow, 1999; Meador et al., 1996). Practically, there is only one single measurement technique available for bulk viscosity (Prangsma et al., 1973), which utilizes sound absorption measurements. Using the classical hydrodynamic theory (Herzfeld et al., 1959), the absorption coefficient α_{tot} of a polyatomic gas is given by a combination of the so-called classical contribution α_{cla} which is due to thermal conductivity and shear viscosity and the so-called excess contribution α_{exc} which is due to the bulk viscosity,

$$\alpha_{\mathrm{cla}} = \frac{2\pi^2 f^2}{\rho c_{\mathrm{s}}^3}\left(\frac{4}{3}\eta + \left(\frac{1}{c_{\mathrm{v}}} - \frac{1}{c_{\mathrm{p}}}\right)\kappa\right) \qquad \text{and} \qquad \alpha_{\mathrm{exc}} = \frac{2\pi^2 f^2}{\rho c_{\mathrm{s}}^3}\eta_b \tag{2.24}$$

and therefore,

$$\alpha_{\mathrm{tot}} = \alpha_{\mathrm{cla}} + \alpha_{\mathrm{exc}} = \frac{2\pi^2 f^2}{\rho c_{\mathrm{s}}^3}\left(\frac{4}{3}\eta + \left(\frac{1}{c_{\mathrm{v}}} - \frac{1}{c_{\mathrm{p}}}\right)\kappa + \eta_b\right) \tag{2.25}$$

where f is the sound frequency, c_{v} and c_{p} are the specific heats, c_{s} the isentropic speed of sound, and ρ the density of the medium, η the shear and η_b the bulk viscosity, and κ the thermal conductivity. Therefore, the bulk viscosity can be obtained by subtracting the classical contribution from the total sound absorption intensity. Since the bulk viscosity contribution to the total sound absorption is small[12], and since the uncertainties of the other quantities in Eq. 2.25 (ρ, η, c_{s}, f, κ) directly act to the uncertainty of η_b, this indirect measurement technique implicates a remarkable inaccuracy. The experimental errors are found to range up to typically 25 % or even larger (Rah and Eu, 2001).

Whereas these large errors might not play a big role for atmospheric applications where the y value, and therefore, the sensitivity of the SRB line shape to the bulk viscosity is small (see section 2.3.3), there will be a remarkable influence on SRB line shapes at larger y values.

[12] Using the transport coefficients of air (Table A.1, $c_{\mathrm{v}} = 743\frac{\mathrm{J}}{\mathrm{kg\,K}}$ and $c_{\mathrm{p}} = 1014\frac{\mathrm{J}}{\mathrm{kg\,K}}$), α_{exc} due to bulk viscosity is about one third of the total sound absorption α_{tot}.

This situation is illustrated by simulated SRB line shapes according to the Tenti S6 model for ultraviolet light ($\lambda = 355$ nm), backscattered ($\theta = 180°$) in nitrogen ($p = 3000$ hPa, $T = 288$ K) for different bulk viscosity values (Fig. 2.5). The black line represents the SRB line shape which is calculated for the reference value of $\eta_b = 1.4 \cdot 10^{-5}\,\mathrm{kg\,m^{-1}s^{-1}}$ (Witschas et al., 2010), whereas the blue and the red line indicate the SRB line shapes for ±25 % deviation. Thus, they are calculated for $\eta_b = 1.05 \cdot 10^{-5}\,\mathrm{kg\,m^{-1}s^{-1}}$ and $\eta_b = 1.75 \cdot 10^{-5}\,\mathrm{kg\,m^{-1}s^{-1}}$, respectively. It gets clearly obvious that 25 % error in bulk viscosity causes a significant change in line shape, especially at the spectral position of the Brillouin peaks which are caused from scattering on sound waves. This error is a large uncertainty in Tenti line shape modeling, especially for larger y values where the influence of Brillouin scattering is more prominent.

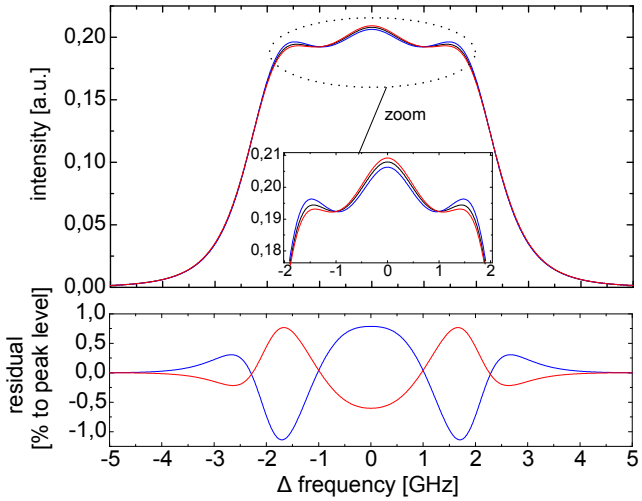

Figure 2.5: Top: Tenti modeled SRB line shapes in nitrogen ($p = 3000$ hPa, $T = 288$ K, $\lambda = 355$ nm, $\theta = 180°$) for different bulk viscosity values. The spectrum which is represented by the black line is calculated for $\eta_b = 1.4 \cdot 10^{-5}\,\mathrm{kg\,m^{-1}s^{-1}}$. The blue and red line represent SRB line shapes which are calculated for 25 % deviation, that is, $\eta_b = 1.05 \cdot 10^{-5}\,\mathrm{kg\,m^{-1}s^{-1}}$ and $\eta_b = 1.75 \cdot 10^{-5}\,\mathrm{kg\,m^{-1}s^{-1}}$, respectively. Curves are normalized to yield unity integrated intensity. The gas transport parameters that are used for simulation can be found in Table A.1. Bottom: The difference between the red and the black line, and the blue and the black line is given as a percentage deviation compared to the intensity at Δfrequency = 0 Hz.

Another problem is that the sound absorption measurements for bulk viscosity determination are performed at acoustic frequencies up to 10^6 Hz, while light scattering involves frequencies which are three orders of magnitude larger. As the bulk viscosity is strongly frequency dependent (Mountain, 1966), its value at frequencies in the order of GHz must be considered largely unknown.

For atmospheric applications it is furthermore necessary to investigate to role of water vapor content in air, which can reach up to 4 vol. % within the atmosphere (e.g., tropical

conditions with water vapor saturated air, p = 1013 hPa, T = 30° C). Thus, water vapor might be the largest contributer to air after N_2 and O_2. Water vapor is known to have a large and frequency-dependent influence on the damping of sound. According to sound absorption measurements (Bass et al., 1990), the bulk viscosity of water vapor saturated air at frequencies in the order of 10 kHz is one order of magnitude larger than that of dry air. These trends are illustrated in Fig. 2.6 which shows the bulk viscosity for water vapor saturated air (solid line) and dry air (dashed line) depending on sound frequency, based on an empirical formula by Bass et al. (1984).

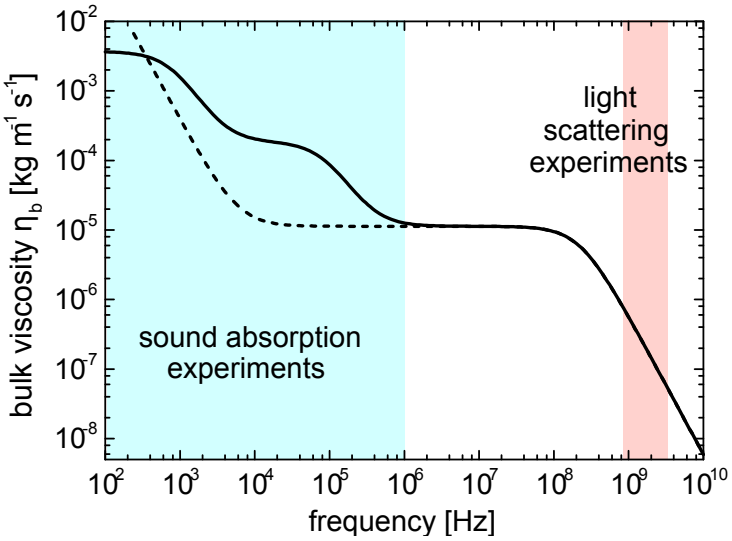

Figure 2.6: Bulk viscosity η_b of dry air (dashed line) and water saturated air (solid line) as a function of frequency. The lines represent an empirical formula that is based on sound absorption measurements with sound frequencies up to 10^5 Hz by Bass et al. (1984). The frequency range where sound absorption measurements are performed is indicated by the blue area. The frequency range relevant for light scattering is indicated by the red area. The largest frequency considered in the formula is the rotational relaxation frequency of N_2 and O_2, after which the bulk viscosity drops to zero. While this might be adequate for the acoustical frequencies for which this formula was designed, it is unrealistic at sound frequencies corresponding to optical wavelengths.

The largest frequency considered in the formula used to calculate Fig. 2.6 is the rotational relaxation frequency of N_2 and O_2, after which the bulk viscosity drops to zero. While this might be adequate for the acoustical frequencies for which this formula was designed, it is unrealistic at sound frequencies corresponding to optical wavelengths. Figure 2.6 also suggests that the influence of water vapor is restricted to low frequencies; but it should be realized that the contribution of the relaxation process at much higher frequencies is not known.

To confirm that the previously mentioned limitations do only have a minor influence on the line shape prediction using the Tenti S6 model, a verification with high resolution experimental data is urgently needed. Therefore, Rayleigh-Brillouin scattering measurements were performed in laboratory (chapter 3) as well as in the "real" atmosphere (chapter 4) and are additionally used to verify the Tenti S6 model.

2.3.3 Tenti S6 model sensitivity to gas transport parameter uncertainties

In section 2.3.1 it was pointed out that the Tenti model uses macroscopic gas transport properties to extract information about the microscopic condition of the gas, and therefore, about the spectrum of the scattered light. For applications which utilize the spectrum of the scattered light to derive gas properties, it is therefore of special interest in which way and magnitude the various transport coefficients influence the modeled line shape. To clarify this topic, a sensitivity analysis for all relevant parameters used in the Tenti model (T, p, η, η_b, κ) was performed.

Therefore, a set of Tenti reference spectra $\mathcal{S}_{\mathrm{ref}}(f_i)$ was calculated for different y values relevant for atmospheric applications (0.126, 0.201, 0.376, 0.751, 1.127)[13] and literature gas transport properties (Table A.1, Fig. 2.7).

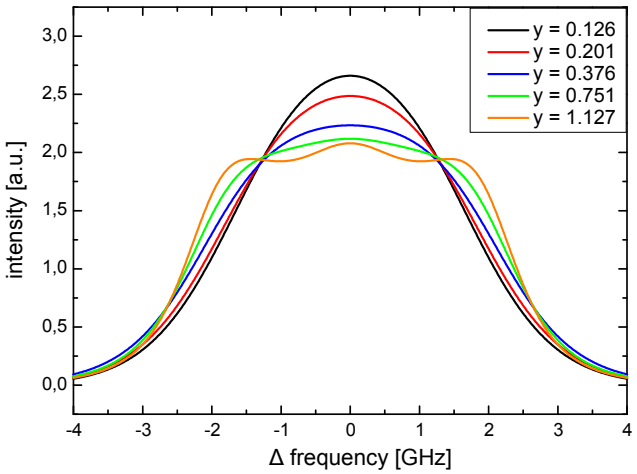

Figure 2.7: SRB reference spectra $\mathcal{S}_{\mathrm{dev}}(f)$ for y values of 0.126 (black), 0.201 (top, red), 0.376 (blue), 0.751 (green), 1.127 (orange) used for sensitivity analysis. The spectra are calculated using the Tenti S6 model and literature transport coefficients of nitrogen (Table A.1). Spectra are normalized to yield equal integrated intensity.

[13] The values which reach the presented y values are chosen to represent atmospheric conditions, and are summarized in Table A.2

These line shapes are compared to Tenti spectra $\mathcal{S}_{\mathrm{dev}}(f_i)$ which are calculated with slightly deviated gas transport properties. The deviations were chosen to be in the order of the uncertainties as they are common for SRB measurements ($\Delta T = \pm 1\,\mathrm{K}$, $\Delta p = \pm 10\,\mathrm{hPa}$, $\Delta\eta = \pm 1\,\%$ of η_{ref}, $\Delta\eta_b = \pm 25\,\%$ of $\eta_{\mathrm{b_{ref}}}$, and $\Delta\kappa = \pm 1\,\%$ of κ_{ref}). For this analysis, only one single parameter is changed for each comparison. Both $\mathcal{S}_{\mathrm{ref}}(f_i)$ and $\mathcal{S}_{\mathrm{dev}}(f_i)$ are simulated for a frequency range of ± 5 GHz and 1024 points. Therefore the frequency resolution is 9.77 MHz.

The magnitude of influence is characterized by

$$\Delta\mathcal{S}^2 = (1/N)\sum_{i=1}^{N}\left(\frac{\mathcal{S}_{\mathrm{dev}}(f_i) - \mathcal{S}_{\mathrm{ref}}(f_i)}{\mathcal{S}_{\mathrm{ref}}(f_i)}\right)^2 \tag{2.26}$$

which can be viewed as "the change" of line shape. The result of this comparison is depicted in Fig. 2.8 for different y parameters and for pressure, temperature, shear viscosity, bulk viscosity and thermal conductivity deviations.

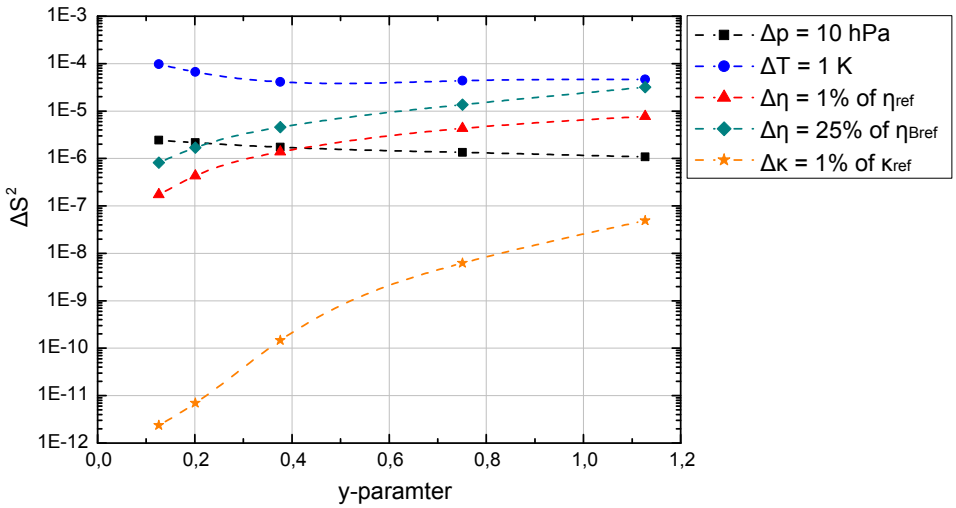

Figure 2.8: Tenti model line shape sensitivity to gas transport property variations. The least square difference according to Eq. 2.26 is calculated using the reference spectra from Fig. 2.7 and considering deviations in pressure ($\Delta p = \pm 10$ hPa), temperature ($\Delta T = \pm 1$ K), shear viscosity ($\Delta\eta = \pm 1\,\%$ of η_{ref}), bulk viscosity ($\Delta\eta_b = \pm 1\,\%$ of $\eta_{\mathrm{b_{ref}}}$) and thermal conductivity ($\Delta\kappa = \pm 1\,\%$ of κ_{ref}). The result is indicated by black squares, blue circles, red triangles, green diamonds and yellow stars, respectively.

Whereas the influence of temperature and pressure variations on the line shape is almost independent of the y parameter, the influence of an uncertainty in transport parameter knowledge increases for increasing y values. For example, at lidar measurements with ultraviolet light ($y = 0$ to 0.4), the influence of the thermal conductivity uncertainty

is neglectable, as it is leads to a least square difference which is at least three orders of magnitude smaller than the one of the other parameters. However, uncertainties in shear and bulk viscosity lead to a least square difference which is in the order of the one of temperature and pressure uncertainties at $y = 0.4$. For larger y values, the influence of a bulk viscosity uncertainty of 25 % is even in the order of a temperature uncertainty of 1 K.

2.4 Summary

The origin of molecular light scattering mechanisms as well as their impact on the spectrum of the scattered light were discussed to enable the reader to distinguish between the effect of Rayleigh-Brillouin scattering mainly investigated in this thesis and other scattering mechanisms like Raman scattering (section 2.1).

It was pointed out that the differential cross section of Rayleigh-Brillouin scattered light is 2 to 3 orders of magnitude larger than that of rotational and vibrational-rotational Raman scattered light, which is one of the main reasons why the Rayleigh-Brillouin spectrum is preferentially used in atmospheric applications (section 2.2).

Furthermore, it was demonstrated that the line shape of Rayleigh-Brillouin scattered light sensitively depends on the actual gas condition. In particular, it mainly depends on the gas temperature and pressure, but also on the gas transport properties like viscosity, bulk viscosity and thermal conductivity (section 2.3.1). This means that a precise knowledge of these quantities is needed for an accurate description of the Rayleigh-Brillouin line shape. It is highlighted that this accurate knowledge is not warranted in case of the bulk viscosity (section 2.3.2).

Additionally, the derivation as well as the limitations of the currently best available model for describing the Rayleigh-Brillouin line shape in molecular gases (Tenti S6 model (Tenti et al., 1974)) were discussed (section 2.3) to enable the reader the possibility to see the strength of the Tenti S6 model, but also to demonstrate that there are some points which urgently have to be investigated before using the Tenti S6 model in atmospheric applications without any doubt.

The main goal of this thesis is therefore to perform Rayleigh-Brillouin experiments that lead to highly resolved Rayleigh-Brillouin line shapes which enable an accurate validation of the Tenti S6 model, and thus, the verification if the discussed limitations are significant and crucial for atmospheric applications.

Chapter 3

Investigation of spontaneous Rayleigh-Brillouin scattering of ultraviolet light in N_2, dry and humid air in laboratory experiments

3.1 Introduction

Atmospheric lidar techniques for the measurement of wind (Dabas et al., 2008; Gentry et al., 2000; McGill et al., 1997b; Reitebuch et al., 2009), temperature (Liu et al., 2009b; Shimizu et al., 1986), and aerosols (Eloranta, 2005; Esselborn et al., 2008; Fiocco and DeWolf, 1968; Liu et al., 2009a) as well as non-intrusive measurement techniques for temperature, density (Elliott et al., 2001), and bulk velocity (Seasholtz et al., 1997) in gas flows rely on the exact knowledge of the spectral line shape (Cabannes line) of the scattered light. The best model which is available to describe this spectral line shape is the Tenti S6 model (section 2.3). However, the Tenti model implies general limitations because of its approximative derivation as well as limitations for the application of describing line shapes of light scattered in gas mixtures such as air (section 2.3.2). Though the Tenti model is used to describe the line shape of scattered light in atmospheric applications (Dabas et al., 2008; Liu et al., 2009a,b; Reitebuch et al., 2009), this approach has not been validated with measurements in air.

The first spontaneous Rayleigh-Brillouin (SRB) scattering experiments in molecular and noble gases were performed in the 1960s and 1970s, as the invention of the laser and the improvement of Fabry-Perot interferometers (FPI) provided the frequency resolution which is needed to resolve the Cabannes line of molecular scattered light. The main

objectives of these measurements were to use the experimental data to obtain information about the molecular velocity distribution function, and therefore, about the dynamics in fluids and gases, and to test the validity of various theoretical solutions of the Boltzmann equation (Eq. 2.15) (Boley et al., 1972; Mountain, 1966; Sugawara and Yip, 1967; Tenti et al., 1974). The basic concept of these measurements is to send laser light through a gas sample, collect the scattered light at a certain angle, and resolve the spectrum of the scattered light using a FPI and a photomultiplier tube.

Greytak and Benedek (1966) used a frequency stabilized He-Ne laser ($\lambda = 632.8$ nm, P = 0.6 mW) to investigate SRB scattering of several gases (Ar, Xe, N_2, CH_4 and CO_2) at room temperature and atmospheric pressure. They observed the scattered light at angles of 10.6°, 22.9° and 169.4° and resolved the spectrum using both a plan parallel FPI ($\Delta f_{FWHM} = 153$ MHz, $\Gamma_{FSR} = 5$ GHz), and a spherical FPI ($\Delta f_{FWHM} = 28$ MHz, $\Gamma_{FSR} = 0.75$ GHz). They used their data to obtain the velocity of sound in the mentioned gases by comparing their measured SRB line shapes to the hydrodynamic line shape model by Mountain (1966).

Hara et al. (1971) investigated the SRB spectrum of the three isotopic variants of hydrogen (H_2, HD and D_2) at room temperature, and a scattering angle of 90°. They used a He-Ne laser ($\lambda = 632.8$ nm, P = 15 mW) and a pressure scanned, plan-parallel FPI ($\Gamma_{FSR} = 15$ GHz and $\Delta f_{FWHM} = 300$ MHz for H_2 experiments, and $\Gamma_{FSR} = 10$ GHz and $\Delta f_{FWHM} = 200$ MHz for HD and D_2 experiments), and derived the velocity of sound by comparing the measured SRB line shapes to the hydrodynamic model by Mountain (1966). They furthermore showed a good agreement between the measured SRB line shapes in the kinetic regime ($y < 1$) and the kinetic model by Sugawara and Yip (1967), however, they did not quantify this agreement.

Sandoval and Armstrong (1976) studied Rayleigh-Brillouin scattering in N_2 at room temperature and pressures between 1 hPa and 881 hPa using a He-Ne laser ($\lambda =$ 632.8 nm). The scattering angle was 15°. Thus, the measured SRB line shapes cover the Knudsen regime ($y = 0.007$), the kinetic regime ($y = 0.55$ to 1.50), as well as the hydrodynamic regime ($y = 4.39$). They used a piezo-electrically scanned spherical FPI ($\Delta f_{FWHM} = 40$ MHz) for resolving the SRB line shapes, compared them to the line shape model by Sugawara and Yip (1967) and observed remarkable differences between model and measurement. These differences are only visible within the figures, but are not quantitatively demonstrated.

Lao et al. (1976) investigated SRB scattering in a number of gases (N_2, CO_2, C_2F_6, C_2H_6) and a He-Kr mixture at various pressures (100 hPa to 22000 hPa) and room

temperature. They used a Ar-ion laser ($\lambda = 514.5$ nm, P = 500 mW), scattering angles of 60° and 90° and a piezo-electrically scanned FPI ($\Delta f_{FWHM} = 31$ MHz, $\Gamma_{FSR} = 2$ GHz) in their setup. The measured spectra were analyzed with the hydrodynamic line shape model by Mountain (1966) and Weinberg et al. (1973). Furthermore, they used one of their N_2 measurements ($\theta = 60°$, T = 302 K, $y = 11.2$) in the hydrodynamic regime to compare it to the Tenti S6 model (Tenti et al., 1974) and showed a good agreement between measurement and model. But they did not verify this agreement by any significance test and did not show a residual between measurement and model.

Ghaem-Maghami and May (1980) investigated the SRB spectrum in both the kinetic and the hydrodynamic regime of the noble gases He, Ne, and Ar by using an Ar-ion laser ($\lambda = 514.5$ nm, P = 500 mW), and a scattering angle of 90°. They used the measured SRB line shapes to investigate the accuracy of line shape scaling by using the dimensionless parameters x and y (section 2.3.1, Eq. 2.23) and found that, in the kinetic regime, the spectra can be scaled to the 3 % accuracy level.

Lock et al. (1992) used an Ar-ion laser ($\lambda = 514.5$ nm, P = 400 mW) and a plan parallel FPI to investigate SRB scattering in N_2 at room temperature and 600 K ($\theta = 90°$). In contrast to the previously mentioned experiments, they used a CCD camera and the fringe-imaging technique for detecting the light passing through the FPI. Though they compared their N_2 measurements to the Tenti S6 model, they did not show any of the measured spectra. They concluded that the temperature determination by fitting the Tenti S6 model to the measured line shape has an accuracy of about 10 %.

SRB scattering experiments on binary gas mixtures of noble gases and mixtures of He with H_2 and D_2 were done by Letamendia et al. (1981, 1982). They used a Ar-ion laser ($\lambda = 514.5$ nm, P = 800 mW), a piezo-electrically scanned FPI ($\Delta f_{FWHM} = 20$ MHz, $\Gamma_{FSR} = 1$ GHz), and scattering angles varying between 30° and 150°. They compared their measurements to hydrodynamic and kinetic line shape models they developed by themselves, and pointed out that the description of the SRB line shapes obtained in gas mixtures is quite dubious.

In connection to SRB scattering a quite recent measurement technique proposed by She et al. (1983, 1985) and termed stimulated, or coherent Rayleigh-Brillouin (CRB) scattering might be mentioned. At CRB scattering, the density fluctuations that are responsible for light scattering are not spontaneous due to the random thermal motion of molecules, but are induced by optical dipole forces using two crossing laser beams (Pan et al., 2004b; She et al., 1983). As the density fluctuations at CRB scattering are caused by an

external dipole force which directly acts to the molecular dynamics (see also Eq. 2.15), the CRB line shape differs from the SRB line shape (for otherwise identical conditions). Grinstead and Barker (2000) experimentally determined the CRB line shape in N_2 in the Knudsen regime (p = 6.6 kPa, T = 208 K), whereas Pan et al. performed measurements in several gases (Ar, Kr, CO_2, N_2, O_2) at room temperature and various pressures representing the kinetic regime (Pan et al., 2005, 2002, 2004b). Pan et al. (2004b) also developed a model based on the same assumptions as those of the Tenti model (but for CRB line shapes)[1], and showed a good agreement to their measurements.

Anyway, none of the previously performed SRB measurements on N_2 at atmospheric conditions (e.g. $y \approx 0.1$ to 1.1 for standard atmospheric conditions (US Standard Atmosphere, 1976), $\lambda = 355$ to 1064 nm, $\theta = 180°$) were compared to the Tenti S6 model, and no SRB measurements have yet been performed on air as a gas mixture. In order to quantify precisely the line shape of light scattering in air, there is an urgent need for precise data and validation of commonly used line shape models, i.e., the Tenti S6 model. In addition, the influence of water molecules on the line shape has to be investigated, as water vapor is the most relevant air constituent among N_2 and O_2 within the lower troposphere. In the past, Bass et al. (1990, 1995, 1996) demonstrated that water molecules have a very large influence on sound damping at frequencies from 10 Hz to 100 kHz. As sound waves are the origin of the Brillouin scattering mechanism, it is a question whether this influence extends to the GHz frequency range which is relevant for light scattering (section 2.3.2).

In this chapter, high-precision Rayleigh-Brillouin scattering experiments on N_2 as well as on dry and water vapor-saturated air are presented and used to investigate the accuracy of the Tenti S6 model[2]. In contrast to earlier Rayleigh-Brillouin scattering experiments in the visible spectral region, these measurements are performed in the ultraviolet, which is widely used for direct-detection DWL (Gentry et al., 2000; Reitebuch et al., 2009) including the lidar on ADM-Aeolus (European Space Agency, 2008) and the HSRL on EarthCARE (European Space Agency, 2004) which use a wavelength of 355 nm. For technical reasons the present study employs a wavelength of 366 nm and a scattering

[1] Pan et al. also use the linearized WCU for the derivation of their CRB line shape model. In contrary to the Tenti model used for SRB line shapes, they also have to consider an acceleration to the molecules, caused by the optical dipole force of the two crossing laser beams, in the linearized Boltzmann equation (Eq.2.15). The precise description of their CRB line shape model development can be found in (Pan et al., 2004b).

[2] Parts of this chapter are already partly published in Witschas et al. (2010).

angle of 90° (section 3.2.1). In view of the relatively small wavelength difference the obtained results should, after scaling for the wavelength, be applicable for the case of 355 nm, and probably also for other laser wavelengths. However, the frequency dependence of the bulk viscosity (section 3.3.1) should be investigated in that case. Furthermore, the obtained results are also scalable to other scattering angles, temperatures and pressures by the y-parameter (Eq. 2.14), for instance 180° as used in lidar measurements. However, the temperature dependence of the gas transport coefficients has to be considered in the latter case.

3.2 Experimental details

3.2.1 Setup

A block diagram of the experimental setup designed and arranged by Vieitez et al. (Vieitez et al., 2010a) at Vrije Universiteit Amsterdam is shown in Fig. 3.1.

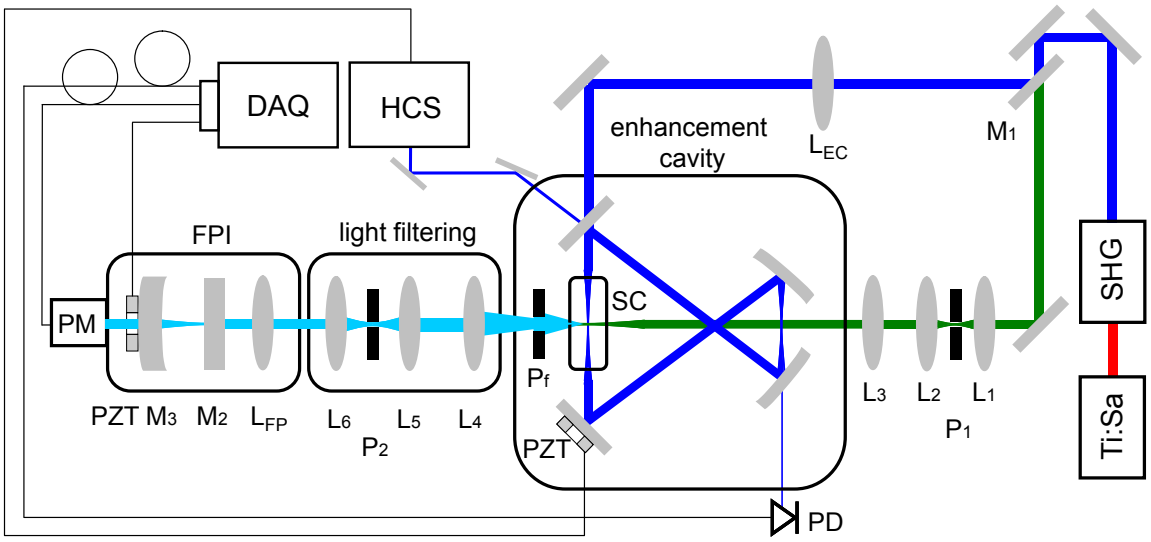

Figure 3.1: Schematic diagram of the experimental setup: red: Ti:Sa laser beam (732 nm); dark blue: UV beam (366 nm); light blue: scattered radiation; green: reference beam (≈ 1 % of the main UV beam intensity); L_x: lenses; M_x: mirrors; P_x: pinholes; PD: photo diode; PZT: piezo-electrical translator; SC: scattering cell; SHG: second harmonic generation; PM: photo multiplier; DAQ: data acquisition; HCS: Hänsch-Couillaud stabilization scheme; FPI: Fabry-Perot interferometer. Detailed description of the setup is given in the text.

The measured line shape of scattered radiation is the result of the convolution of the molecular spectral line shape and the instrument function, which itself is the result of the convolution of the line width function of the laser and the transmission function of

the Fabry-Perot interferometer. To avoid an influence of the laser bandwidth on the detected signal, a narrowband, continuous-wave, single longitudinal mode laser is used. The laser is a titanium sapphire laser (Fig. 3.1, Ti:Sa, red line) which is pumped by a frequency doubled Nd:YVO_4 laser (Millennia), delivering single-mode continuous wave radiation at 732 nm wavelength with an output power of 1.5 W. The laser bandwidth is 1 MHz (at 732 nm) and the long-term frequency drift was measured with a wavelength meter (Atos - LM-007) to be smaller than 10 MHz per hour (at 732 nm).

To reach the desired UV radiation, the frequency of the Ti:Sa laser light is doubled in a non-linear optical crystal (second harmonic generation, Fig. 3.1, SHG). Therefore, the conversion efficiency in the frequency doubling process of continuous wave radiation is only a small number between 10^{-5} and 10^{-2} (Cruz and Cruz, 2007), the crystal is placed in a bow-tie shaped enhancement cavity to increase the arising UV power. In principle, the enhancement cavity ensures that the light wave travels many round trips, and therefore, the power inside the cavity enhances 10-20 times, depending on the mirror reflectivities and absorption losses. The enhancement cavity length is thereby controlled and locked using the Hänsch-Couillaud stabilization technique (Hänsch and Couillaud, 1980). After second harmonic generation (Fig. 3.1, SHG), laser light with a wavelength of 366.5 nm, 2 MHz linewidth and a power of 400 mW is obtained (Fig. 3.1, dark blue line).

The UV beam is split by a high reflecting mirror (Fig. 3.1, M_1) in a way that 99 % of the beam is directed to the enhancement cavity where the scattering experiment is performed, whereas 1 % of the UV light leaking through the mirror is used as a reference beam (Fig. 3.1, green line), which itself is used to align the setup. The reference beam is spatially frequency filtered using lens L_1 and L_2 ($f = 10\,cm$) and pinhole P_1 ($d = 65\,\mu m$). Lens L_3 ($f = 20\,cm$) is used to focus the reference beam spatially in the same position as the main beam, which is the center of the scattering cell (Fig. 3.1, SC). The main beam is directed through the mode matching lens L_{EC} ($f = 40\,cm$) into the enhancement cavity, where the scattering cell is placed inside. The mode matching lens thereby ensures that the phase fronts of the laser beam match to the confocal cavity, which is held resonant by the Hänsch-Couillaud stabilization (HCS) technique (Fig. 3.1, HCS). The HCS utilizes changes in the polarization of the reflected light of the cavity to generate an error signal which can be used to lock and control the cavity length (Hänsch and Couillaud, 1980). The scattering cell is a 2.0 mm diameter and 52 mm long aluminum tube with Brewster angled input and output windows which prevent the amplification of the UV circulating power. The amplification reaches a factor of about 10, and hence a power level of 4 W

at 366.5 nm is achieved. The photo diode (Fig. 3.1, PD), used to measure the intensity of the light which is leaking through one of the confocal cavity mirrors, delivers a signal which is proportional to the laser light intensity inside the cavity.

The SRB-scattered light (Fig. 3.1, light blue line) is collected by lens L_4 at an angle of 90° from an auxiliary focus inside the scattering cell, after it is filtered by the diaphragm (Fig. 3.1, P_f) which covers an opening angle of 2°. The scattering angle is calculated to be $[90 \pm 0.6]°$ by means of geometrical relations using the sets of diaphragms and pinholes present in the optical setup. It is collimated and further geometrically filtered by lenses L_5 and L_6 and pinhole P_2 ($d = 50$ μm) to generate a geometrical shape of the beam of the scattered light which is accepted by the Fabry-Perot interferometer (Fig. 3.1, FPI). After that, the light is focused by lens L_{FP} (f = 50 mm) onto the flat mirror (Fig. 3.1, M_2) of the scanning FPI, which is used to resolve the frequency spectrum of the scattered light. The FPI is built as a hemispherical version of a confocal etalon, which means that it is composed of one spherical (Fig. 3.1, M_3) and one plane mirror (M_2) (Hernandez, 1986). To scan the FPI plate distance, the spherical mirror is mounted on a piezo-electrical translator (Fig. 3.1, PZT) which is controlled by a computer (Fig. 3.1, DAQ). Despite the lower light gathering in comparison to a plane parallel FPI (composed of two plane mirrors), the hemispherical configuration was chosen because of its insensitivity to small changes in tilt and orientation which can occur during scanning.

The light that passes through the FPI is detected using a photomultiplier tube (PMT, Philips-XP2020/Q) that is operated in photon-counting mode and read out by the DAQ.

To prevent contamination on the mirrors that could lead to absorption of UV light, the enhancement cavity, as well as the FPI is flushed with nitrogen.

To measure and monitor temperature, pressure and humidity of the gas under investigation several measurement devices are mounted in the system. The pressure is measured with two different baratrons, an active capacitive transmitter (Pfeiffer-CMR 271) for pressure values between 100 hPa and 1000 hPa, delivering an accuracy of 0.15 % of the measured pressure value, and an active piezo transmitter (Pfeiffer-APR 266) for pressure values between 1000 hPa and 11000 hPa, delivering an accuracy of 2 % for the full allowed measurement range. The temperature is measured with a thermo-resistor Pt100 delivering an accuracy of ± 0.5 K of the measured temperatures, and the humidity is measured with a monolithic integrated circuit with integral thermistor (Honeywell HIH-4602) delivering an accuracy of 3.5 % of the measured relative humidity value. For completeness, the main setup up parameters are summarized in Table 3.1.

Table 3.1: System parameters of the laboratory SRB experiment

Instrument	Parameter	Value
Laser	wavelength	366.5 nm
	power	400 mW/4 W
	operation mode	continuous wave
	line width	2 MHz
FPI	Γ_{FSR}	[7440 ± 40] MHz
	$\Delta \mathrm{f}_{\mathrm{FWHM}}$	[232 ± 10] MHz
Detector	photomultiplier	photon counting

3.2.2 The instrument function

The measured frequency spectrum is the convolution of the spectrum of the scattered light and the instrument function of the system. This means that an accurate knowledge of the instrument function is needed to derive the actual line shape of the scattered light. Therefore, a narrowband laser is used as light source, the instrument function of the system is mainly determined by the FPI which is used to resolve the frequency spectrum. The used interferometer in this setup is a piezo-scanning, hemispherical FPI (section 3.2.1). The characteristics of a hemispherical FPI are the same as those of a confocal FPI with double mirror separation, however, they are different to those of a plane parallel FPI with equal mirror reflectivities and plate separation (Hernandez, 1986). In particular, the free spectral range of the hemispherical FPI is one fourth of those of a plan parallel FPI with the same mirror reflectivities and separation.

The intensity transmission curve $\mathcal{A}(f)$ of an ideal FPI (axially parallel beam of rays, mirrors perfectly parallel to each other, mirrors of infinite size, mirrors without any defects) is expressed by the Airy function according to (Hernandez, 1986; Vaughan, 1989)

$$\mathcal{A}(f) = I_0 \left[1 + \left(\frac{2\,\Gamma_{\mathrm{FSR}}}{\pi\,\Delta \mathrm{f}_{\mathrm{FWHM}}} \right)^2 \sin^2 \left(\frac{\pi}{\Gamma_{\mathrm{FSR}}} f \right) \right]^{-1} \tag{3.1}$$

where I_0 is the intensity transmission maximum, Γ_{FSR} is the free spectral range, and $\Delta \mathrm{f}_{\mathrm{FWHM}}$ the full width at half maximum of the transmission curve. Γ_{FSR}, which is the spectral distance between two intensity maxima, depends on the velocity of light c, the mirror separation d, and the index of refraction n between the mirrors. For a hemispherical FPI, it is

$$\Gamma_{\mathrm{FSR}} = \frac{c}{8\,n\,d} \tag{3.2}$$

With $n \approx 1$ and $d = 5$ mm, the Γ_{FSR} of the hemispherical FPI is 7.5 GHz, and therefore, it is large enough to resolve the spectrum of molecular scattered light in the kinetic regime, whose FWHM is expected to be 3-4 GHz for a laser wavelength of 366 nm, pressure values between 300 hPa and 3000 hPa, and temperatures of about 300 K.

The exact Γ_{FSR} was measured to be [7440 ± 40] MHz. The Δf_{FWHM} was determined with Eq. 3.1 as [232 ± 10] MHz using a fit to the measured transmission curve (Fig. 3.2).

Throughout this chapter, $\mathcal{A}(f)$ is used to convolve it with the Tenti S6 model spectra before comparing it to the measurement data.

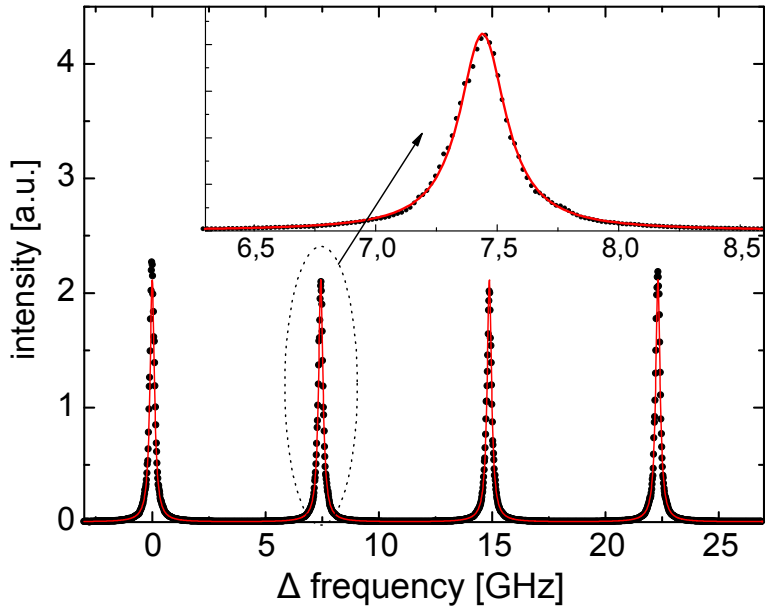

Figure 3.2: Transmission curve of the hemispherical Fabry-Perot interferometer (FPI) versus frequency, obtained with the narrowband reference laser and scanning the FPI plate separation (black dots), showing 3 complete free spectral ranges (Γ_{FSR}) and details of the instrument function (inset). The red line represents the best fit of Eq. 3.1 to the measurement leading to $\Gamma_{\mathrm{FSR}} = 7440$ MHz and $\Delta f_{\mathrm{FWHM}} = 232$ MHz.

As obvious from Fig. 3.2, the measured transmission curve of the FPI is very well described by the ideal Airy-function (3.1). Plate defects and others disturbances seem to have no remarkable influence on the transmission curve. This circumstance is different for the plane parallel FPI which is used for atmospheric measurements (chapter 4).

3.2.3 Investigation of stray light

In order to quantify precisely the line shape of SRB scattered light, it is necessary to make sure that the detected light is solely due to scattering on molecules, excluding any stray light which can originate from scattering at optics and particles within the setup.

To assure the absence of stray light within the detected signal, measurements with an evacuated scattering cell (Fig. 3.3, left) and a scattering cell filled with 1000 hPa of nitrogen (Fig. 3.3, right) were performed for three different cases (Fig. 3.3, symbols). Thereby, the scattered light was directly recorded with the PMT, without being filtered by the FPI.

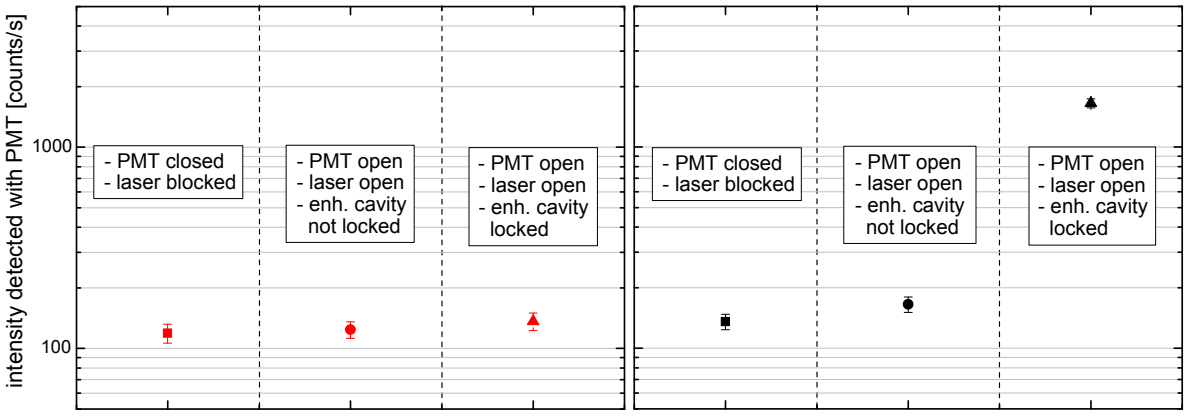

Figure 3.3: Average and standard deviation of the detected photomultiplier signal (counts/s, log-scale, measurement without using the FPI for filtering purpose) for three cases for investigating the existence of stray light in an evacuated scattering cell (left) and with a scattering cell filled with 1000 hPa of nitrogen (N_2) (right). The first case depicts the measured counts/s in case of a closed PMT, and therefore indicates the amount of dark counts. The second case shows the detected counts/s in case of an open PMT and an unlocked enhancement cavity. The third case shows the detected counts/s in case of a locked enhancement cavity and an open PMT.

The first case, gives the number of detected photons per second, when the PMT is optically closed (Fig. 3.3, squares). Therefore, this is the amount of dark counts which are caused by thermionic emission of the photo cathode. The measured dark counts are [119 $\pm$ 13] counts/s in case of the evacuated cell and [136 $\pm$ 12] counts/s in case of the N_2 filled cell. The slight difference in detected dark counts shows that there is a day to day variation in dark count detection of about 20 counts/s.

The second case gives the number of detected photons per second when the PMT is open, and the laser passes the scattering cell, but with an unlocked enhancement cavity (Fig. 3.3, triangles). Therefore, the laser power within the cell is about 400 mW instead of about 4 W in case when the enhancement cavity is locked. For both measurements, the one with the evacuated cell and the one with the nitrogen filled cell, a slight increase in detected photons is obvious. Whereas the amount of detected photons is [124 $\pm$ 12] counts/s in case of the evacuated cell, it is [165 $\pm$ 14] counts/s in case

of the cell filled with N_2. For the evacuated cell, the increase in the detected signal is therefore within the uncertainty of detected counts.

The third case shows the same situation as the second one, but with the enhancement cavity locked (Fig. 3.3, circles). It can clearly be seen that the detected signal is dramatically increased for the filled scattering cell ([1651 ± 86] counts/s), whereas it almost stays constant in case of the evacuated cell ([136 ± 11] counts/s). In case of the filled cell, the detected counts increase by a factor of 10 (from 165 counts/s to 1651 counts/s), which is due to the laser power amplification within the enhancement cavity.

In summary, although a lot of effort was made to optically cover the PMT from stray light, it can not totally be excluded to be present in the detected signal. The increase in detected photons in case of an evacuated cell and a locked enhancement cavity is 17 counts/s, which is still within the uncertainty of the detected counts, i.e, ± 13 counts/s in case of the evacuated cell. The signal strength for a common scattering experiment is in the order of 1500 counts/s (i.e., Fig. 3.3, right, triangle). This means that it can be assured that the contribution of stray light to the detected signal is not more than in the order of 1 %. Furthermore it should be noted that when the stray light is caused by fluorescence which is excited due to the UV light, it has a broad band spectral distribution. Therefore, the contribution to the detected signal will act more like a background signal which can be corrected within a calibration procedure (section 3.2.5). However, as the signal of possibly available stray light is only a few counts/s, it is too weak to be spectrally resolved using an interferometer.

3.2.4 Measurement procedure

Before performing a line shape measurement, the scattering cell was evacuated and purged with the working gas, before being charged to the desired pressure, to avoid any contamination from gases of previous measurements. The temperature for all measurements ranged between 295 K and 303 K. Pressures between 300 hPa and 3500 hPa were applied. The gas representative for air was a synthetic mixture of 79 vol. % N_2 and 21 vol. % O_2 without considering the 1 vol. % Ar or any other trace gases as CO_2, CH_4, which are present in atmospheric air.

To resolve the SRB spectrum of the scattered light, the FPI cavity length is changed by applying a voltage ramp to the PZT on which the curved FPI mirror is mounted. Additionally, the photons which are transmitted through the FPI are detected by a

PMT. To clarify the measurement procedure, the signal of the PMT, depending on the PZT scan voltage, is illustrated in Fig. 3.4 for an example of SRB scattered ultraviolet light (λ = 366.510 nm) in air (T = 298 K, P = 300 hPa). The components of the raw signal and their further processing are discussed as follows.

Before detecting the photons of the scattered light, the PMT is kept optically closed to determine its dark counts (section 3.2.3), which have to be subtracted from the detected signal to obtain the desired measurement data. The average of dark counts determined with this procedure is indicated by the red line in Fig. 3.4. It can be seen that the signal between each detected SRB spectrum reaches the dark count level, and therefore, it is assured that the different spectra do not overlap. The slight nonlinearity of the response of the PZT is responsible for a varying distance between the modes after scanning several FSR. This nonlinearity has to be corrected by calibration. Apart from the photon counter signal and the PZT scan voltage, a signal which is proportional to the intensity of the the laser inside the scattering cell is recorded (Fig. 3.4, bottom, black line) with a photo diode (Fig. 3.1, PD). This allows for corrections of the intensity of the scattered light for laser power long-term drifts.

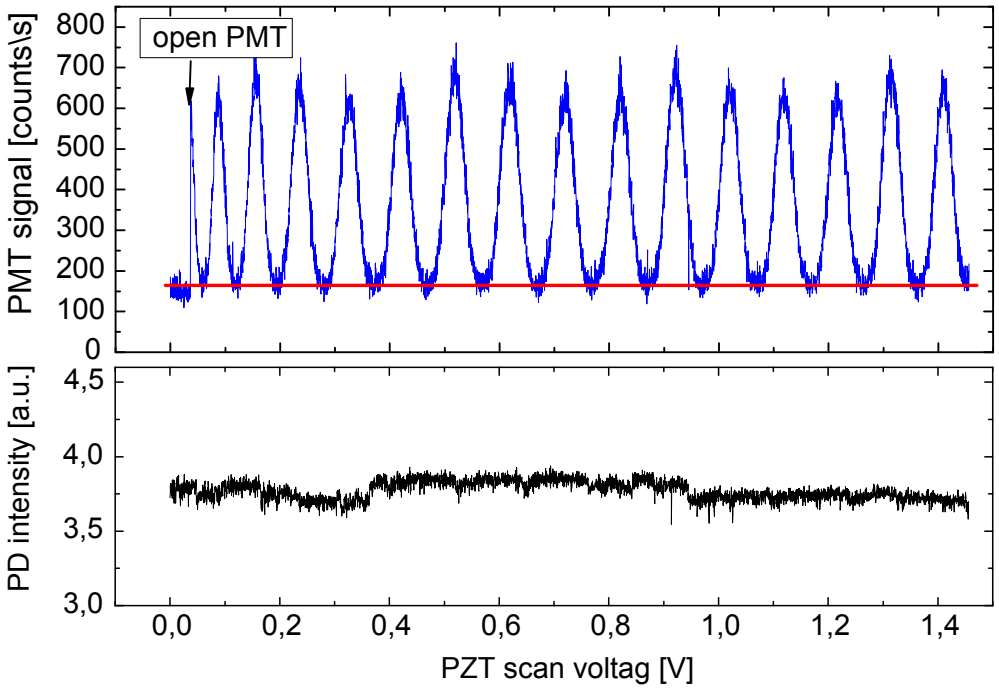

Figure 3.4: Top, blue line: Raw signal of the photomultiplier [counts/s] versus scan voltage, obtained in air (T = 298 K, P = 300 hPa). The average dark count level of the photomultiplier obtained before starting the measurement is indicated with a red line. Bottom, black line: Photo diode signal which is proportional to the laser intensity inside the enhancement cavity.

3.2.5 Frequency calibration and spectral averaging

The raw signal (Fig. 3.4) contains the intensity of the scattered light depending on the scan voltage which drives the piezo PZT of the FPI. This scan voltage has to be converted into a frequency, to obtain the spectral line shape which can additionally be compared to Tenti S6 model. For that purpose, the properties of the FPI which define the instrument function of the measurement device are used. The FSR of the FPI has been measured to be 7440 MHz, and therefore, the spectral distance between the peaks of the scattered light in the raw signal are also separated by 7440 MHz. Using this information, the piezo scan voltage can be converted into a relative frequency axis.

If this frequency calibration is done, the signal of several peaks - which are obtained by scanning the FPI - is averaged to get a better signal to noise ratio in the measured SRB line shape. This procedure is possible, as the peaks in the raw signal only differ slightly in intensity but provide the same width and line shape. Even at low pressures of 300 hPa, where the total scattering intensity is small due to the small amount of molecules within the scattering volume, a quantitative comparison to the Tenti S6 model is enabled due to the good signal to noise ratio of the averaged SRB line shapes. This circumstance is illustrated in Fig. 3.5, which shows the raw PMT signal of a single peak (left) and the averaged signal over 12 peaks (right).

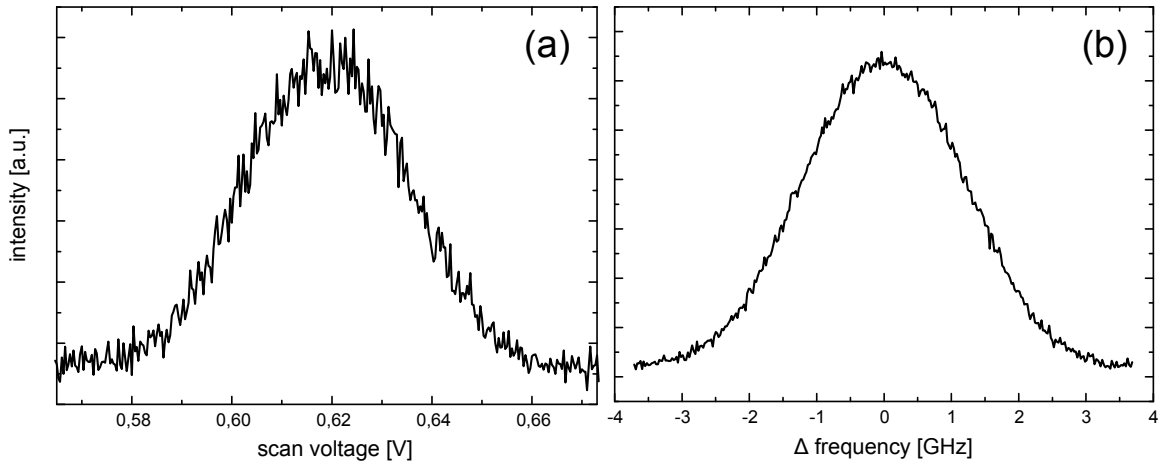

Figure 3.5: Measured SRB line shape of light scattered in air ($p = 300$ hPa, $T = 298$ K, $\lambda = 366.510$ nm, $\theta = 90°$). (a) Raw signal for one single peak, and (b) Line shape after averaging over 12 peaks.

3.2.6 Comparison of measurement data to the Tenti S6 model

The measured SRB line shape of the scattered radiation is the result of the convolution of the molecular spectral line shape and the instrument function, which itself is mainly determined by the transmission function $\mathcal{A}(f)$ of the FPI (section 3.2.2). Therefore, all modeled Tenti S6 line shapes are convolved with $\mathcal{A}(f)$ (Eq. 3.1) before being compared to the measured SRB line shapes (Fig. 3.6). The resulting modeled line shape after convolution is subsequently called $I_{\mathrm{m}}(f)$.

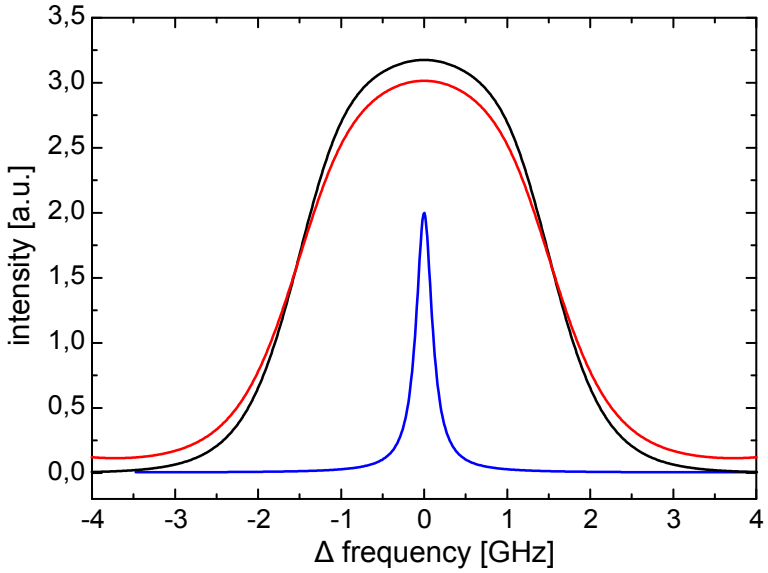

Figure 3.6: Simulated SRB line shape for air (T = 300 K, p = 1000 hPa, transport coefficients from Table A.1) using the Tenti S6 model (black line), the instrument function $\mathcal{A}(f)$ (Eq. 3.1, Γ_{FSR} = 7440 MHz, $\Delta\mathrm{f}_{\mathrm{FWHM}}$ = 232 MHz, blue line), and the convolution of both (red line).

As the light-scattering experiments do not provide an absolute intensity, it is necessary to normalize the experimental and the modeled spectra. Therefore, the integrated intensity of the spectra might be equal, the experimental spectra $I_{\mathrm{e}}(f)$ as well as the modeled spectra $I_{\mathrm{m}}(f)$ were normalized such that

$$\int_{-f_b}^{f_b} I(f)\,df = 1 \tag{3.3}$$

Ideally, the bounds f_b of the integration should be such that the intensity is zero at $f = f_b$, however, the FSR of the etalon is not much larger than the width of the measured spectra. Therefore, $f_b = f_{\Gamma_{\mathrm{FSR}}}/2$ is used in the normalization.

Furthermore, it is necessary to subtract the signal background I_{e_0} from the raw measured spectrum $I_{e_r}(f)$ before normalization of $I_e(f) = I_{e_r}(f) - I_{e_0}$. It turns out that I_{e_0} is not only the dark current of the photomultiplier. It also contains a small contribution I'_{e_0} of broadband fluorescence of the cell windows. Therefore, it was decided to correct the model spectra $I_m(f)$ for this poorly known background contribution, by setting $I_m(f) = a\, I_e(f) - I'_{e_0}$, and determining I'_{e_0} and the proportionality constant a in a least squares procedure for the wings of the spectra. If the measured spectra had the correct background, then the 2 constants would have the values $a = 1$ and $I'_{e_0} = 0$.

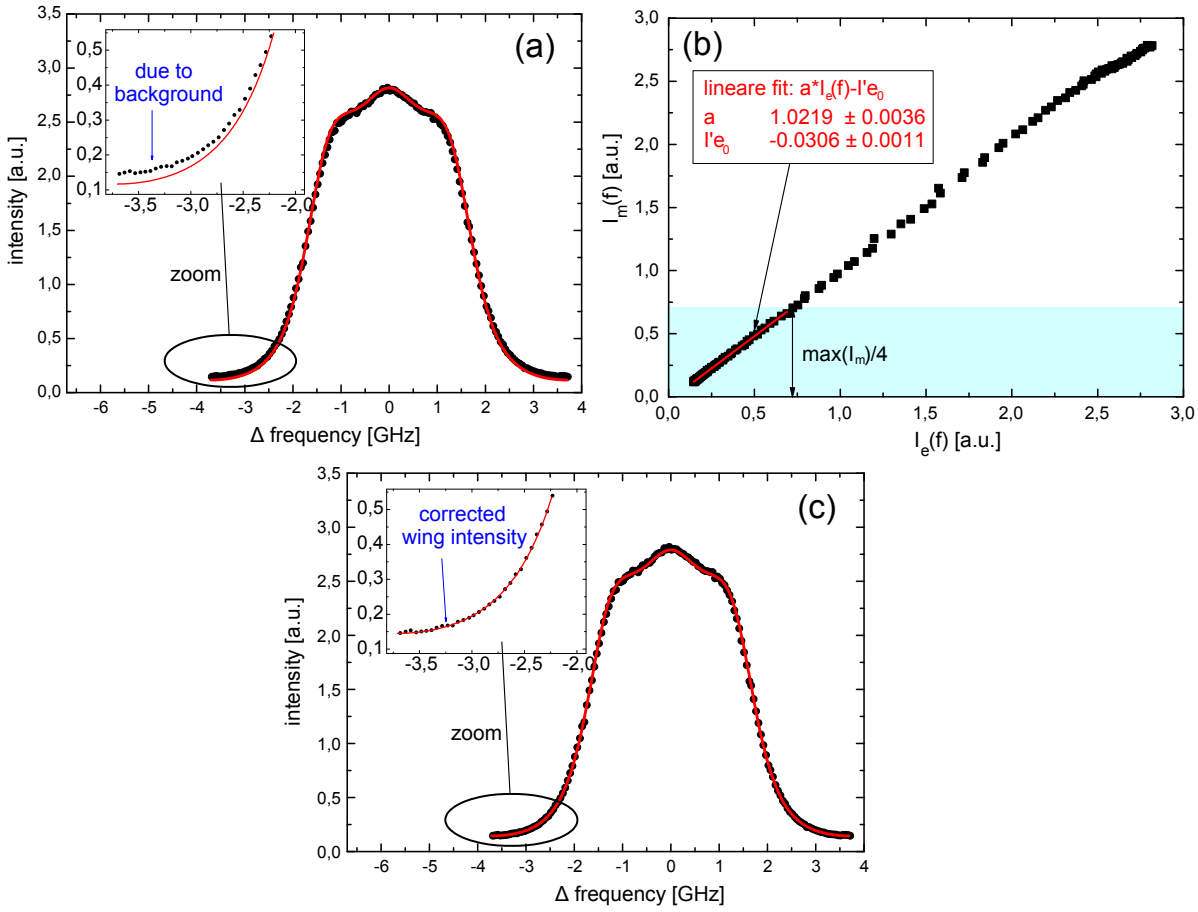

Figure 3.7: Principle of background correction caused by broadband fluorescence of the cell windows: Measured (black dots) and modeled (red line) SRB line shape in N_2 (p = 2000 hPa, T = 295.5 K) before (a) and after (c) background correction. Details of the wing intensity are depicted by the inset. The least squares procedure used to determine the background contribution I'_{e_0} and its proportionality constant a is shown in (b). Here, the intensity of modeled spectrum is plotted against the intensity of the measured spectrum. Intensities smaller than $\max(I_m)/4$, indicated by the light blue area, are used as input the linear fit. The resulting fit parameter are $a = 1.021 \pm 0.004$ and $I'_{e_0} = -0.031 \pm 0.001$.

The wings of the spectra were defined as frequencies such that $I_\mathrm{m}(f) \leq \max(I_\mathrm{m})/4$. The corrected model spectrum $I'_\mathrm{m}(f) = I_\mathrm{m}(f) + I'_{\mathrm{e}_0}$ was then normalized again such that $\int_{-f_b}^{f_b} I'_\mathrm{m}(f)\, df = 1$. This procedure gives a small but perceptible change of the background intensity; it increases the wing intensity $I_\mathrm{m}(f_{\Gamma_\mathrm{FSR}}/2)$ by approximately 25 %. In conclusion, in comparing experimental to model line shapes, both the offset and the scale of the vertical axis of the experimental result are chosen to match that of the model spectrum. The procedure of background correction is visualized in Fig. 3.7.

After background correction and normalization, the accordance between measured SRB line shapes and Tenti S6 model is quantified in several ways:

- By assuming Poisson statistics of the collected photon counts $\mathcal{N}$, it is possible to arrive at an estimate of the statistical error $\sigma_\mathcal{N}(f_i) = \sqrt{\mathcal{N}}$ at each (discrete) frequency f_i of the data. Thus, it is possible to define the normalized difference $\Delta I(f_i)$ between modeled spectrum $I_\mathrm{m}(f)$ and experimental spectrum $I_\mathrm{e}(f)$ according to

$$\Delta I(f_i) = \frac{I_\mathrm{m}(f_i) - I_\mathrm{e}(f_i)}{\sigma(f_i)} \tag{3.4}$$

  This is important as the number of photons collected for each spectrum varies and is typically smallest at the lowest pressures where the total scattering cross section is small due to the small amount of molecules within the scattering volume. If there is no systematic difference between model and measurements, then $\Delta I(f_i)$ would be constant and randomly varying around 1 over the entire frequency range.

- To determine the quality of the accordance between model line shape I_m and experimental line shape I_e, a χ^2 value is defined according to (Hoel et al., 1962)

$$\chi^2 = (1/N) \sum_{i=1}^{N} \left(\frac{I_\mathrm{m}(f_i) - I_\mathrm{e}(f_i)}{\sigma(f_i)} \right)^2 \tag{3.5}$$

  That is, if the computed line shape model I_m fits perfectly to the measured line shape I_e, only the statistical error σ remains in the numerator of Eq. 3.5. This case defines the minimum χ^2 value to be unity, and increasing χ^2 values can be thought of as corresponding to increasingly poor model agreement.

- The residual between measurement and model is plotted below each graph, and is calculated as a percentage deviation with respect to peak intensity of the modeled line shape $I_{\mathrm{m}}(f_{I_{max}})$ according to

$$\text{residual} = \frac{I_{\mathrm{m}}(f_i) - I_{\mathrm{e}}(f_i)}{I_{\mathrm{m}}(f_{I_{max}})} \cdot 100\,\% \tag{3.6}$$

Furthermore , the uncertainties of the experimental quantities (T, p, θ, section 3.2.1) are considered by calculating "worst-case" Tenti S6 line shapes for each comparison. Thereby, the worst case line shapes are defined by the minimal and maximal possible y parameter (y_{min} and y_{max}) according to

$$y_{\mathrm{min}} = \frac{(p - \Delta p)}{\sin(\frac{\theta+\Delta\theta}{2})\sqrt{T + \Delta T}} \cdot C \quad \text{and} \quad y_{\mathrm{max}} = \frac{(p + \Delta p)}{\sin(\frac{\theta-\Delta\theta}{2})\sqrt{T - \Delta T}} \cdot C\,, \tag{3.7}$$

where $C = \sqrt{M}/(2\,k_i\,\sqrt{2\,k_B}\,\eta)$ (all quantities defined with Eq. 2.14), and $\Delta T = \pm\,0.6$ K and $\Delta\theta = \pm\,0.6°$ are the uncertainties in temperature and scattering angle, respectively. The uncertainty in pressure is $\Delta p = \pm\,0.15\,\%$ for pressures between 0 hPa and 1000 hPa, and $\Delta p = \pm\,2\,\%$ for pressures between 1000 hPa and 10000 hPa. Thus, the measurement is compared not only to a single line shape, but to a line shape ensemble which is given by the uncertainties of the experimental quantities.

The uncertainty of the description of the instrument function ($\Gamma_{\mathrm{FSR}} = [7440 \pm 40]$ MHz and $\Delta \mathrm{f}_{\mathrm{FWHM}} = [232 \pm 10]$ MHz) is thereby indirectly considered by an additional temperature uncertainty of $\pm\,0.1$ K (uncertainty of the Pt100 is $\pm\,0.5$ K). By assuming a Gaussian SRB line shape with a FWHM $\Delta \mathrm{f}_{\mathrm{SRB}} = 3.75$ GHz (Eq. 2.16 and Eq. 2.17, $T = 295$ K, $\lambda = 366$ nm, $M_{\mathrm{air}} = 28.8$ g/mol) and an instrument function with a Gaussian line shape with FWHM $\Delta \mathrm{f}_{\mathrm{FPI}} = 0.23$ GHz, the FWHM $\Delta \mathrm{f}_{\mathrm{conv}}$ of the convolution of both can be calculated according $\Delta \mathrm{f}_{\mathrm{conv}} = ((\Delta \mathrm{f}_{\mathrm{SRB}})^2 + (\Delta \mathrm{f}_{\mathrm{FPI}})^2)^{(1/2)} = 3.76$ GHz. This enables the estimation of the influence of the instrument function uncertainty, compared to the influence of the temperature uncertainty. It can be shown that an additional temperature uncertainty of 0.1 K has the same influence on the SRB line shape as the uncertainty in FPI line width of 10 MHz. Therefore, the temperature uncertainty of $\pm\,0.6$ K, which is used for "worst-case" line shape calculation, already contains the uncertainty of instrument function quantities.

3.3 Discussion of experimental results

3.3.1 Determination of the bulk viscosity

In section 2.3.1 it was pointed out that the Tenti S6 model uses macroscopic gas transport parameter (shear viscosity, thermal conductivity, heat capacity, bulk viscosity) to parametrize the collision integral in the linearized WCU equation, in order to describe the spectral distribution of the molecular scattered light. However, as discussed in section 2.3.2, there is a serious shortage in bulk viscosity data for molecular gases, which is due to the error-prone indirect measurement technique used for bulk viscosity determination. Another problem is that the sound absorption measurements for bulk viscosity determination are performed at acoustic frequencies (up to 10^6 Hz), while light scattering involves frequencies which are three orders of magnitude larger. As the bulk viscosity is strongly frequency dependent (Graves and Argrow, 1999; Meador et al., 1996; Mountain, 1966), its value at frequencies in the order of GHz must be considered largely unknown.

In order to deal with this subject, a procedure which was already introduced by Pan et al. (2005, 2004a) was used to determine a value for the bulk viscosity η_b. At high pressures of $p = 3000$ hPa, the influence of Brillouin scattering on the spectrum is large, and therefore, its sensitivity to the used value of η_b in the S6 model is large (section 2.3.3). Thus, these pressures define a value of η_b at frequencies of about 1.3 GHz, where the S6 model fits the experiment best. By calculating the χ^2 value (Eq. 3.5) between measured and modeled SRB line shapes which are calculated for bulk viscosities of $1.0 \cdot 10^{-6}\,\mathrm{kg\,m^{-1}s^{-1}}$ to $1.0 \cdot 10^{-4}\,\mathrm{kg\,m^{-1}s^{-1}}$, a best fitting bulk viscosity can be obtained at the χ^2 minimum ($\chi^2{}_{\mathrm{min}}$).

It is worth mentioning that it is difficult to estimate the statistical uncertainty of the obtained bulk viscosity values. As described by Vieitez et al. (2010b), it is possible to estimate the statistical error in the determined bulk viscosity by using a maximum likelihood argument. Doing so, the statistical error is determined by the curvature at $\chi^2{}_{\mathrm{min}}$ and is in the order of 1 % within this experiment. However, there are errors which are assumed to play a much bigger role. First of all, the Tenti model is not the correct physical description of the Cabannes line of molecular scattered light, less than ever for light scattered in gas mixture like air (section 2.3.2). Therefore, it can not be assured that the Tenti model reflects the bulk viscosity physically correctly. However, it can be assured that the obtained bulk viscosity fits best for Tenti S6 model line shape calculations. Furthermore, the uncertainties in the experimental quantities (p, T, θ) have to be considered. This is done by using y_{min} and y_{max} from Eq. 3.7 for calculating "worst-

case" line shapes which are used for χ^2 calculation. Therefore, the bulk viscosities which are obtained at ${\chi^2}_{\min}$ of the "worst-case" line shapes define the maximum uncertainty of the obtained bulk viscosity.

The described procedure of bulk viscosity determination is demonstrated in Fig. 3.8, which shows the χ^2 depending on bulk viscosity for N_2 (a)-(c) and air (g)-(i) at different pressures. The corresponding measured (black dots) and the simulated SRB line shape ensembles (red area) are shown in (d)-(f) and (j)-(l), respectively. In case of N_2, two measurements (Fig. 3.8, (b) and (c)) were used to determine the bulk viscosity. The measurement at p = 3000 hPa yields $\eta_b = [2.25 \pm 0.53] \cdot 10^{-5}\,\mathrm{kg\,m^{-1}s^{-1}}$ and the one at p = 3500 hPa yields $\eta_b = [1.94 \pm 0.46] \cdot 10^{-5}\,\mathrm{kg\,m^{-1}s^{-1}}$. This results in a mean bulk viscosity for N_2 of $[2.10 \pm 0.70] \cdot 10^{-5}\,\mathrm{kg\,m^{-1}s^{-1}}$ (Fig. 3.8, (a)-(c), dark blue line (mean), light blue area (standard deviation)), which is from now on used for Tenti S6 model calculation. The obtained value is about a factor of 1.6 larger than the literature value of $1.29 \cdot 10^{-5}\,\mathrm{kg\,m^{-1}s^{-1}}$ obtained from sound absorption measurements (Emanuel, 1990; Pan et al., 2004b).

In case of air, two different measurements at p = 3000 hPa (exact measurement conditions can be found in Table A.3) were used for bulk viscosity determination (Fig. 3.8, (h) and (i)). They yield $\eta_b = [1.57 \pm 0.43] \cdot 10^{-5}\,\mathrm{kg\,m^{-1}s^{-1}}$ and $\eta_b = [1.22 \pm 0.35] \cdot 10^{-5}\,\mathrm{kg\,m^{-1}s^{-1}}$, and therefore, a mean bulk viscosity of $[1.40 \pm 0.55] \cdot 10^{-5}\,\mathrm{kg\,m^{-1}s^{-1}}$ (Fig. 3.8, (g)-(i)), dark blue line (mean), light blue area (standard deviation)), which is from now on used for Tenti S6 model calculation. The obtained value is about a factor of 1.3 larger than the literature value of $\eta_b = 1.1 \cdot 10^{-5}\,\mathrm{kg\,m^{-1}s^{-1}}$ (Rossing, 2007), which was obtained from sound absorption measurements (see also Fig. 2.5).

In summary, it can be said that SRB measurements offer an alternative measurement technique for the bulk viscosity of molecular gases. The uncertainty of the obtained bulk viscosity values is in the order of 35 %, and therefore, this measurement technique is not more accurate than utilizing sound absorption, however, it is performed for the correct sound frequencies in the GHz range. For N_2, a bulk viscosity of $\eta_b = [2.10 \pm 0.70] \cdot 10^{-5}\,\mathrm{kg\,m^{-1}s^{-1}}$ is obtained. This is a factor of 1.6 larger than the literature value of $1.29 \cdot 10^{-5}\,\mathrm{kg\,m^{-1}s^{-1}}$ (Emanuel, 1990; Pan et al., 2004b). For air, a bulk viscosity of $\eta_b = [1.40 \pm 0.55] \cdot 10^{-5}\,\mathrm{kg\,m^{-1}s^{-1}}$ is obtained. This is a factor of 1.3 larger than the literature value of $\eta_b = 1.1 \cdot 10^{-5}\,\mathrm{kg\,m^{-1}s^{-1}}$ (Rossing, 2007). This tendency is confirmed by Vieitez et al. (2010b) and Meijer et al. (2010), who obtained a bulk viscosity of $\eta_b = 2.2 \cdot 10^{-5}\,\mathrm{kg\,m^{-1}s^{-1}}$ and $\eta_b = 2.6 \cdot 10^{-5}\,\mathrm{kg\,m^{-1}s^{-1}}$ for N_2

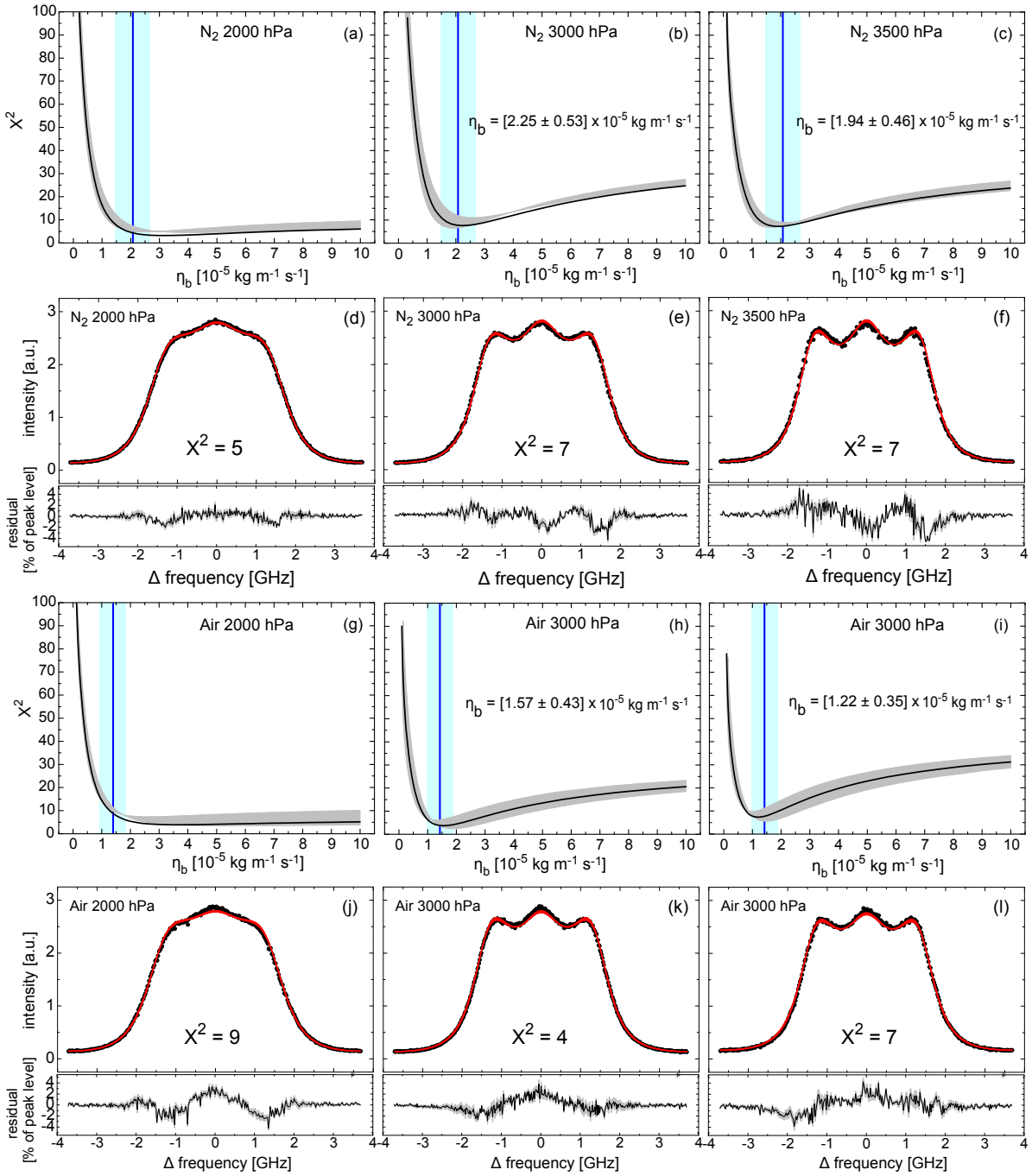

Figure 3.8: (a)-(c), (g)-(i): χ^2 error according to Eq. 3.5 as a function of bulk viscosity for N_2 and air at different pressures, respectively. The χ^2 for "worst-case" line shapes (Eq. 3.7) is indicated with the gray area and is used to calculate the standard deviation of the obtained bulk viscosity values. The obtained mean bulk viscosity values are indicated by the dark blue line (mean) and the light blue area (standard deviation), respectively. (d)-(f), (j)-(l): Measured (black dots) and simulated (red area) SRB line shapes in N_2 and air at different pressures, used for χ^2 calculation. Thereby the red line indicates the area between the two worst-case line shapes (Eq. 3.7). Below: Residual between line shapes as a percentage deviation with respect to peak intensity. Exact measurement conditions can be found in Table A.3, all transport coefficients used for line shape simulation can be found in Table A.1.

and $\eta_b = 2.0 \cdot 10^{-5}\,\mathrm{kg\,m^{-1}s^{-1}}$ for air by using the presented procedure within coherent Rayleigh-Brillouin scattering measurements at a different scattering angle ($\theta = 178°$) and wavelength ($\lambda = 532$ nm). Therefore, the presented bulk viscosity values seem to be solid.

However, Pan et al. (2004a) showed a good agreement between measured CRB line shapes in N_2 and their line shape model by using the literature bulk viscosity of $1.29 \cdot 10^{-5}\,\mathrm{kg\,m^{-1}s^{-1}}$. This discrepancy might be ascribed by the fact that they used their 7 moment model instead of the 6 moment model which was used by Vieitez et al. (2010b) and Meijer et al. (2010).

3.3.2 Rayleigh-Brillouin spectra measured in N_2 and air

A key point within the framework of this thesis was the question of how well the Tenti S6 model reproduces the line shape in nitrogen and air, and whether the line shape of spontaneous Rayleigh-Brillouin scattering in air can be modeled by using the transport coefficients of nitrogen as common in atmospheric applications (Liu et al., 2009a; Shimizu et al., 1983; Young and Kattawar, 1983). Therefore, SRB measurements on N_2 and air at pressure ranges from 300 hPa to 3500 hPa and temperatures of 295.5 K to 300 K were performed and compared to the Tenti S6 model. The detailed measurement conditions can be found in Table A.3.

Measured SRB spectra for N_2 and air at pressures of 2000 hPa, 3000 hPa, and 3500 hPa, the comparison to the Tenti S6 model, and the residuals with respect to peak intensity were already shown in Fig. 3.8 (d) to (f), and (j) to (l), as they were used for bulk viscosity determination (section 3.3.1). From these figures it is obvious that significant differences between model and measurement exist. For N_2, minimum χ^2 values of $\chi^2 = 5$ at 2000 hPa, and $\chi^2 = 7$ at 3000 hPa and 3500 hPa are obtained. For air, the obtained minimum χ^2 values are $\chi^2 = 9$ at 2000 hPa, $\chi^2 = 4$ and $\chi^2 = 7$ at 3000 hPa. However, as obvious with the residual plots below each graph, these differences are small on a relative scale; in particular the deviations between model and measurement are smaller than 4 % of the peak intensity in all cases.

To clarify further the difference of SRB spectra obtained in pure N_2 and air and to show the ability of predicting this difference using the Tenti S6 model, the residual plots between both spectra (N_2 and air) obtained at almost the same measurement conditions (Table A.3) are calculated.

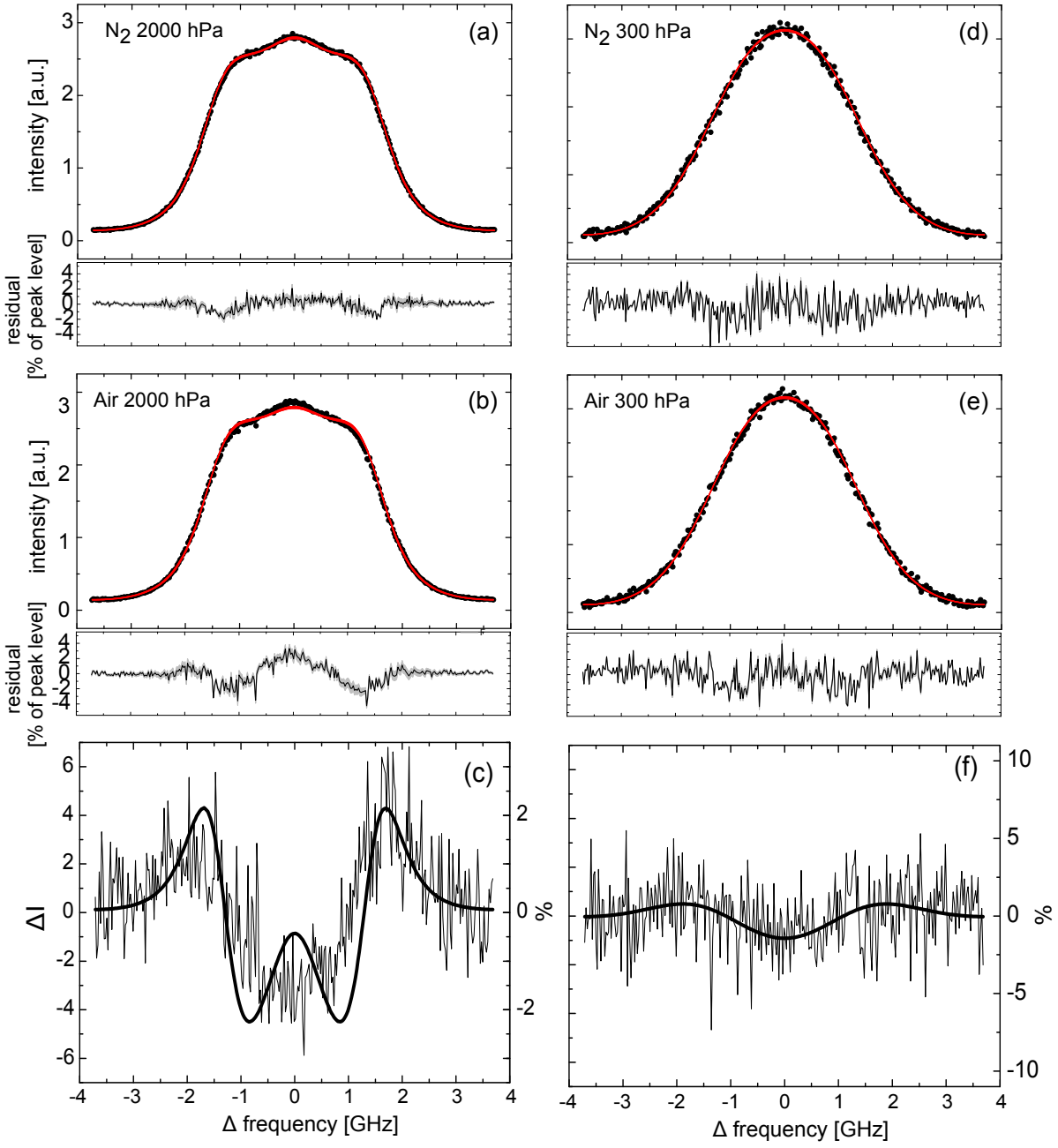

Figure 3.9: Measured SRB line shapes (black dots) in N_2 at 2000 hPa (a) and 300 hPa (d) and air at 2000 hPa (b) and 300 hPa (e) compared with the Tenti S6 model (red line). (c) and (f) indicate the difference between both spectra (N_2 and air) according to Eq. 3.8 for 300 hPa and 2000 hPa, respectively. Thereby, the thin black line indicates the difference between the measured and the thick black line between the modeled spectra, respectively. The right vertical axes give the deviation with respect to peak intensity in percentages.

Thereby, the difference between the N_2 and air spectra is quantified in two ways. First the statistical significance of this difference is illustrated by plotting the normalized frequency-dependent difference

$$\Delta I(f_i) = \frac{I_{N_2}(f_i) - I_{air}(f_i)}{(\sigma_{N_2}(f_i)^2 + \sigma_{air}(f_i)^2)^{1/2}}, \tag{3.8}$$

where σ_{N_2} and σ_{air} are the statistical errors of the measured N_2 and air spectra assuming Poisson statistics, respectively, and second, the difference is presented as a percentage deviation by comparing it to the intensity at Δfrequency = 0 Hz.

The measured as well as the modeled difference for a 300 hPa (c) and a 2000 hPa measurement (f), as well as the corresponding SRB line shapes which were used for the calculation (a), (b) and (c), (d) are plotted in Fig. 3.9.

It is apparent from Fig. 3.9 that the spectrum in N_2 differs significantly from that in air down to 300 hPa. The difference is about $\pm 2\,\%$ of peak level for both measurements. The difference between N_2 and air spectra can be reproduced well by the Tenti S6 model when taking the corresponding transport coefficients (Table A.1). From the gas transport properties that determine the line shape, the molecular mass sets its overall width via the Doppler broadening. The other transport coefficients (shear viscosity, bulk viscosity and thermal conductivity) have a smaller influence on the line shape. Taking a fictitious gas with the mean molecular mass of air and N_2 transport coefficients (not shown here), as done by Liu et al. (2009a), produces a line shape at p = 3000 hPa which is indistinguishable from that using all air transport coefficients according to Table A.1.

3.3.3 Rayleigh-Brillouin spectra measured in air at atmospheric conditions

As mentioned in chapter 1, an accurate knowledge of the SRB line shape is required for several atmospheric lidar applications (Dabas et al., 2008; Elliott et al., 2001; Fiocco and DeWolf, 1968; Liu et al., 2009a,b; Reitebuch et al., 2009; Seasholtz et al., 1997; Shimizu et al., 1986). It is common that the Tenti S6 model with N_2 gas parameters (Liu et al., 2009a; Rye, 1998; Young and Kattawar, 1983), or even the Gaussian approximation from the Knudsen regime (Ansmann et al., 2007; Hua et al., 2005; McGill et al., 1997a; Paffrath et al., 2009) is used for this purpose. In section 3.3.2 it was already pointed out that the difference in line shape between air and pure nitrogen is obvious, and that this difference can be described by the Tenti S6 model. Thereby, the main spectral difference is caused by the different molecular masses of N_2 and air.

Furthermore, it is now verified that the Gaussian approximation is not a satisfactory description of SRB line shapes, not even for atmospheric pressures down to 300 hPa, which corresponds to an altitude of about 10 km above sea level.

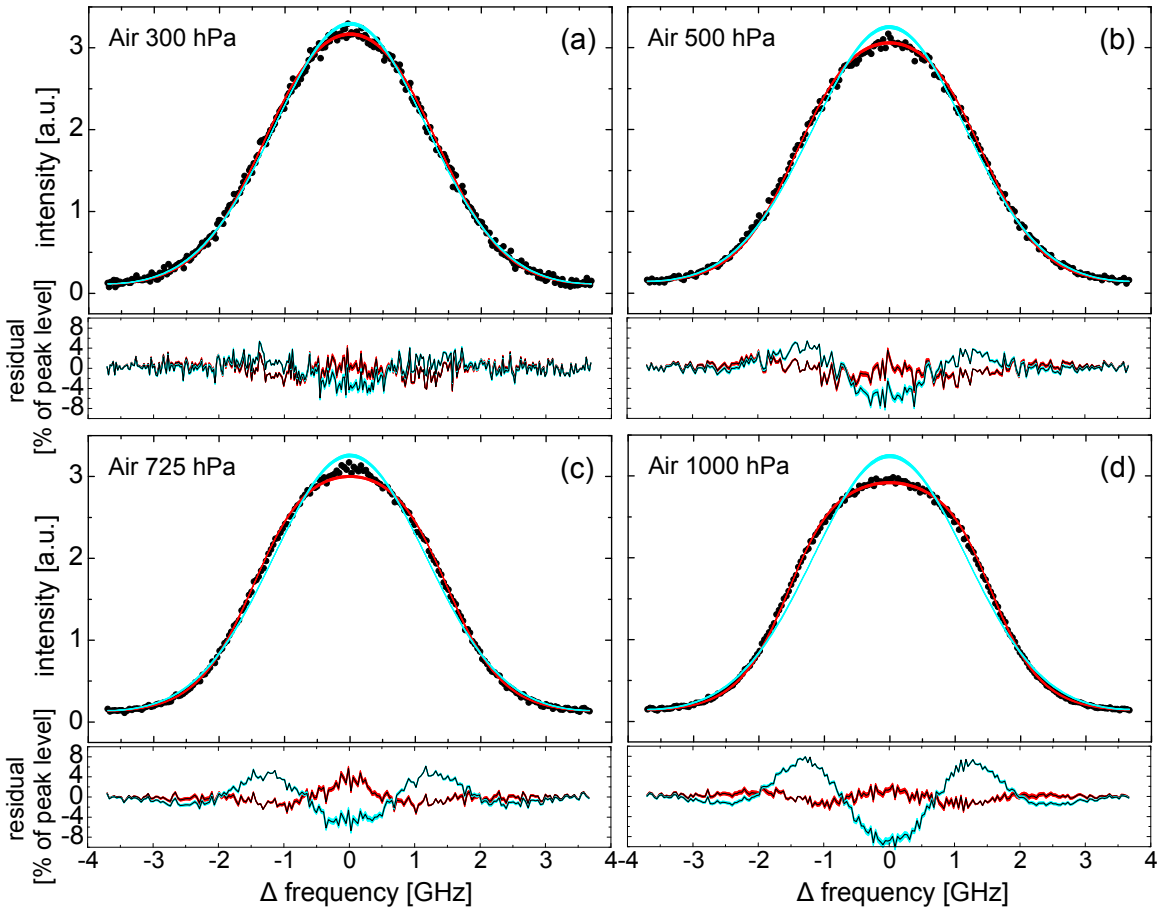

Figure 3.10: Measured spontaneous Rayleigh-Brillouin spectra in air (black dots), compared to the Tenti S6 model (red line) and the Gaussian function (Eq. 2.17) (blue line) at pressures of $p = 300$ hPa (a), 500 hPa (b), 725 hPa (c) and 1000 hPa (d). The difference between measurement and model (red line) and measurement and Gaussian function (blue line) as a percentage deviation compared to the intensity at $\Delta f = 0$ Hz is depicted below each graph. For the Tenti S6 model calculation, the normalized differences between measurement and model are $\chi^2 = 2.0$ (a), 2.5 (b) 3.9 (c) and 3.7 (d). For the Gaussian function, these differences become $\chi^2 = 2.6$ (a), 7.6 (b), 7.9 (c) and 50 (d).

Figure 3.10 shows SRB line shapes measured in air at 300 hPa (a), 500 hPa (b), 725 hPa (c) and 1000 hPa (d) and the comparison to both the Tenti S6 model and the Gaussian line shape resulting from the Maxwell velocity distribution according to Eq. 2.17 (approximation of the SRB line shape for an ideal gas in thermal equilibrium). Below each graph, the difference between model and measurement as a percentage deviation compared to the intensity at Δfrequency $= 0$ Hz is shown.

The deviation between S6 model and measurement is about ± 2 % for the measurements at 300 hPa, 500 hPa, and 1000 hPa. In the case of the 725 hPa measurement, the deviation is about ± 4 % around the peak of the laser. This deviation seems to come from stray light which is caused by a slightly misaligned laser beam, as it occurs at the emitted laser frequency. If the laser beam is not totally centered within the scattering cell, it can hit the cell wall, and as a result, this scattered light could partly enter the FPI.

On the contrary, the deviation between measurement and Gaussian approximation is about ± 9 % for an ambient pressure of 1000 hPa (≈ sea level), and still about ± 3 % for an ambient pressure of 300 hPa (≈ 10 km above sea level). This clearly demonstrates that the Gaussian approximation is inadequate at pressures of 500 hPa to 1000 hPa, while it is still significantly different from the Tenti S6 model at p = 300 hPa.

3.3.4 Influence of water vapor to the Rayleigh-Brillouin line shape

In section 2.3.2 it was pointed out that humidity has a large effect on the bulk viscosity at acoustical frequencies. In section 2.3.3 it was additionally mentioned that the bulk viscosity has a remarkable influence on the SRB line shape. Thus, humidity may also have an effect on scattering line shapes, which correspond to much larger sound frequencies (∼ GHz). Therefore, SRB spectra obtained in dry and water vapor saturated air were compared to each other, to investigate if there is any change in line shape due to humidity. The relative humidity content was measured to 99.4–99.9 % for the case of water vapor saturated air. The temperature was [299.4 ± 0.5] K in case of dry air and [301 ± 0.5] K in case of humid air. The ambient pressure was [1040 ± 15] hPa in both cases. This corresponds to a volume fraction of water vapor of 3.6 %. The results of these experiments are illustrated in Fig. 3.11.

Both spectra are modeled well by the Tenti S6 model, using the transport coefficients of dry air in both cases, while a plot of the normalized difference (Eq. 3.8) in Fig. 3.11 (c) does not show a significant difference. Although all transport coefficients are the same when taken at the same reference temperature, the model spectra are slightly different due to the slightly different temperatures of the two experiments. These results show that at GHz frequencies, water molecules do not significantly affect the bulk viscosity, at least not for a water vapor content up to 3.6 vol. %, which is almost the upper bound within the atmosphere.

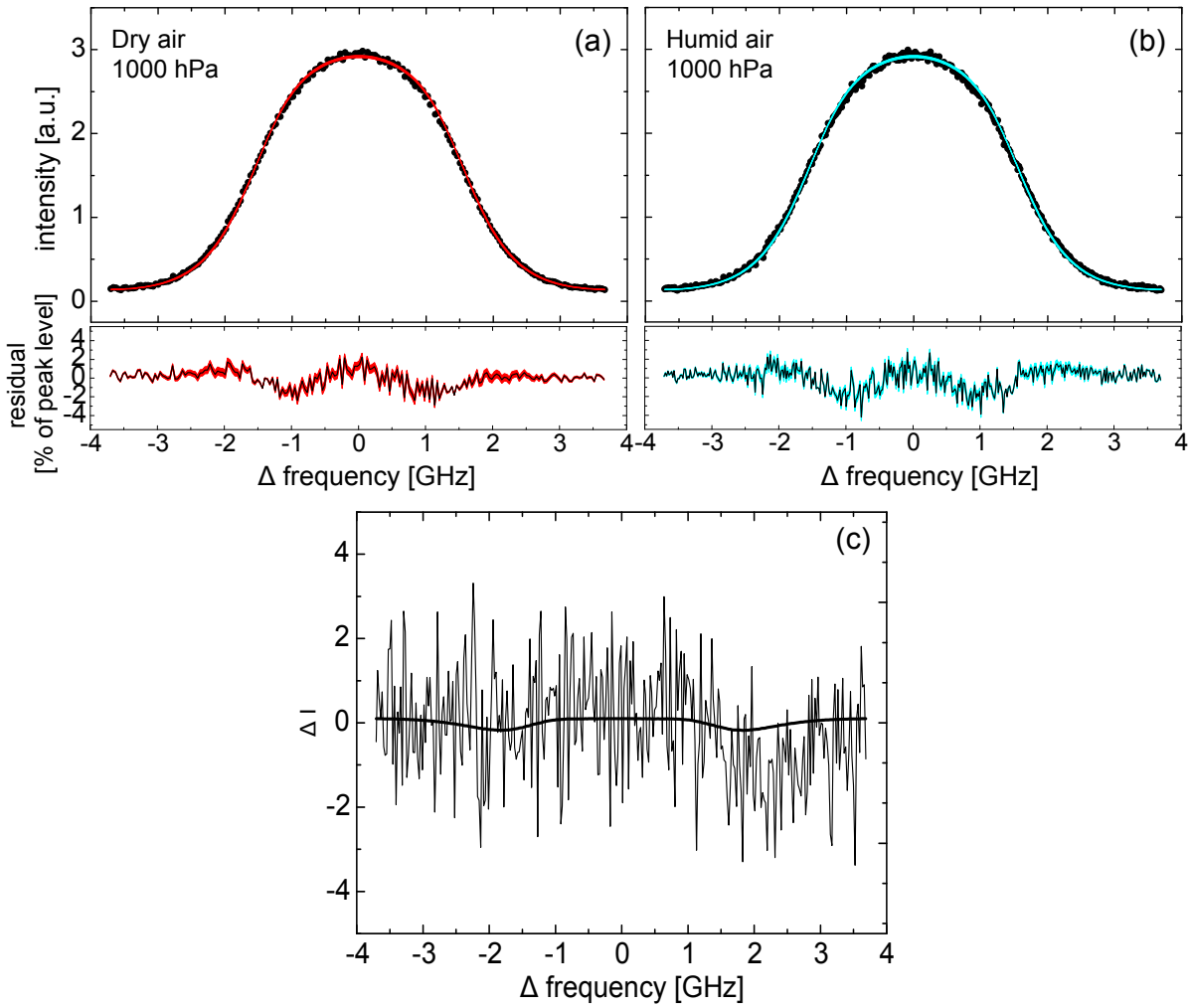

Figure 3.11: (a) Measured SRB line shape of dry air (black dots) compared to the Tenti S6 model (red line) ($T = 299.4$ K, $p = 1040$ hPa, $\theta = 90°$). The difference between model and data is expressed by $\chi^2 = 3.1$. (b) Measured SRB line shape of water saturated air (black dots) compared to the Tenti S6 model (blue line) ($T = 301.0$ K, $p = 1040$ hPa, $\theta = 90°$). The difference between model and data is expressed by $\chi^2 = 2.7$. The difference between model and measurement as a percentage deviation compared to the intensity at $\Delta f = 0$ Hz is shown below each graph, respectively. (c) Normalized difference ΔI (calculated according to Eq. 3.8) between measured spectra of (a) and (b) (thin black line) with the mean squared difference $\chi^2 = 1.7$. The normalized difference ΔI between the modeled spectra is indicated by the thick black line.

3.4 Summary

Spontaneous Rayleigh-Brillouin scattering was measured at a wavelength of 366.5 nm and a scattering angle of 90°. The measurements were performed for N_2, dry and humid air with temperatures of 295 to 301 K and pressures of 300 to 3500 hPa. For the first time, the SRB line shapes of N_2 and air in the kinetic regime were compared to the Tenti S6 model. The bulk viscosity for frequencies in the order of GHz of N_2 and air was determined using SRB measurements at the largest pressure (3000 hPa and 3500 hPa) in combination with the S6 model (section 3.3.1). It was demonstrated that the line shapes obtained in N_2 and air under the same measurement conditions differ significantly at pressures of 2000 hPa and 300 hPa (section 3.3.2), and that this difference is mainly caused by the mass difference between N_2 and air. In addition, it was pointed out that the Gaussian approximation is not a satisfactory description for SRB line shapes obtained in air with atmospheric pressures down to 300 hPa (section 3.3.3). It was further shown that the line shapes of N_2 and air can be described by the Tenti S6 model, with small but measurable discrepancies at atmospheric and higher pressures. On a relative scale these deviations are smaller than $\pm$ 4 % with respect to the peak intensity for all cases. For atmospheric relevant pressures, the deviations are even smaller than $\pm$ 2 %. By considering a contribution to the measured SRB line shapes due to undetected stray light and due to the Q-branch of rotational Raman scattering, and by considering the slight asymmetry in the measured SRB line shapes, these deviations can be view to be within the measurement uncertainty.

It was furthermore pointed out that humidity has no significant influence on the line shape of the scattered light, not even for high water vapor contents up to 3.6 vol. % in the atmosphere (section 3.3.4).

It was verified that the Tenti S6 model, which refers to a single-species molecular gas, can be applied to air by using the effective transport coefficients of air, and the molecular mass of a fictive gas mixture of N_2 and O_2. However, this approach is not based on the microscopically correct description of the collision between two different molecules. The Tenti S6 model is a kinetic model which involves collisions between molecules expressed in a single collision integral. Air contains different molecules with different collision cross sections. A better line shape model, therefore, should explicitly involve those details. For gases consisting of hard spheres atoms, such a model has recently been designed, and has shown to provide a better fit to spectra of noble gas mixtures than a hydrodynamic model (Bonatto and Marques, 2005). However, hard-sphere models consider no internal

degrees of freedom, and thus, they can not be used for the description of molecular gases like N_2 or air.

Although the insignificance of water for SRB line shapes has been established, the influence of other trace gases such as CO_2 and CH_4, and Ar of the real atmosphere remains to be investigated. Furthermore, there is a need to investigate the temperature dependence of gas transport coefficients and its influence on the SRB line shapes for atmospheric applications.

To deal with the still open issues, and to additionally verify the laboratory results of SRBS on air in the real atmosphere, a field campaign called BRAINS (BRillouin scattering - Atmospheric INvestigation on Schneefernerhaus) was performed. The accomplishment and the results of the BRAINS campaign are discussed in the next chapter.

Chapter 4

Investigation of spontaneous Rayleigh Brillouin scattering in the atmosphere

The laboratory experiments on spontaneous Rayleigh-Brillouin (SRB) scattering discussed in chapter 3 laid the groundwork for an accurate description of the SRB line shape in air using the Tenti S6 model. To verify if the obtained laboratory results are also valid for a line shape description in the real atmosphere under more complex and variable conditions, a field campaign called BRAINS (Brillouin scattering - atmospheric investigation on Schneefernerhaus) was performed from the environmental research station Schneefernerhaus. The performance and the results of the BRAINS campaign are discussed in the following.

4.1 Introduction

More than 40 years ago, Fiocco and DeWolf (1968) referred to the necessity of considering Brillouin scattering when deriving the frequency spectrum of scattered laser light in the atmosphere. However, because of the partly uncontrolled, non-ideal and challenging measurement conditions, the effect of Brillouin scattering has not been successfully demonstrated within the atmosphere yet. Nevertheless, and despite the high requirements in their performance, atmospheric SRBS experiments are useful as they offer remarkable advantages compared to laboratory experiments. For instance, atmospheric measurements provide the unique[1] opportunity to investigate SRBS in backscatter geometry (scattering angle of 180°). Furthermore, as the temperature in the lower

[1] In laboratory SRBS experiments, scattering from optics and windows can not be avoided totally. Thus, a signal which is detected in backward direction will not only contain the fraction of light scattered on molecules, but also a fraction of light scattered on optics used in the laboratory setup.

atmosphere (0 - 12 km above sea level) varies from about 210 K to 300 K, atmospheric measurements can be used to investigate the influence of the temperature dependence of gas transport parameters on the SRB line shape. In addition, measurements in the atmosphere provide information about the influence of the noble and trace gases in air (e.g. argon and carbon dioxide) on the SRB line shape. It was already mentioned in section 2.3.2 that water vapor in air might have an influence on the SRB line shape. It is still questionable if similar effects can occur for other gases in the atmosphere, too.

The only (to the author's knowledge) attempt to investigate SRBS in the atmosphere was performed within the framework of the ILIAD (Impact of line shape on Aeolus-ADM Doppler estimates) study (Flamant et al., 2005), initiated by ESA. Within this study, data sets of four different lidar systems have been analyzed by D. Rees et al. (Hovemere Ltd.). They pointed out that the data of two lidar systems could not be used for SRB investigations because of limited information of atmospheric state and strong "contamination" due to Mie scattering on aerosols. The data of a third lidar was not analyzed in detail, and thus, only the data from the Doppler wind and temperature lidar system of the ALOMAR (Arctic lidar observatory for middle atmosphere research) observatory, located in Andøya in the north of Norway, was used for investigating the effect of Brillouin scattering in the atmosphere. Unfortunately, this data was only analyzed for altitudes above 12 km where the effect of Brillouin scattering is small[2]. It was demonstrated that the measured SRB spectra at different altitudes (12 km, 14 km and 20 km above sea level) differ to a defined reference spectrum at 18 km. However, this measured difference is about a factor of 2 - 3 higher compared to deviations simulated by using the Tenti S6 model. Such high deviations seem to be unrealistic compared to existing laboratory studies. The authors of the ILIAD study concluded themselves: "*Experimental Lidar works have been conducted and data analysis performed (using new and old databases) showing that the Rayleigh-Brillouin effect could be there, but the data set is too small to claim for an evidence of Brillouin doublet and possible discrepancy with Tenti's S6. The reported factor 2 off in the mid troposphere seems too large when compared to existing laboratory validation*" (Flamant et al. (2005), chapter 8, page 123). This recent statement provides further evidence of the challenge in verifying the Brillouin effect in the atmosphere.

[2]The ambient pressure at 12 km above sea level is about 200 hPa. And although it was shown in section 3.3.3 that the Brillouin effect in air is obvious down to a pressure of 300 hPa, the difference to a Gaussian function due to pure Rayleigh scattering is small and assumed to be hardly measurable within the atmosphere.

For proving the Brillouin effect in the atmosphere, the following essential issues have to be considered: The deviation of the Rayleigh-Brillouin line shape to a Gaussian function due to "pure" Rayleigh scattering is proportional to the y parameter (Eq. 2.14 in section 2.1.3), which increases for increasing pressure values. Thus, low altitudes with large ambient pressures are generally preferred for performing SRBS experiments in the atmosphere. However, the large aerosol content in the atmospheric boundary layer limits the usefulness of low altitudes. Light scattering from aerosols is stronger than scattering from molecules and its spectral line width is much smaller than from molecular scattering. Thus, scattering from aerosols must be avoided in order to not disturb the measured SRB line shape. This means that an adequate location for investigating SRBS in the atmosphere is just above the atmospheric boundary layer (still high ambient pressure but already low aerosol content). Additionally, a laboratory infrastructure which enables scientific lidar measurements is needed. As pointed out in section 4.2.1, all these circumstances are fulfilled by the environmental research station Schneefernerhaus.

In addition to a well-chosen measurement location, a suitable lidar system has to be used for atmospheric SRBS experiments. A lidar system which is well adapted for that purpose is the ALADIN (Atmospheric LAser Doppler Instrument) airborne demonstrator A2D. The A2D is a direct-detection Doppler wind lidar (DWL) which was developed by the European Aeronautic Defence and Space Company (EADS-Astrium) and Deutsches Zentrum für Luft- und Raumfahrt (DLR). The main task of the A2D is to validate the ALADIN Doppler lidar, which is the instrument on the ADM-Aeolus space mission of ESA.

In the framework of this thesis, the field campaign BRAINS was performed in January - February 2009, aiming to demonstrate the effect of Brillouin scattering in the atmosphere. To reach this goal, the A2D system was used to perform horizontal lidar measurements from the environmental research station Schneefernerhaus. An overview of the experimental details, the measurement procedure and a discussion of the obtained results is given in the following.

4.2 Experimental details

4.2.1 The environmental research station Schneefernerhaus

The environmental research station Schneefernerhaus is located at the south-facing slope of Germany's highest mountain - the Zugspitze (2962 m), situated at an altitude of 2650 m above sea level. It was originally built in 1930's as a hotel for ski tourism, but due to the high upkeeps and the avalanche-prone location the hotel was closed in the end of the 1980's. To avoid the complex and expensive pulling down of the building, it was reconstructed into Germany's highest research station - the Umweltforschungsstation Schneefernerhaus (UFS)[3]. A photograph of the Schneefernerhaus is illustrated in Fig. 4.1.

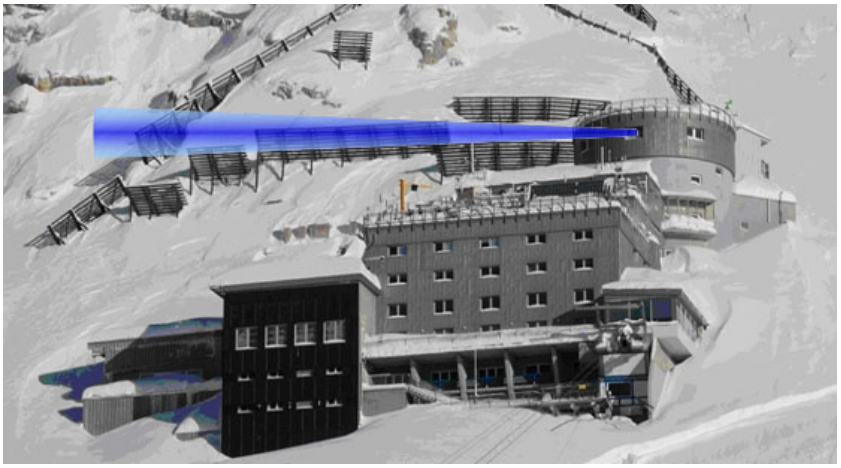

Figure 4.1: Photograph of the environmental research station Schneefernerhaus (2650 m), located at the south-facing slope of Germany's highest mountain - the Zugspitze (2962 m), taken during the BRAINS campaign in February 2009. The SRBS experiments were performed from the laboratory at the top of the UFS. The blue line indicates the outgoing laser beam.

The UFS provides perfect conditions for the first-time verification of the Brillouin effect within the atmosphere. During high-pressure weather conditions in winter, the altitude of the UFS is usually higher than the atmospheric boundary layer[4] and therefore, SRBS measurements are not disturbed by scattered light from aerosols. Nevertheless, the ambient pressure of about 720 hPa, which was observed during the BRAINS campaign

[3]The reconstruction was enabled with financial assistance from the state of Bavaria, the federal ministry of education and research, and the Deutschen Bundesstiftung Umwelt.

[4]Data of the federal environmental agency (UBA) show that the annual mean particle density at the UFS is 1000 particles/cm^3 and during winter even less than 500 particles/cm^3. This value has to be compared to a particle density of up to 60000 particles/cm^3 in cities (personal communication Dr. Ries, UBA).

period in January-February 2009, is large enough to have a remarkable influence due to Brillouin scattering. Furthermore, despite its extraordinary location, the UFS offers a very good laboratory infrastructure. Sufficient power current connection as well as water supply is permanently provided, and bulky equipment can be delivered by using a cog railway. In addition, a number of in-situ measurement data of temperature, pressure, humidity and aerosol content, performed by the German weather service (Deutscher Wetterdienst, DWD) and the federal environmental agency (Umweltbundesamt, UBA), is available and can be used for data analysis. Moreover, data from radiosondes, daily launched from the airport Innsbruck ($\approx$ 30 km from the UFS) are available. Another advantage is, that the UFS allows the performance of horizontal lidar measurements over long distances. This kind of measurement is favorable as the data of horizontal lidar measurements can be averaged over several kilometers, which leads to an improvement of the signal to noise ratio in the measured SRB line shapes. All in all it can be concluded that the environmental research station Schneefernerhaus provides well-suited conditions for the performance of SRBS experiments in the atmosphere.

4.2.2 The A2D Doppler Wind Lidar

The lidar system, used for the atmospheric SRBS experiments is the direct detection Doppler wind lidar A2D, developed to validate the wind lidar ALADIN, which is the instrument on the ADM-Aeolus mission of ESA (European Space Agency, 2008). As discussed in the following, the A2D instrument is well-suited for the investigation of Brillouin scattering in the atmosphere. The basic principle of the A2D is depicted in Fig. 4.2.

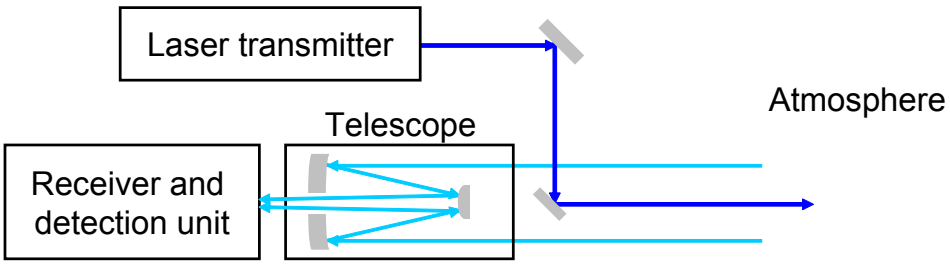

Figure 4.2: Basic principle of the A2D lidar system. Short laser light pulses (dark blue) are transmitted into the atmosphere, where they are scattered on molecules, aerosols, and cloud particles. A telescope collects the backscattered light (light blue), which is spectrally resolved and detected in an optical receiver. The laser transmitter and the receiver are sketched in more detail in Fig. 4.3 and Fig. 4.4, respectively.

Short laser light pulses (Fig. 4.2, dark blue line) are transmitted into the atmosphere, where they are scattered on molecules, aerosols and cloud particles. The backscattered light (Fig. 4.2, light blue line) is collected with a telescope and directed to an optical receiver were it is spectrally resolved and detected. Thereby, the frequency shift between transmitted and detected light is proportional to the wind speed, as moving scatterer (molecules and aerosols that are moving with wind speed) cause a Doppler frequency shift in the scattered light. A more detailed explanation of wind retrieval by using the A2D is given by Paffrath (2006) and Reitebuch et al. (2009).
In the following, the attention is directed to the discussion of the components and properties of the A2D instrument that are relevant for the performed SRBS experiments. A more detailed description of the A2D instrument specifications is given by Durand et al. (2006, 2005), Reitebuch et al. (2004, 2009) and Paffrath (2006). A detailed overview of the laser transmitter and its frequency stability is given by Schröder et al. (2007) and Witschas (2007).

The A2D laser transmitter consists of a frequency-tripled, diode pumped, pulsed Nd:YAG laser with an output energy of 60 - 70 mJ, a pulse repetition rate of 50 Hz, a pulse duration of 25 ns (FWHM), and a line width of 45 MHz (FWHM) at a wavelength of 354.89 nm. A schematic block diagram of the A2D laser transmitter is displayed in Fig. 4.3.

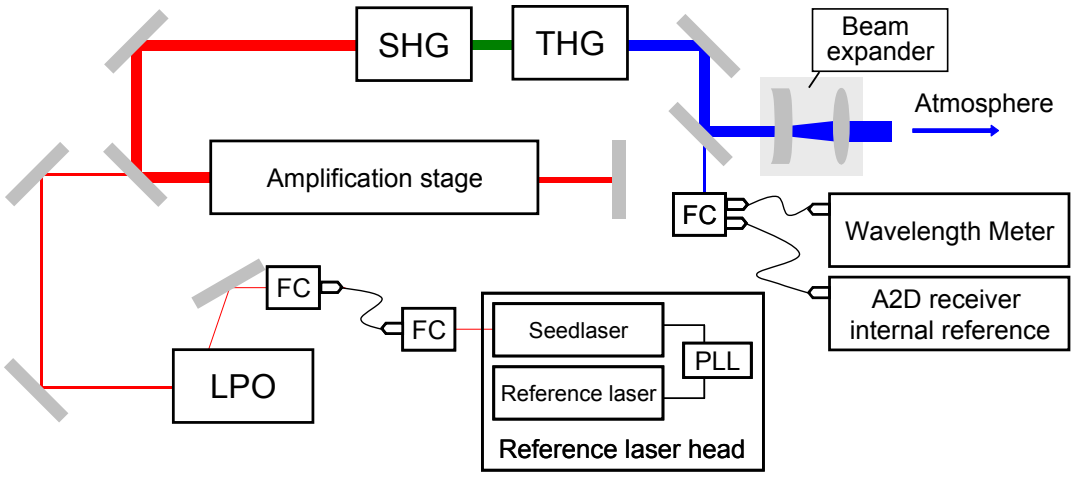

Figure 4.3: Schematic diagram of the A2D laser transmitter: red: Nd:YAG laser beam (1064 nm); green: frequency doubled laser beam (532 nm); blue: frequency tripled laser beam (355 nm); black: fibers; LPO: low power oscillator; PLL: phased locked loop; FC: fiber coupler; SHG: second harmonic generation; THG: third harmonic generation.

The reference laser head, specifically designed and developed by Innolight GmbH, is a low power, continuous wave, frequency tunable laser system (1064 nm) with high frequency stability (234 kHz root mean square over 25 min.), which is required for SRBS experiments to avoid an influence of the laser spectral drift on the detected SRB line shape. It consists of two identical laser systems (reference and seed laser) based on non-planar ring geometry. To hold and tune the seed laser at a defined frequency offset against the frequency stable reference laser, a phased-locked loop (PLL) controller is used. With this configuration it is possible to tune the seed laser frequency over a range of about 12 GHz (at 355 nm) single frequency and without laser mode hopping. This allows sampling the SRB line shape of the scattered light by changing the laser's frequency with defined frequency steps over a frequency range of 12 GHz[5]. The seed laser radiation is used as injection seeder for the low power oscillator (LPO) which is composed of a transversally pumped Nd:YAG rod placed between a concave high reflective mirror and a convex Gaussian variable reflectivity mirror which is used as output coupler to ensure good output beam parameters. For the generation of actively controlled laser pulses a Q-switch is used. With the presented configuration and a cavity length of about 30 cm, pulse durations of about 35 ns (FWHM) at 1064 nm are obtained. To ensure resonance between the LPO cavity length and the seed laser radiation, the cavity length is controlled by the ramp and fire technique (Fry et al., 1991; Henderson et al., 1986; Nicklaus et al., 2007; Schmitt and Rahn, 1986). In order to reach a pulse energy of up to 70 mJ, the LPO radiation is directed to the amplification stage which consists of two amplifiers of equal design. The amplifier laser crystals are designed in slab geometry to ease the removal of the strong thermal load deposited in the laser crystal by the pump laser light. Between the two amplifier stages, three beam turning mirrors rotate the beam spatially by 90° after each pass for compensation of thermally induced astigmatism. After amplification, the UV radiation is obtained by second and third harmonic generation (SHG, THG). For this purpose, LBO (LiB_3O_5) crystals are used in critical phase-matching orientation. Both crystals are temperature stabilized at 35 °C. High quality anti-reflection coatings at the entrance and exit faces of the SHG crystal (double band coating at 1064 nm and 532 nm) and THG crystal (triple band coating at 1064 nm, 532 nm and 355 nm) minimize the optical losses. The laser UV

[5]Using the Gaussian approximation (Eq. 2.16) the FWHM of SRB scattered light is calculated to be about 3 - 4 GHz for a laser wavelength of 355 nm and atmospheric pressures (0 hPa - 1013 hPa) and temperatures (220 K - 330 K). Thus, the frequency range of 12 GHz is large enough to resolve to entire SRB line shape.

wavelength is continuously monitored with a commercial wavelength meter (High Finesse WS Ultimate 10) which allows to measure the absolute mean wavelength for 4-6 pulses with an accuracy of 2 MHz (corresponding to a relative accuracy of $2{\cdot}10^{-9}$), thanks to a continuously ($\approx$ every 100 s) performed calibration with a frequency-stabilized He-Ne laser. To yield a laser beam divergence of less than 100 μrad ($\pm 3\,\sigma$), the laser beam is expanded to a diameter of 11 mm ($\pm 2\,\sigma$) before it is sent into the atmosphere. The laser beam profile and divergence of the outgoing laser beam at 355 nm was characterized by using the converging lens method according to ISO 11146: 1999, resulting in a M^2 value of 1.2 and a divergence below 90 μrad ($\pm 3\,\sigma$).

The backscattered light from the atmosphere is collected with a Cassegrain telescope which is composed of a 200 mm concave, aspheric primary mirror and a 75 mm convex spherical secondary mirror with a telescope focal length of 1.5 m. The collected light is directed to the optical receiver.

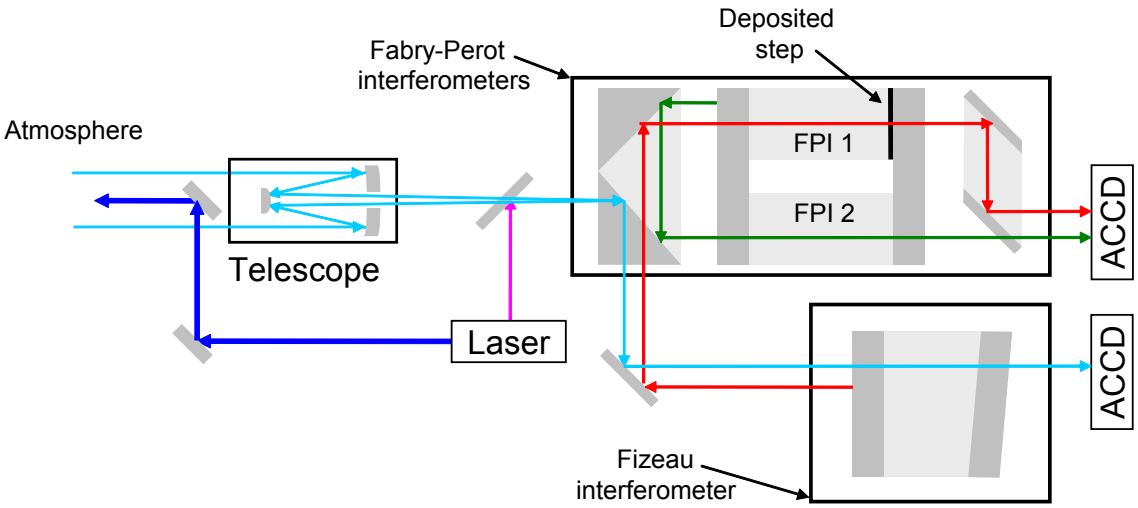

Figure 4.4: Schematic diagram of the A2D receiver: dark blue: UV laser beam which is sent into the atmosphere; light blue: backscattered light which is collected with a telescope and directed to the Fizeau interferometer where it is partly transmitted and detected by the ACCD; red: light which is reflected from the Fizeau interferometer and directed to the first FPI, where it is partly transmitted and detected by the ACCD; green: light which is reflected from the first FPI is directed to the second FPI, where it is transmitted and detected by the ACCD; pink: internal reference signal from the laser which is couplet into receiver, following the light blue, red, and green line.

The A2D receiver consists of a Fizeau interferometer, used to analyze the spectrally narrow backscatter signal from aerosols, and two spectrally separated FPIs to analyze the spectrally broad backscatter signal from molecules. For both the FPIs and the Fizeau interferometer, an accumulation charge-coupled device (ACCD) is used as a detector.

The interferometer outputs are imaged onto a zone of the ACCD with a small number of 16·16 pixel, each with a size of 27^2 μm^2. Unlike ordinary CCD detectors, the ACCD allows the electronic charges from several atmospheric returns to be accumulated directly on the CCD within a second non-illuminated zone, the so-called memory zone (Reitebuch et al., 2009). This on-chip accumulation allows reading out the electronic charges with low readout noise. The schematic layout of the A2D receiver is given in Fig. 4.4.

The scattered light (Fig. 4.4, light blue), collected by the telescope, is first directed to the Fizeau interferometer. The Fizeau interferometer thereby acts as a narrow band filter with a FWHM of Δf_{FWHM} = 137 MHz, which is used to analyze the spectrally narrow signal from light scattered on aerosols. However, most of the incoming signal (90 - 100 %) is reflected from the Fizeau interferometer and is directed to the first FPI (Fig. 4.4, red, FPI 1) which has a mirror separation of 13.68 mm leading to a free spectral range of Γ_{FSR} = 10.95 GHz and a FWHM of Δf_{FWHM} = 1.78 GHz. A more detailed discussion of the intensity transmission curve of FPI 1 is given in section 4.2.3. The light, reflected from FPI 1 is directed to the second FPI (FPI 2, Fig. 4.4, green). FPI 2 has the same configuration as FPI 1 but a slightly different mirror separation because of a deposited step which is only present for FPI 1 (Fig. 4.4). This leads to an intensity transmission curve which is spectrally shifted to the one of FPI 1 as common for wind measurements by using the double edge technique (Flesia and Korb, 1998; Gentry et al., 2000).

For the performed SRBS experiments, only the signal transmitted to FPI 1 (Fig. 4.4, red line) is used for data analysis. The transmission behavior of this FPI is extensively discussed in the following.

4.2.3 Instrument function of the plane-parallel Fabry-Perot interferometer

In Section 3.2.2 it was shown that the transmission function of an ideal FPI (axially parallel beam of rays, mirrors perfectly parallel to each other, mirrors of infinite size, mirrors without any defects) can be expressed by an Airy function (Eq. 3.1). It was also pointed out that Eq. 3.1 can be used to accurately describe the instrument function of the spherical FPI used for laboratory measurements.

This circumstance is different in the specific case of the plane-parallel FPI used for atmospheric measurements. In Fig. 4.5, the FPI transmission curve, measured by scanning the laser frequency in 50 MHz steps over a frequency range of 20 GHz, is shown for 2 complete free spectral ranges (left, black dots). The blue line indicates the best fit of Eq. 3.1 to the data. It is obvious from the right graph of Fig. 4.5, that there are discrepancies between measured data and fit of Eq. 3.1, especially in the "transmission valley". As these discrepancies lead to a systematic error in the analysis of the measurement data, their origin must be investigated.

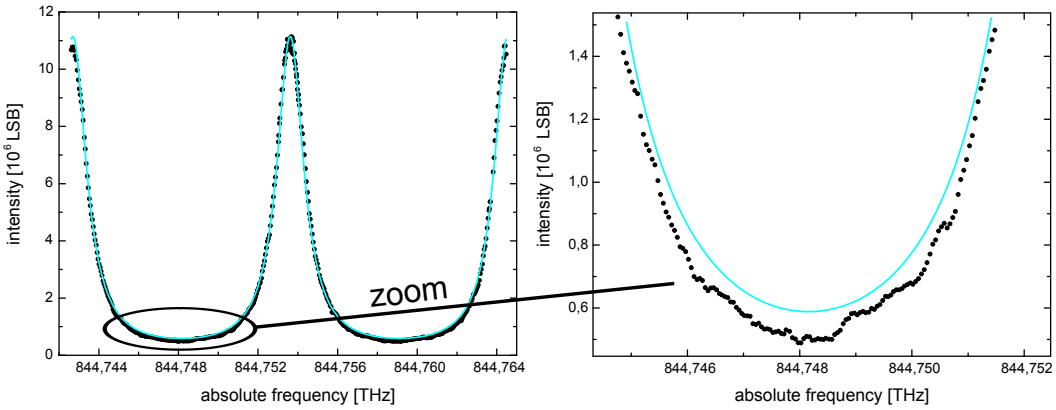

Figure 4.5: Transmission (in least significant bits (LSB)) curve of the plane-parallel FPI versus absolute frequency, obtained with the narrow-band laser internal reference by changing the laser frequency in 50 MHz steps (black dots) over a frequency range of 20 GHz, showing 2 complete free spectral ranges (left) and details of the transmission curve (right). The absolute frequency of the laser was determined by a wavelength meter delivering an absolute accuracy of 2 MHz. The best fit of the Airy function (Eq. 3.1) is indicated by the blue line.

The origin of the discrepancies between measured transmission curve and Eq. 3.1 are imperfections and irregularities on the FPI mirror's surface. For instance, microscopic imperfections on the mirrors, errors in their parallel alignment, or non-uniformities in the reflective coatings cause the effective mirror separation to vary across the face of

the interferometer, which in turn leads to a transmission function which departs from an Airy function. As a precise knowledge of the FPI transmission curve is needed to accurately extract the spectrum of the molecular scattered light, obtained within SRBS experiments, a FPI transmission model that takes the last mentioned plate defects into account must be applied. In the following, different FPI transmission function models that take the various kinds of mirror imperfections into account are derived and compared to each other. After doing so, it is verified and concluded that the implementation of a global defect parameter can be used for the description of the present FPI transmission curve[6].

Basically, surface defects cause a varying mirror separation. Without loss of generality, it can be assumed that these separation changes are caused only by one of the mirrors, while the other one is viewed to be perfect. Using this description, it is possible to treat the FPI as a composition of elementary interferometers with different plate separations, caused by the various kinds of plate defects. The final intensity transmission function $\mathcal{I}(f)$ of the FPI is then obtained by summing the intensities of each of the generated elementary interferometers (Wilksch, 1985). Using this approach it can be shown (Bhatnagar et al., 1974; Hernandez, 1966; Wilksch, 1985) that $\mathcal{I}(f)$ is calculated by the convolution of the Airy function $\mathcal{A}(f)$ (Eq. 3.1), as the transmission function of an ideal FPI, with a mirror surface defect function $\mathcal{D}_x(f)$ according to

$$\mathcal{I}(f) = \mathcal{A}(f) * \mathcal{D}_x(f) = \int_{-\infty}^{\infty} \mathcal{D}_x(g)\mathcal{A}(f-g)\, dg \tag{4.1}$$

Depending on the kind of defect, there are several approaches for defining appropriate defect functions $\mathcal{D}_x(f)$, which have been examined by several authors (Bayer-Helms, 1963; Bhatnagar et al., 1974; Chabbal, 1954; Hays and Roble, 1971; Hernandez, 1966; Palik et al., 1996; Wilksch, 1985). For instance, in the case of microscopic flatness imperfections on the mirror's surface, the mirror separation can be viewed to vary randomly, and the corresponding defect function $\mathcal{D}_g(f)$ (Fig. 4.6, left) is described by a Gaussian function (Chabbal, 1954; Hays and Roble, 1971; Hernandez, 1966)

$$\mathcal{D}_g(f) = \frac{1}{\sqrt{2\pi}\sigma_g} \exp\left(-\frac{f^2}{2{\sigma_g}^2}\right) \tag{4.2}$$

where σ_g is the defect parameter, indicated by the standard deviation of $\mathcal{D}_g(f)$.

[6] McGill et al. (1997a,b) suggested the use of a Gaussian distributed global defect parameter instead of describing the various kinds of plate defects by their physical origin. This approach leads to a simpler mathematical description which makes the data analysis easier.

In case of spherical bowing of the mirrors or any aperture effects, the surface defect function is expressed by a rectangular function $\mathcal{D}_r(f)$ (Fig. 4.6, middle) according to (Chabbal, 1954; Hays and Roble, 1971; Hernandez, 1966)

$$\mathcal{D}_r(f) = \begin{cases} \frac{\Gamma_{\mathrm{FSR}}}{4\,\pi\,\sigma_r} & \text{, for } |f| \leq \frac{2\,\pi\,\sigma_r}{\Gamma_{\mathrm{FSR}}} \\ 0 & \text{, for } |f| > \frac{2\,\pi\,\sigma_r}{\Gamma_{\mathrm{FSR}}} \end{cases} \tag{4.3}$$

where σ_r is the defect parameter, defined by the half width of the rectangle. For considering plate defects which lead to an asymmetric modification of the FPI transmission function it is possible to define a tilted rectangular defect function $\mathcal{D}_{tr}(x)$ (Fig. 4.6, right) according to

$$\mathcal{D}_{tr}(f) = \begin{cases} \frac{\Gamma_{\mathrm{FSR}}}{8\,\pi^2\sigma_{tr}^2}\left[(4\,\pi\,\sigma_{tr}\,b + \Gamma_{\mathrm{FSR}})\cdot f + 2\,\pi\sigma_{tr}\right] & \text{, for } |f| \leq \frac{2\,\pi\,\sigma_{tr}}{\Gamma_{\mathrm{FSR}}} \\ 0 & \text{, for } |f| > \frac{2\,\pi\,\sigma_{tr}}{\Gamma_{\mathrm{FSR}}} \end{cases} \tag{4.4}$$

where σ_{tr} is the defect parameter, defined by the half width of the rectangle, and b is the step height of the smaller side (Fig. 4.6). It is worth mentioning that all defect functions are normalized to yield unit integrated area, and therefore, they do not influence the integrated transmitted intensity through the FPI, but only its spectral distribution. For a better illustration, the last mentioned defect functions are depicted in Fig. 4.6.

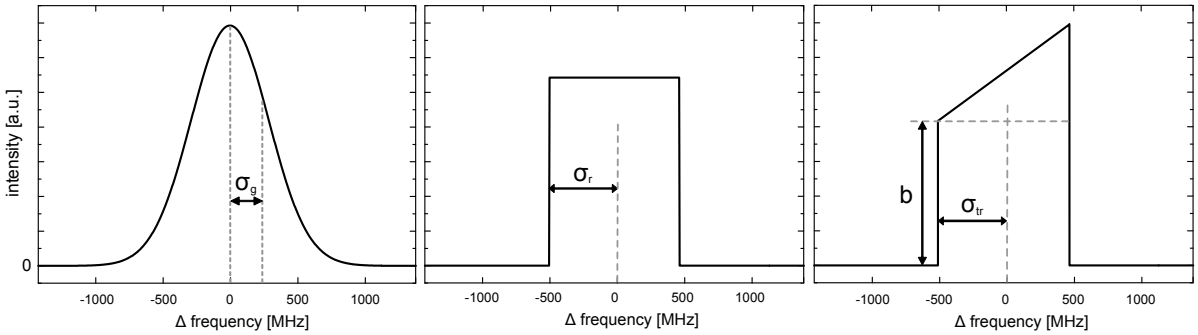

Figure 4.6: Different defect functions $\mathcal{D}_x(f)$ used for the calculation of the transmission function of the FPI. (left) Gaussian shaped defect function $\mathcal{D}_g(f)$ with standard deviation σ_g for considering microscopic imperfections on the FPI mirrors. (middle) Rectangular shaped defect function $\mathcal{D}_r(f)$ with half width σ_r for considering spherical bowing of the FPI mirrors, and any aperture effects. (right) Tilted rectangular shaped defect function $\mathcal{D}_{tr}(f)$, defined by half width σ_{tr} and step height b, for considering asymmetric defects.

The transmission function of a FPI with mirror imperfections can now be calculated with Eq. 4.1 by using the various defect functions Eq. 4.2 - 4.4. As pointed out by Krebs

and Sauer (1953), this evaluation is much more convenient if the Airy function $\mathcal{A}(f)$ is expanded into its Fourier series according to

$$\mathcal{A}(f) = \frac{1}{\Gamma_{\mathrm{FSR}}} \left(1 + 2 \sum_{k=1}^{\infty} R^k \cos\left(\frac{2\,k\,\pi\,f}{\Gamma_{\mathrm{FSR}}} \right) \right) \tag{4.5}$$

Here, all quantities are defined as in Eq. 3.1, and R is the reflectivity of the mirrors[7]. The index of refraction of the medium between the mirrors is set to be unity and only light with perpendicular incident angle is considered[8]. The FSR of the plane-parallel FPI is $\Gamma_{\mathrm{FSR}} = c/2d$, were c is the light velocity in vacuum and d the mirror separation. Furthermore, the dispersion relation $\lambda = c/f$, with λ is the light's wavelength, and f the light's frequency, is used. By further using $\cos(f-g) = \cos(f)\cdot\cos(g) + \sin(f)\cdot\sin(g)$, the intensity transmission of the FPI according to Eq. 4.1 can be written as

$$\begin{aligned} \mathcal{I}_x(f) \;=\; & \frac{1}{\Gamma_{\mathrm{FSR}}} \int_{-\infty}^{\infty} \mathcal{D}_x(g)\; dg \\ & + \frac{2}{\Gamma_{\mathrm{FSR}}} \sum_{k=1}^{\infty} R^k \cos\left(\frac{2\,k\,\pi\,f}{\Gamma_{\mathrm{FSR}}} \right) \int_{-\infty}^{\infty} \mathcal{D}_x(g) \cos\left(\frac{2\,k\,\pi\,g}{\Gamma_{\mathrm{FSR}}} \right)\; dg \\ & + \frac{2}{\Gamma_{\mathrm{FSR}}} \sum_{k=1}^{\infty} R^k \sin\left(\frac{2\,k\,\pi\,f}{\Gamma_{\mathrm{FSR}}} \right) \int_{-\infty}^{\infty} \mathcal{D}_x(g) \sin\left(\frac{2\,k\,\pi\,g}{\Gamma_{\mathrm{FSR}}} \right)\; dg \end{aligned} \tag{4.6}$$

As the defect functions are normalized to unit integrated area, the integral in the first argument of Eq. 4.6 is equal to 1. The integral in the third argument contains the integration of the product of the odd sin - function with the defect function from $-\infty$ to $+\infty$, and therefore, it is equal to 0 for all symmetrical[9] defect functions $\mathcal{D}_x(f)$. For that special case, only the integral in the second argument of Eq. 4.6 has to be evaluated. The evaluation of Eq. 4.6 in the case where microscopic imperfections according to $\mathcal{D}_g(f)$ (Eq. 4.2) are considered yields an intensity transmission function $\mathcal{I}_g(f)$ according to

$$\mathcal{I}_g(f) = \frac{1}{\Gamma_{\mathrm{FSR}}} \left(1 + 2 \sum_{k=1}^{\infty} R^k \cos\left(\frac{2\,\pi\,k\,f}{\Gamma_{\mathrm{FSR}}} \right) \exp\left(-\frac{2\,\pi^2\,k^2\,{\sigma_g}^2}{{\Gamma_{\mathrm{FSR}}}^2} \right) \right) \tag{4.7}$$

[7] In Sec. 3.2.2, the Airy function was defined by using the full width at half maximum $\Delta \mathrm{f}_{\mathrm{FWHM}}$. The relation between $\Delta \mathrm{f}_{\mathrm{FWHM}}$ and the reflectivity of the mirrors is approximately (arcsin(x)≈(x) for small x) given by Vaughan (1989): $\Delta \mathrm{f}_{\mathrm{FWHM}} = (\Gamma_{\mathrm{FSR}} \cdot (1-R))/(\pi \cdot \sqrt{R})$.

[8] The space between the mirrors is evacuated, and therefore, the index of refraction is unity. The opening angle at the FPI is 1 mrad, and therefore, the assumption of perpendicular incident light is valid.

[9] This is true for the Gaussian defect function (Eq. 4.2) and the rectangular defect function (Eq. 4.3), but not for the tilted rectangular defect function (Eq. 4.4).

In the case of considering the effect of spherical bowing and aperture effects according to $\mathcal{D}_r(f)$ (Eq. 4.3), the intensity transmission function $\mathcal{I}_r(f)$ yields

$$\mathcal{I}_r(f) = \frac{1}{\Gamma_{\mathrm{FSR}}}\left(1 + 2\sum_{k=1}^{\infty} R^k \cos\left(\frac{2\,\pi\,k\,f}{\Gamma_{\mathrm{FSR}}}\right)\mathrm{sinc}\left(\frac{2\,\pi\,k\,\sigma_r}{\Gamma_{\mathrm{FSR}}}\right)\right) \tag{4.8}$$

where

$$\mathrm{sinc}\left(\frac{2\,\pi\,k\,\sigma_r}{\Gamma_{\mathrm{FSR}}}\right) = \sin\left(\frac{2\,\pi\,k\,\sigma_r}{\Gamma_{\mathrm{FSR}}}\right)\cdot\left(\frac{2\,\pi\,k\,\sigma_r}{\Gamma_{\mathrm{FSR}}}\right)^{-1} \tag{4.9}$$

In the case of considering the asymmetric tilted rectangle defect function $\mathcal{D}_{tr}(f)$, also the third argument in Eq. 4.6 has to be evaluated. Although this evaluation is analytically possible, it leads to a rather large equation according to

$$\begin{aligned}\mathcal{I}_{tr}(f) \;=\; & \frac{1}{\Gamma_{\mathrm{FSR}}}\cdot[1+ \\ & +\frac{2}{\Gamma_{\mathrm{FSR}}}\sum_{k=1}^{\infty} R^k\,\cos\left(\frac{2\,\pi\,k\,f}{\Gamma_{\mathrm{FSR}}}\right)\mathrm{sinc}\left(\frac{2\,\pi\,k\,\sigma_{tr}}{\Gamma_{\mathrm{FSR}}}\right) \\ & +\frac{2}{\Gamma_{\mathrm{FSR}}}\sum_{k=1}^{\infty}\frac{-R^k\,\Gamma_{\mathrm{FSR}}\,\sin\left(\frac{2\,\pi\,k\,f}{\Gamma_{\mathrm{FSR}}}\right)(b\,\sigma_{tr}-1)}{{\sigma_{tr}}^2\,\pi^2\,k^2}\cdot \\ & \cdot\left(\Gamma_{\mathrm{FSR}}\,\sin\left(\frac{\pi\,k\,\sigma_{tr}}{\Gamma_{\mathrm{FSR}}}\right) - \sigma_{tr}\,\pi\,k\,\cos\left(\frac{\pi\,k\,\sigma_{tr}}{\Gamma_{\mathrm{FSR}}}\right)\right)\Bigg]\end{aligned} \tag{4.10}$$

It is worth mentioning that in the special case were $b = 1/\sigma_{tr}$, Eq. 4.10 reduces to Eq. 4.8, which was calculated for the rectangular defect function. Furthermore, it should be pointed out that it is possible to take more than one kind of defect into account. For instance if one wants to consider microscopic imperfections and spherical bowing of the mirrors, Eq. 4.7 has to be expanded by the sinc-term as mentioned in Eq. 4.9. However, the exact origin of defects is not of any interest for this work, and thus only single mirror defects are considered in the following.

To investigate the appropriateness of the different model functions (Eq. 4.7 - 4.10) they, as well as the "pure" Airy function (Eq. 4.5), are fitted to the measured transmission curve. By using a downhill simplex fit procedure (Press, 2007), best fit values for the free spectral range Γ_{FSR}, the mirror reflectivity R, the center frequency f_0, and the respective defect parameter σ_x are obtained. For the least squares fit, the sum in Eq. 4.5 and Eq. 4.7 - 4.10 is evaluated from $k = 1$ to $k = 25$ which is sufficient, as the contribution of

sum terms higher then $k = 25$ is only $\approx 10^{-5}$ (assuming a mean reflectivity of $R = 0.66$). After the best fit is obtained, the accordance between measured data $\mathcal{I}_{\mathrm{meas}}(f)$ and model function $\mathcal{I}_x(f)$ is investigated by the relative deviation $\Delta\mathcal{I}$ and a χ^2 value according to

$$\Delta\mathcal{I} = \frac{\mathcal{I}_{\mathrm{meas}}(f_N) - \mathcal{I}_x(f_N)}{\mathcal{I}_x(f_N)} \qquad \text{and} \qquad \chi^2 = \frac{1}{N}\sum_{k=1}^{N}(\Delta\mathcal{I})^2 \tag{4.11}$$

where N is the number of measurement points[10]. The measured FPI transmission curve, the best fit of Eq. 4.5, Eq. 4.7 - 4.10 and the relative deviation according to Eq. 4.11 are shown in Fig. 4.7. The obtained best fit parameters can be found in Table 4.1.

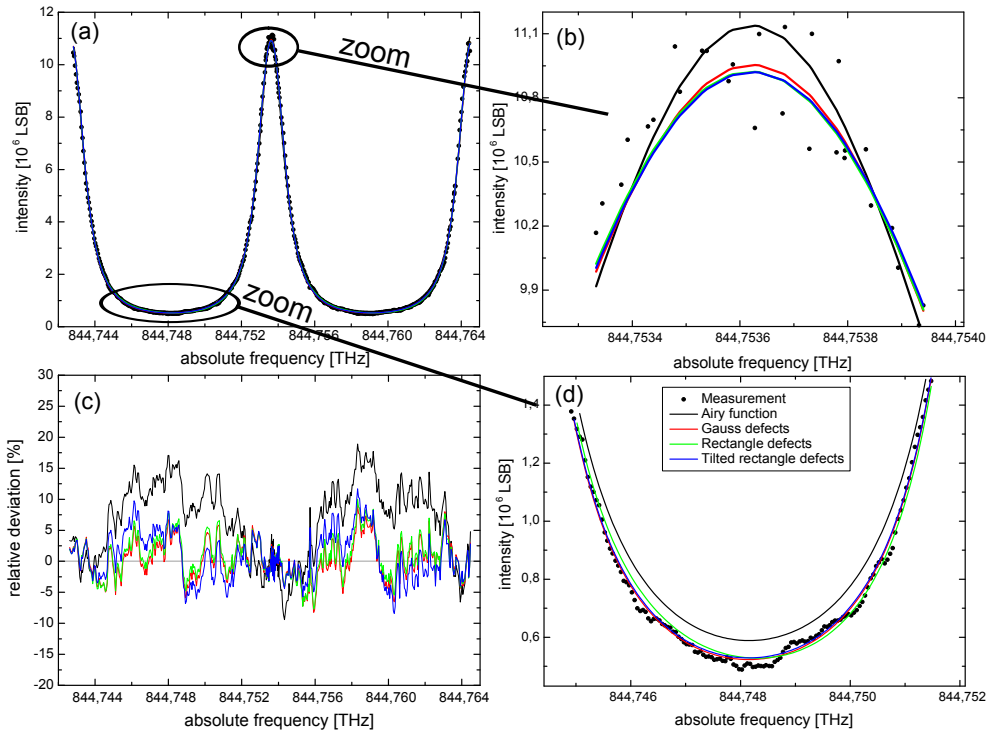

Figure 4.7: (a) Measured transmission function of the plan-parallel FPI versus absolute frequency (black dots) and best fit to the measurement data by considering no defects and using the Airy function according to Eq. 4.5 (black line), by considering Gaussian defects according to Eq. 4.7 (red line), by considering rectangle defects according to Eq. 4.8 (green line), and by considering tilted rectangle defects according to Eq. 4.10 (blue line). (b) and (d) Details of the transmission curve in the region of the intensity transmission maximum and minimum, respectively. (c) Relative deviation between measurement and the different model functions. Colored lines are the same in all graphs.

It is obvious from Fig. 4.7, that the measured transmission curve is well described by all defect model transmission functions (red, green, and blue line), whereas there are distinct discrepancies in the case where the ordinary Airy function (black line) is used.

[10] In $\Delta\mathcal{I}$, the difference between fit an measurement is normalized to $\mathcal{I}_x(f_N)$ at each discrete frequency step instead of normalizing it to the maximum intensity. This is done to better visualize the differences at the transmission valley of the FPI.

The model of the Airy function leads to a relative deviation to the measurement of up to 15 %, whereas the relative deviation is randomly varying between ± 5 % in case of using the defect model functions. For the Airy model, $\chi^2 = 7.86 \cdot 10^{-3}$, whereas $\chi^2 = 0.98 \cdot 10^{-3}$ in case of using the Gaussian defect function, $\chi^2 = 1.08 \cdot 10^{-3}$ in case of using the rectangular defect function and $\chi^2 = 1.49 \cdot 10^{-3}$ in case of using the tilted rectangular function. It is obvious that the accordance between measurement and model function is increased when mirror defects are considered, which is also demonstrated by the smaller χ^2 values for mirror defect model functions. It should be noted that in case of considering plate defects, the obtained reflectivity R as well as the full width at half maximum Δf_{FWMH} is larger than for considering the Airy function. For R, this is due to the fact that in case of considering mirror defects, the width of the transmission curve results from the width of the Airy function of an ideal FPI (which is given due to R) convolved with the width of the defect function. Thus, the width of the Airy function has to be smaller as it gets additionally broadened by the defect function. For Δf_{FWMH}, this is solely because of a better description of the measurement. This demonstrates that it is necessary to consider mirror defects for calculating the intensity transmission of the FPI. However, it also shows that the actual shape of the applied defect function plays only a minor role. Therefore, I will follow the suggestion of McGill et al. (1997a), and use $\mathcal{I}_g(f)$ (Eq. 4.7) to describe the instrument function of FPI 1 used for atmospheric measurements.

The exact intensity transmission curve of the plane-parallel FPI, which is the instrument function of the system, was accurately determined from 8 different measurements at different days under equal conditions[11]. The measurements were performed with 50 MHz frequency steps over a frequency range of 20 GHz. Using these measurements, the mean values and their standard deviation are given by $\Gamma_{\mathrm{FSR}} = [10934 \pm 23]$ MHz, $R = 0.659 \pm 0.004$, $\Delta f_{\mathrm{FWHM}} = [1765 \pm 31]$ MHz and $\sigma_g = [296 \pm 23]$ MHz.

Table 4.1: Comparison of fit parameters for different FPI transmission function models

$\mathcal{I}_x(f)$	Γ_{FSR} [MHz]	**R**	Δf_{FWMH} [MHz]	f_0 [THz]	σ_x [MHz]	χ^2 Eq.4.11
$\mathcal{A}(f)$ (Eq. 4.5)	10928	0.626	1644	844.753621	-	$7.86 \cdot 10^{-3}$
$\mathcal{I}_g(f)$ (Eq. 4.7)	10948	0.659	1760	844.753622	288	$0.98 \cdot 10^{-3}$
$\mathcal{I}_r(f)$ (Eq. 4.8)	10948	0.656	1760	844.753623	461	$1.08 \cdot 10^{-3}$
$\mathcal{I}_{tr}(f)$ (Eq. 4.10)	10948	0.656	1760	844.753616	459[a]	$1.49 \cdot 10^{-3}$

[a] Parameter b = $2.17 \cdot 10^{-3}$ MHz, and therefore it is almost $1/\sigma_{tr}$.

[11] The temperature of the FPI was $T = 18.5\,^{\circ}\mathrm{C}$, stabilized with an accuracy of $\pm 1 \cdot 10^{-3}$ K.

4.2.4 Measurement principle

The main objective of the BRAINS campaign was to demonstrate the Brillouin effect in the atmosphere for the first time and to verify the Tenti S6 model for its ability to describe the SRB line shape in air. To achieve this goal, the A2D lidar instrument was setup in a laboratory of the UFS as illustrated in Fig. 4.8, left. In the following, the measurement procedure, performed to resolve the SRB line shape of light scattered from the atmosphere is described.

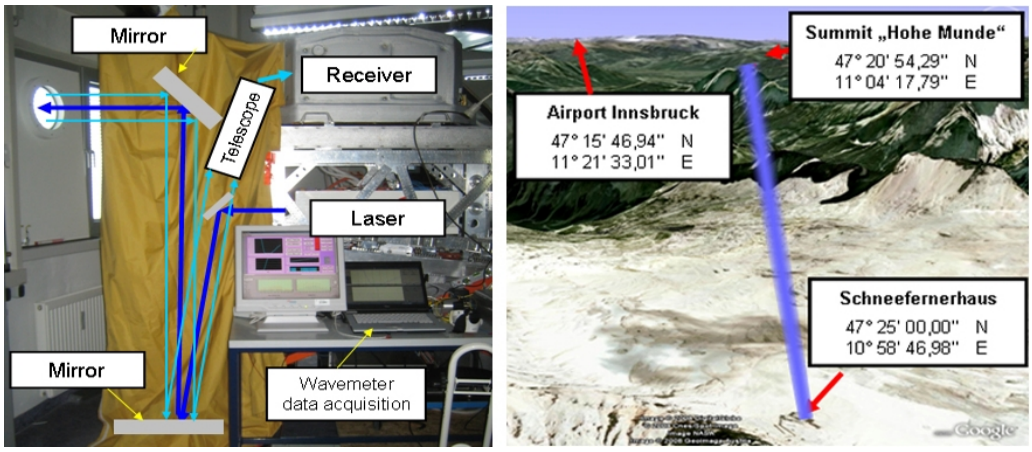

Figure 4.8: A2D setup and the Schneefernerhaus location. (left) The A2D lidar setup at the UFS laboratory. The laser beam, directed into the atmosphere, is indicated by dark blue arrows, the backscattered light from the atmosphere by light blue arrows. (right) Pointing direction of the laser beam in viewing direction from the UFS. The geographic coordinates of the Schneefernerhaus, the summit Hohe Munde (used for horizontal beam alignment) and the airport of Innsbruck (daily radiosonde launches), are indicated (perspective view from Google earth).

To improve the signal to noise ratio of the measured SRB line shape, the detected backscatter signal is averaged over several kilometers. To assure constant atmospheric pressure and temperature, and therefore a constant SRB line shape of the scattered light within the averaged range, a horizontal alignment of the outgoing laser beam is needed. This is realized by using the hard target return of a mountain called "Hohe Munde", in about 10.2 km distance from the UFS (Fig. 4.8, right). As the altitude of the "Hohe Munde" (2662 m) equals that of the UFS (2650 m - 2670 m), the laser beam was aligned in a way that it just passes the summit (verified by analyzing the strength of the backscattered signal at a distance of 10 km - 11 km away from the UFS). With this procedure, a horizontal pointing of the laser beam was achieved with $\pm$ 10 m over 10 km distance.

To obtain the resolved SRB line shape of the scattered light, it is sampled by changing the laser frequency with defined frequency steps of 50 MHz over a frequency range of 12 GHz (at 354.89 nm), and therefore, the SRB line shape is sampled with 240 points. One observation with 700 laser pulses is performed per frequency step within 14 s. The laser frequency is changed after each observation during 4 s, a period which is needed for data transfer. A subsample of all frequency steps, measured with a wavelength meter during SRB line shape sampling is shown in Fig. 4.9, left. With 240 steps and a duration of 18 s per frequency step, the sampling of the entire SRB line shape requires 72 minutes. This means that the laser, the receiver as well as the atmospheric conditions have to be stable within this period. The accuracy of laser frequency determination with the wavelength meter is 2 MHz. The mean laser frequency value of one observation is obtained by averaging the wavemeter data over the data acquisition time (14 s), which itself is measured by a trigger signal from the data acquisition unit.

The light scattered from the atmosphere is filtered and resolved by the FPI (Fig. 4.4, FPI 1) and detected with the ACCD. To avoid a spectral drift of the FPI intensity transmission curve, and therefore, an influence on the resolved SRB line shape, the FPI is enclosed in a thermal hood which is temperature stabilized to $\pm$ 10 mK. Furthermore, the FPI transmission curve is measured by using an internal reference signal from the laser (Fig. 4.4, pink). That is, the actual transmission curve is obtained for each measurement and is used for further data analysis.

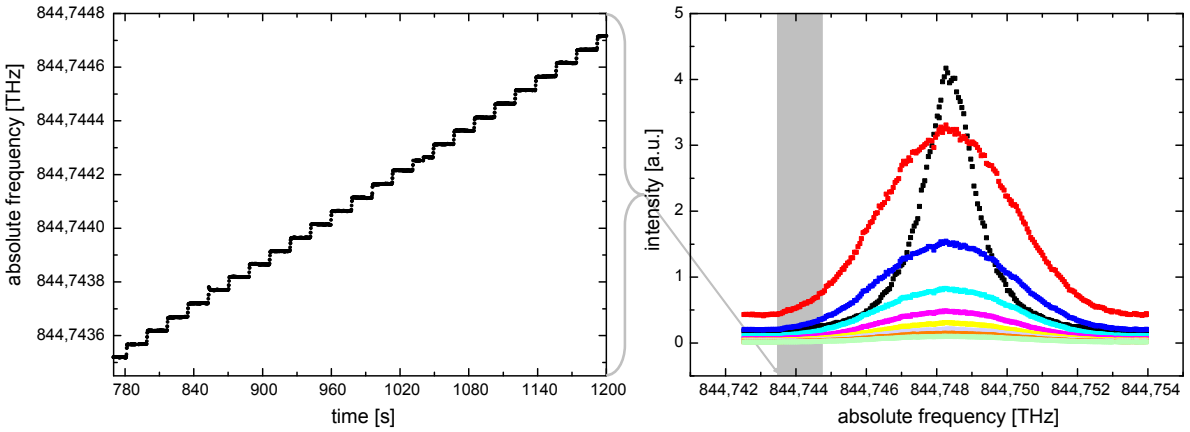

Figure 4.9: Illustration of the atmospheric SRBS measurement principle. (left) Subsample of the measured laser frequency. The step difference of 50 MHz, the step duration of 14 s as well as the frequency change can be seen. (right) FPI transmission curve, measured with the laser internal reference (black dots) and the measured SRB line shapes for different atmospheric range bins (colored dots). The detected signal strength of the backscattered light decreases with increasing distance from the lidar.

The light, passing through the FPI is detected with the ACCD, which thereby integrates charges within a time interval of 4.2 μs, leading[12] to defined range bins of 630 m. Due to the impact of the telescope overlap up to 2 km, and the attenuation of the signal enclosed to the instrument caused by an electro-optical modulator, the first 4 range bins are not used. Only measurements from a distance larger than 2.4 km are used for SRB line shape analysis. To correct the influence of atmospheric background light and detector noise, these quantities are measured in a separate range bin. More details about raw signal corrections are given by Paffrath (2006). An example of the corrected ACCD signal of different range bins for a SRBS measurement is shown in Fig. 4.9. From Fig. 4.9, right it is obvious that the strength of the backscattered signal depends on the distance r from the lidar. Actually it is proportional to r^{-2}. The analysis procedure of the obtained SRB line shapes is discussed in the next section.

4.2.5 Data analysis procedure

The detected signal $\mathcal{I}(f)$ on the ACCD is given by the convolution of the SRB line shape $\mathcal{S}(f)$ of the scattered light and the intensity transmission function $\mathcal{A}(f)$ of the FPI according to

$$\mathcal{I}(f) = \mathcal{S} * \mathcal{A} = \int_{-\infty}^{\infty} \mathcal{S}(f)\mathcal{A}(f-g)\,dg \tag{4.12}$$

It is well known that the convolution of such two functions can alternatively be represented by the product of their individual Fourier transforms

$$\tilde{\mathcal{I}}(k) = \tilde{\mathcal{S}}(k) \cdot \tilde{\mathcal{A}}(k) \tag{4.13}$$

where the transformation is made to the reciprocal k-space. Thus, $\mathcal{S}(f)$ can theoretically be obtained by deconvolution, which means by calculating the reciprocal Fourier transform of $\tilde{\mathcal{I}}(k)/\tilde{\mathcal{A}}(k)$. Such a deconvolution procedure works without difficulties for well behaved analytical functions. However, as discussed by Vaughan (1989), the relative error becomes large for real spectra with random noise, as the noise of the spectrum dominates higher Fourier terms. This is particular evident by considering the transmission curve of an ideal FPI, which is given by the Airy function according to Eq. 3.1. The values of $\tilde{\mathcal{A}}(k)$ get close to zero for large k. This leads to large errors in the calculation of

[12] The range bin thickness Δx can be calculated according to $\Delta x = \Delta t \cdot c/2$, where Δt is the ACCD integration time and c the velocity of light in air. For $\Delta t = 4.2 \cdot 10^{-6}$ s and $c \approx 3 \cdot 10^8$ m/s, the observed range bin thickness Δx is 630 m.

$\tilde{\mathcal{I}}(k)/\tilde{\mathcal{A}}(k)$, and thus, in the deconvolved SRB spectrum. Thus, a precise deconvolution procedure is only applicable for spectra with low noise. As measurements performed in the real atmosphere are exposed to a variety of noise sources, the deconvolution procedure is inappropriate, and another analysis procedure has to be developed. It was tested that even in case of describing $\mathcal{A}(f)$ with the noiseless model function according to Eq. 4.7, the deconvolution procedure yields no reasonable result for $\mathcal{S}(f)$ which is due to the noise in the atmospheric signal $\mathcal{I}(f)$[13].

An adequate alternative for the description of the measured line shape $\mathcal{I}(f)$ would be to evaluate Eq. 4.12 by using $\mathcal{A}(f)$ from Eq. 4.7 and calculating $\mathcal{S}(f)$ according to the Tenti S6 model. However, as the Tenti S6 model is not available in an analytical closed form, this evaluation could only be performed numerically. Thus, also $\mathcal{I}(f)$ is obtained in numerical form, and therefore, a least square fit algorithm can not be used.

To sort out this problem, an analytical function for the description of the measured signal $\mathcal{I}(f)$ is developed as described in the following. A schematic sketch of using the obtained analytical function for the detection of the Brillouin effect within atmospheric measurements is displayed in Fig. 4.10.

The SRB spectrum $\mathcal{S}(f)$ of molecular scattered light can be approximated by a Gaussian line shape due to the thermal motion of the molecules. Using Eq. 2.17 and the relation[14] $f_\sigma = 2\sqrt{k_B\,T/M}/\lambda_0$, the SRB spectrum $\mathcal{S}(f)$ is described by

$$\mathcal{S}(f) = \frac{1}{\sqrt{2\pi}\,\sigma_{\mathrm{sp}}} \exp\left(-\frac{1}{2}\left(\frac{f-f_0}{\sigma_{\mathrm{sp}}}\right)^2\right) \quad \text{with} \quad \sigma_{\mathrm{sp}} = \frac{2}{\lambda_0}\sqrt{\frac{k_B\,T}{M}} \tag{4.14}$$

where f_0 and λ_0 is the light's frequency and wavelength, respectively, k_B the Boltzmann constant, T the gas temperature and M the mass of one molecule.

The transmission function $\mathcal{A}(f)$ of the used FPI is extensively discussed in section 4.2.3. It is demonstrated that the measured intensity is accurately described by Eq. 4.7. Thus, Eq. 4.12 can analytically be evaluated[15] by using the approach demonstrated in sec-

[13] It would be possible to suppress the noise in the raw signal by various kinds of filters, however, it can not be assured that informations of the actual line shape get lost due to this filtering.

[14] The relation between the thermal velocity of molecules and the spectrum of the scattered light is caused by the Doppler effect and is described in section 2.3.

[15] The evaluation of an integral function which has the form of Eq. 4.12 is explicitly discussed in section 4.2.3 (Eq. 4.6).

tion 4.2.3, which leads to

$$\mathcal{I}(f) = \frac{1}{\Gamma_{\mathrm{FSR}}} \left(1 + 2 \sum_{k=1}^{\infty} R^k \cos\left(\frac{2\,\pi\,k\,(f - f_0)}{\Gamma_{\mathrm{FSR}}} \right) \exp\left(- \frac{2\,\pi^2\,k^2\,({\sigma_g}^2 + {\sigma_{\mathrm{sp}}}^2)}{{\Gamma_{\mathrm{FSR}}}^2} \right) \right) \quad (4.15)$$

where Γ_{FSR} is the free spectral range and R is the mirror reflectivity of the used FPI. Eq. 4.15 can now directly be applied to the measured SRB line shape (Fig. 4.10, c) by using ordinary least square fit algorithms. However, as the Gaussian approximation was used to describe $\mathcal{S}(f)$, the effect of Brillouin scattering is neglected within this approach. Thus, the remaining characteristic residual between analytical function and measured data (Fig. 4.10, j) can be expected to be caused by Brillouin scattering.

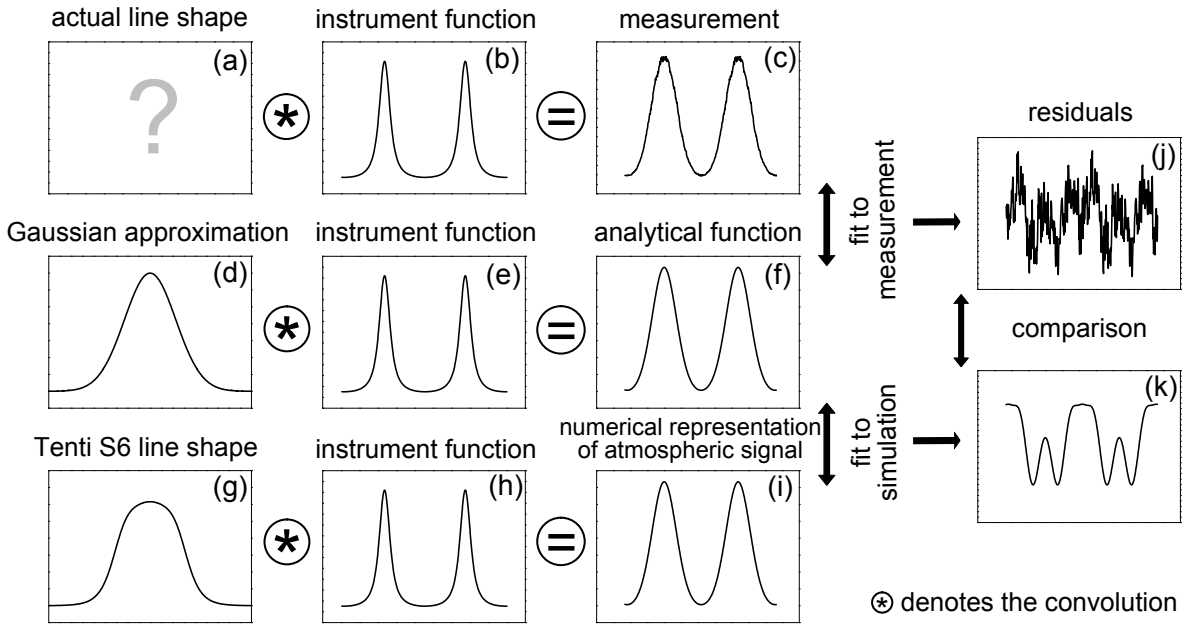

Figure 4.10: Schematic diagram of the data analysis procedure for atmospheric measurements. (a - c): The measured line shape (c) is composed of the convolution of the actual line shape (a) with the instrument function (b). (d - f): An analytical function (f) for describing the measured line shape is developed by convolving a Gaussian line shape (d) with the instrument function (e). This function is an approximation as only Rayleigh scattering is considered, while Brillouin scattering is neglected. Thus, the residual between the measurement and the analytical model function might contain the effect of Brillouin scattering. (g - i): A atmospheric reference signal (i) is simulated by numerically convolving a Tenti S6 modeled SRB line shape (g) (for the same atmospheric conditions as at the measurement) with the instrument function (h). By fitting the analytical function to the simulated line shape, the remaining residual describes the deviation due to Brillouin scattering. (j, k): The residuals between measurement and analytical function, and reference signal and analytical function are calculated and additionally compared to each other.

The main objective of this study was to investigate the validity of the Tenti S6 model in air. Therefore, a reference atmospheric signal is simulated (Fig. 4.10, i) by numerically convolving a Tenti S6 line shape (Fig. 4.10, d), simulated by using the measured atmospheric pressure and temperature values, with the instrument function $\mathcal{A}(f)$ (Fig. 4.10, e). If this simulated atmospheric signal is now analyzed by using Eq. 4.15, the remaining characteristic residual is caused by the effect of Brillouin scattering, which is considered in the simulated atmospheric signal but not in Eq. 4.15.

Now, the residuals between analytical function and measurement data (Fig. 4.10, j) and between analytical function and simulated Tenti S6 line shape (Fig. 4.10, k) can be compared to each other. The degree of correlation is thereby a measure of how well the Tenti S6 model describes SRB line shapes obtained in the atmosphere.

An alternative to the aforementioned analysis procedure would be the use of a recently developed analytical SRB line shape model by Witschas (2011), which is going to be used to analyze BRAINS data in the near future. This model was developed in the framework of this thesis and its derivation is given in appendix A 1.

4.3 Discussion of experimental results

The described measurement principle (section 4.2.4) and the analysis procedure (section 4.2.5) are now applied to an example of a SRBS measurement performed on January 31st at 17:00 UTC. In addition, the results of two other SRBS measurements, performed on January 26 at 19:23 UTC and January 31st at 15:30 UTC are shown and discussed.

Before performing a SRBS measurement, the atmospheric boundary conditions were analyzed, which means that it was verified that almost no aerosols were present in the atmosphere in order to assure a "pure molecular-scattering experiment" without any disturbances due to Mie scattering on aerosols. Furthermore, it was verified that the atmospheric temperature and pressure were constant within the lidar averaging range. On January 31st, the PM10 aerosol particle concentration was measured by UBA[16] to be below 2 $\mu g/m^3$ during the entire day, which indicates a very clear air condition. This circumstance is further visualized by a photograph taken on 31.01.2009 at 16:05 UTC, showing the viewing direction of the laser beam (Fig. 4.11, left).

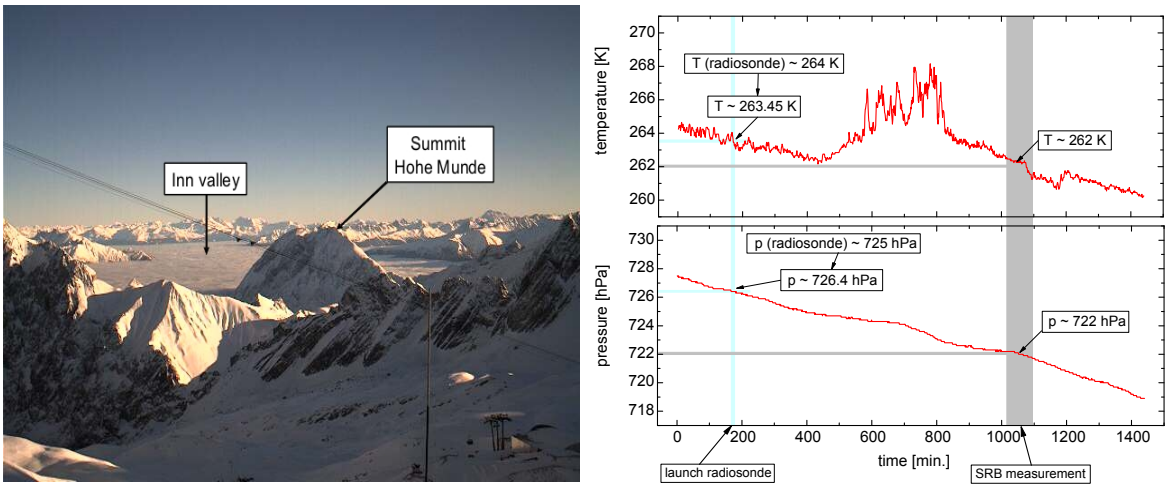

Figure 4.11: (left) Photograph, showing the viewing direction of the laser beam, taken on 31.01.2009 at 16:05 UTC. The mountain Hohe Munde as well as the Inn valley is indicated. The line through the photograph it due to the cable car, going to Zugspitze summit. (right) Temperature (top) and pressure (bottom) versus time, measured by the DWD at the UFS. The time of the radiosonde launch at Innsbruck airport (3:00 UTC) and of the discussed SRBS measurement (17:00 UTC) is indicated by the light blue and light gray bars, respectively. The corresponding mean temperature and pressure value is given. For comparison, the temperature (264 K) and pressure (725 hPa), measured by the radiosonde (at 3:00 UTC) is mentioned. The mean temperature and pressure for the performed SRBS measurement is 262 K and 722 hPa, respectively.

[16]PM stands for particulate matter. The PM10 value is a measure of the particle concentration of particles with diameters up to 10 μm. PM10 Data by courtesy of Dr. L. Ries (UBA).

The atmospheric temperature and pressure is measured by DWD directly at the UFS. Furthermore, temperature and pressure values from the radiosonde, launched at 3:00 UTC from Innsbruck airport (30 km distance to UFS), are available. The time series of the temperature and pressure measurement from January 31st is shown in Fig. 4.11, right. The temperature (264 K) and pressure (725 hPa), measured by the radiosonde[17] is also indicated. By comparing the temperature and pressure values at 3:00 UTC (Fig. 4.11, right, light blue bar, UFS: T = 263.45 K, p = 726.4 hPa; radiosonde: T = 264 K, p = 725 hPa) it is obvious that the values agree within their uncertainty. Hence, the assumption of homogeneous atmospheric conditions is valid for that period and it is further assumed to be valid also for the period of the SRB measurements about 14 h later. The mean temperature and pressure for the performed SRBS measurement are 262 K and 722 hPa, respectively.

The discussed SRBS experiment was performed as described in section 4.2.4. The SRB line shape was sampled by changing the laser frequency in 50 MHz steps over a frequency range of about 12 GHz. Before analyzing the measured SRB line shapes it is necessary to determine the filter parameters of the FPI (section 4.2.5). Within the SRB experiment, the FPI intensity transmission curve is measured by using the laser internal reference (Fig. 4.12, black dots). The filter parameters are obtained by fitting Eq. 4.7 to the measured transmission curve. The measured FPI intensity transmission, the best fit of Eq. 4.7 to it, the residual between fit and measurement, as well as the resulting fit parameters are shown in Fig. 4.12.

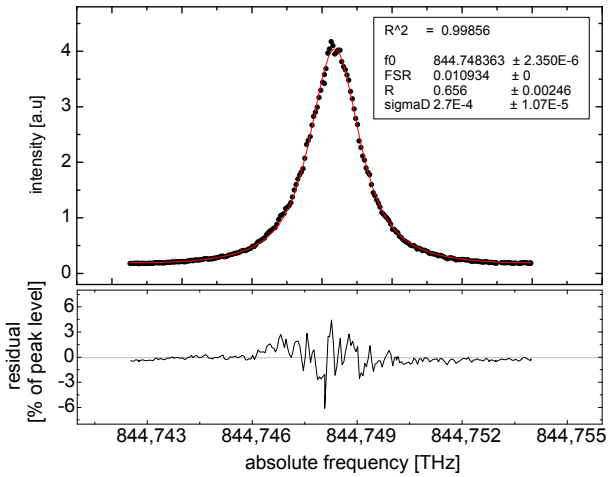

Figure 4.12: Top: Transmission curve of the FPI versus absolute frequency, obtained with the narrowband laser internal reference by changing the laser frequency in 50 MHz steps over a range of 12 GHz (black dots). The best fit of Eq. 4.7 to the measurement is indicated by the red line. The resulting fit parameters are shown within the inset. Bottom: Residual between measurement and fit according to Eq. 3.6 in % of the peak intensity.

[17] The temperature and pressure from the radiosonde are interpolated to the altitude of the UFS of 2650 m.

Here, f_0 is the frequency at the intensity transmission maximum given in THz, R is the FPI mirror reflectivity and sigmaD the defect parameter given in THz. FSR is the free spectral range, determined as discussed in section 4.2.3 and set constant to be 10934 MHz within the fit procedure. From Fig. 4.12 it is obvious that the measured FPI transmission curve is accurately described by the model function, which is realized due to the consideration of mirror defects on the FPI (section 4.2.3). The residual between measurement and model (Fig. 4.12, bottom) shows a deviation of $\pm 3\,\%$ which symmetrically varies around zero, and thus, no remarkable systematic discrepancies between measurement and model remain.

After the FPI filter parameters are determined, Eq. 4.15 can be used to fit the measurement. The measured SRB line shapes for 8 different range bins, the best fit of Eq. 4.15 to them, and the residual between both according to Eq. 3.6 are plotted in Fig. 4.13, left.

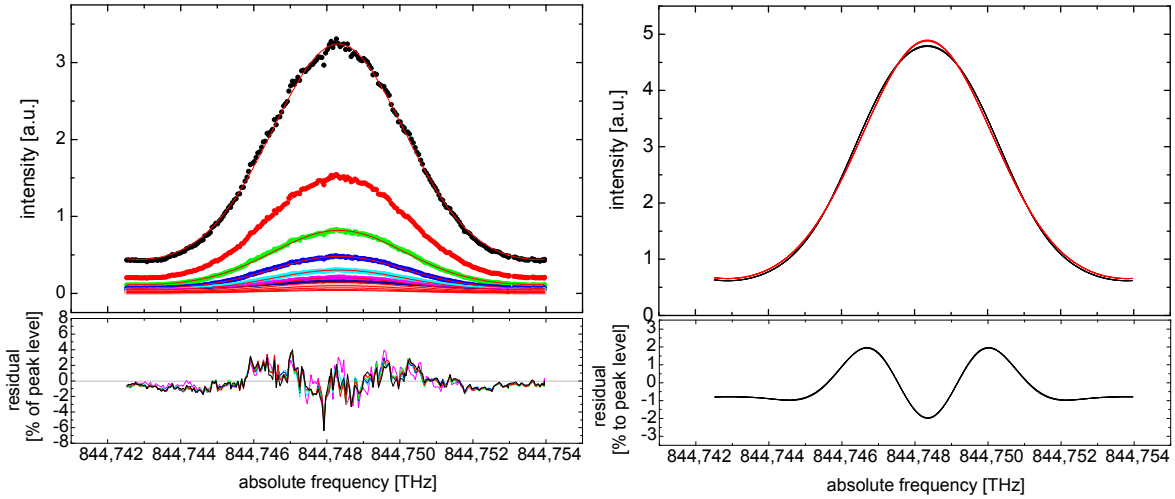

Figure 4.13: (left, top): Measured SRB line shapes for different distances (colored points) versus absolute frequency. The best fit of the analytical SRB line shape model according to Eq. 4.15 to the measurement is indicated by the red lines. (left, bottom): Residual between measurement and fit (according to Eq. 3.6). (right, top): Simulated SRB line shape, calculated by using the Tenti S6 model, temperature and pressure values present during measurement, and FPI filter parameter obtained from Fig. 4.12 (black). The best fit of the analytical SRB line shape model according to Eq. 4.15 to the simulated line shape is indicated in red (right, bottom): Residual between simulation and fit.

As the Gaussian approximation was used for deriving Eq. 4.15, the residual between the measured SRB line shapes and fit (Fig. 4.13, left, bottom) is assumed to represent a characteristic imprint which is due to the Brillouin scattering.

To verify this assumption and to further verify the ability of describing SRB line shapes in air by using the Tenti S6 model, an atmospheric reference signal is simulated by

convolving a Tenti S6 modeled SRB line shape (T = (262 ± 1.5) K, p = (722 ± 15) hPa, gas transport parameters of air (Table A.1) used as input) with the FPI transmission function according to Eq. 4.7 (filter parameters from measurement (Fig. 4.12) used as input). This simulated atmospheric reference signal (Fig. 4.13, right, top, black line) is fitted by Eq. 4.15 (Fig. 4.13, right, top, red line). The residual between simulated atmospheric reference signal and best fit (Fig. 4.13, right, bottom, black line) thereby certainly represents a characteristic imprint due to Brillouin scattering, as the Brillouin effect is considered in the Tenti S6 model but not in Eq. 4.15. The uncertainties in the measured temperature and pressure values are considered by calculating "worst-case" SRB line shapes as described in section 3.2.6. However, the difference between the worst-case line shapes is in the order of the line thickness (Fig. 4.13), and therefore, they are hardly distinguishable.

The next step of the analysis procedure is to compare both characteristic imprints (Fig. 4.13, bottom, left and right) to each other. As the residuals are normalized to the maximum intensity of the best-fit line shapes (Eq. 3.6) it is possible to directly realize this comparison as illustrated in Fig. 4.14.

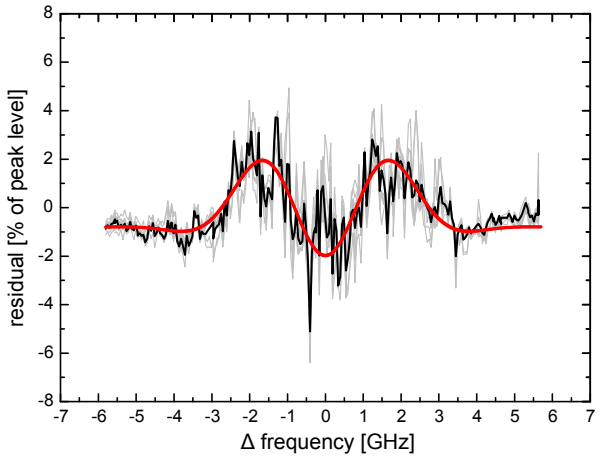

Figure 4.14: Comparison of the residuals between measured SRB line shapes and analytical model (Fig. 4.13, left, bottom) and simulated SRB line shape and analytical model (Fig. 4.13, right, bottom). The gray lines indicate the various residuals, calculated from the 8 range bins shown in Fig. 4.13, left, bottom, and the black line indicates their (unweighted) average. The red line represents the simulated residual as already depicted in Fig. 4.14, right, bottom.

In Fig. 4.14, the gray lines indicate the various residuals, calculated from the 8 range bins shown in Fig. 4.13, left, (2520 m - 7560 m from the UFS) and the black line indicates their (unweighted) average. The red line represents the simulated residual as already

illustrated in Fig. 4.14, right, bottom. It is clearly obvious that the characteristics of the averaged residual strictly follow the one of the simulated residual. This circumstance is a direct proof of the Brillouin effect within the atmosphere. In addition, it can be concluded that the SRB line shape of light scattered in air at atmospheric conditions is accurately described by the Tenti S6 model. Trace gases and noble gases in air do not have a remarkable influence on the SRB line shape. Furthermore, this result gives certainty that the Tenti S6 model can be used in case of a scattering angle of $\theta = 180°$. The positive maxima of both residuals are located at about ± 1700 MHz, which is close to the expected spectral location of the Brillouin peaks[18]. Furthermore, it is demonstrated that the transport coefficients of air derived for temperatures of 297 - 300 K (Table A.1) are applicable also for temperatures down to 263 K.

The above-mentioned points are confirmed by further SRBS measurements, performed during the BRAINS campaign. The residual comparison of SRBS measurements, performed on January 26 at 19:23 UTC and January 31st at 15:30 UTC, are shown in Fig. 4.15. It is obvious that the characteristics of the averaged residual strictly follow those of the simulated residual, too.

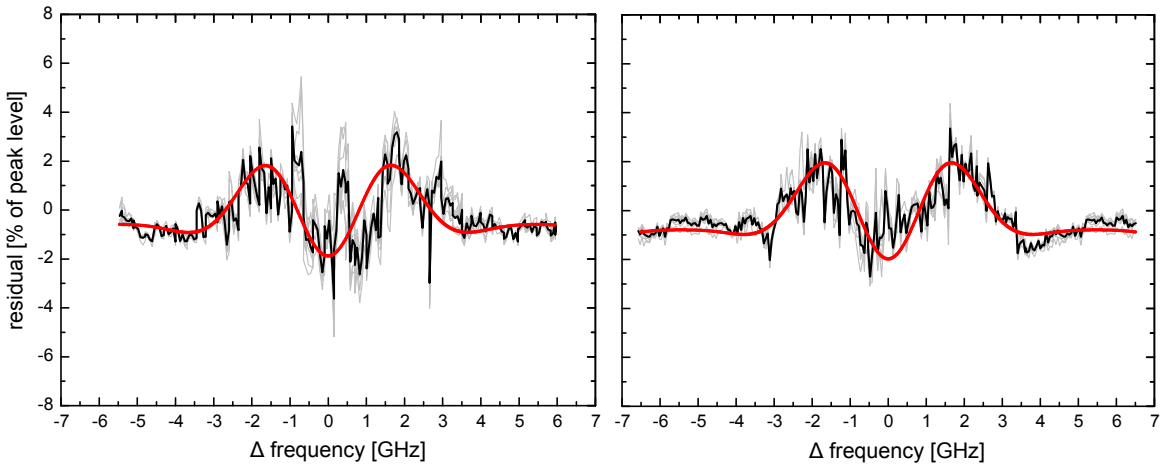

Figure 4.15: Comparison of the residuals between measured SRB line shapes and analytical model and simulated SRB line shape and analytical model according to Fig. 4.14. The shown measurements were performed on January 26 at 19:23 UTC (left) and January 31st at 15:30 UTC (right), respectively. The measurements were analyzed as demonstrated for the example of the SRBS measurement from January 31st at 17:00 UTC. Same labels as in Fig. 4.14.

[18] In the hydrodynamic regime, the spectral location of the Brillouin peaks can be calculated according to Eq. 2.12. With $c_s \approx 325$ m/s (at T = 262 K), $\lambda_i = 354.89$ nm, $\theta = 180°$, and $n \approx 1$, the Brillouin shift is 1831 MHz.

In Fig. 4.14 and Fig. 4.15 it can be seen that the signal to noise ratio of the averaged residual (black line) is improved compared to the one obtained from the single range bins (gray lines). However, it is worth mentioning that the performed atmospheric measurements can not be used for an accurate model verification or derivation of transport coefficients (e.g. bulk viscosity) as with the laboratory measurements under controlled conditions. This is mainly due to the quite large FPI resolution of about 1700 MHz used for atmospheric measurements, in comparison to 232 MHZ used for the laboratory measurements, which disallows to resolve small line shape changes with the atmospheric measurements. This gets more obvious by realizing that a temperature difference of ± 1.5 K and a pressure difference of ± 15 hPa cause a line shape difference which is almost indistinguishable Fig. 4.13, right. Furthermore, it is obvious that the obtained atmospheric signal is still noisy after averaging. This is due to systematic noise sources which do not cancel out by averaging. For instance, the field of view of the used telescope is 100μrad, and the divergence of the laser beam is about 90 μrad ($\pm 3\,\sigma$). If small atmospheric turbulences cause a jitter in the laser beam pointing in the order of more than $\pm 10\,\mu$rad, the laser beam is partly out of the field of view of the telescope, and the detected intensity systematically decreases.

Another issue related to the instrument model function (Eq. 4.7) is the reflection on the Fizeau interferometer (Fig. 4.4). Up to now this reflection is not included in the model function (Eq. 4.15), but results in a small modulation of the detected spectral transmission. This modulation arises from the spectral dependency of the Fizeau reflection and depends on the FSR of the Fizeau and the relative spectral position of the Fabry-Perot and Fizeau FSR's.

4.4 Summary

In the framework of the field campaign BRAINS (Brillouin scattering; atmospheric investigation on Schneefernerhaus), horizontal lidar measurements ($\lambda = 355$ nm, $\theta = 180°$) for the investigation of spontaneous Rayleigh-Brillouin scattering in the atmosphere were performed from the environmental research station Schneefernerhaus (UFS, 2650 m), located at Germany's highest mountain - the Zugspitze. The atmospheric temperatures and pressures during BRAINS were between 250 K - 272 K and 702 hPa - 736 hPa, respectively. A model function to describe the intensity transmission curve of the used Fabry-Perot interferometer was developed by considering mirror defects (section 4.2.3). The measured high-precision line shapes were compared to the Tenti S6 model using

a derived method within this thesis to compare the characteristic spectral signature of SRBS on simulated and measured spectra. It was the first time, that the influence of the Brillouin effect on the line shape was shown with lidar measurements in the atmosphere (section 4.2.5). As with the laboratory measurements, it is pointed out that measured SRB line shapes are accurately described by the Tenti S6 model also in backscattering geometry and real air composition. It is verified that trace and noble gases do not have any remarkable influence on the SRB line shape and that the transport coefficients of air derived for temperatures of 297 - 300 K (Table A.1) are applicable also for temperatures down to 263 K.

Chapter 5

Conclusion and outlook

Conclusion of this thesis

In the framework of this thesis, the first laboratory and atmospheric experiments on spontaneous Rayleigh-Brillouin scattering (SRBS) of ultraviolet light in air were performed. The measurements were used to investigate the spontaneous Rayleigh-Brillouin (SRB) line shape for relevant conditions in the atmosphere and to verify the Tenti S6 line shape model in terms of its applicability of describing the SRB line shape in air. The presented results are of relevance for the future space borne lidars on ADM-Aeolus (European Space Agency, 2008) and EarthCARE (European Space Agency, 2004).

Laboratory SRBS experiments in N_2, dry and humid air at temperatures of 295 to 301 K and pressures of 300 to 3500 hPa were performed at a wavelength of 366.5 nm and a scattering angle of 90°. For the first time, SRB line shapes of N_2 and air in the kinetic regime were compared to the Tenti S6 model, which is shown to describe the measured line shapes with small deviations. On a relative scale, these deviations are smaller than $\pm$ 4 % with respect to the peak intensity for all measured cases. For SRB line shapes obtained in air at atmospheric relevant pressures, the deviations are even smaller than $\pm$ 2 % (section 3.3.3, Fig. 3.10). These deviations can be due to experimental reasons, for example the undetected influence of stray light on the measurement (section 3.2.3), as well as due to shortcomings of the Tenti S6 model itself because of its approximative nature (section 2.3.2). Nevertheless, the $\pm$ 2 % deviation can be regarded as an upper boundary for discrepancies between Tenti S6 model and the actual SRB line shape as they are within the measurement uncertainty of the performed experiment. For the retrieval of direct-detection Doppler wind or high spectral resolution lidar data, this small deviation is assumed to cause only small errors, however, this statement has to be verified for each specific case as it depends on the respective setup configuration.

It was furthermore pointed out that the Gaussian approximation for SRB line shapes in air is unsatisfactory for pressures down to 300 hPa (section 3.3.3, Fig. 3.10). Due to the mathematical complexity of the Tenti S6 model, even today the Gaussian approximation is used in lidar applications in order to describe the SRB line shape (Ansmann et al., 2007; Hua et al., 2005; McGill et al., 1997a; Paffrath et al., 2009). However, as discussed in section 3.3.3, the deviation between measurement and Gaussian approximation is about ± 9 % for an ambient pressure of 1000 hPa (≈ sea level), and still about ± 3 % for an ambient pressure of 300 hPa (≈ 10 km above sea level). To be able to consider the Brillouin effect without high computational effort, an analytical line shape model which provides an adequate description of the SRB line shape in air was developed (appendix A 1). The derived analytical model is based on the superposition of three Gaussian functions and is fast to evaluate. The deviations between the analytical model and the Tenti S6 model were shown to be smaller than 0.85 % with respect to peak intensity for y values up to 1. Therefore, the newly developed model can be viewed as an analytical approximation of the Tenti S6 model.

In addition, it was demonstrated that the SRB line shapes obtained in air and N_2 under equal measurement conditions differ significantly (± 2 % with respect to peak intensity) at pressures of 2000 hPa and 300 hPa (section 3.3.2, Fig. 3.9), and that this difference can be described by the Tenti S6 model. In the past, several atmospheric researchers used the gas transport coefficients of N_2 as input parameters for their Tenti S6 model line shape calculation (Liu et al., 2009a; Shimizu et al., 1983; Young and Kattawar, 1983). However, the performed study has shown that the usage of the gas transport parameters of air is needed to obtain an adequate SRB line shape description. It is furthermore mentioned that between air and N_2 the main difference is arising from the difference in molecular mass. The other transport coefficients (shear viscosity, bulk viscosity and thermal conductivity) have, depending on gas temperature and pressure, a smaller influence on the line shape.

Moreover, it is shown that the precise value of the gas transport coefficients, needed as input for the Tenti S6 line shape model, is challenging to determine. This is especially the case for the bulk viscosity, as it has to be considered unknown at frequencies in the order of GHz. Based on the analysis of measured SRB line shapes using the Tenti S6 model, an alternative procedure for measuring the bulk viscosity of molecular gases in the GHz region was introduced (section 3.3.1). The bulk viscosity of N_2 and air was determined to be a factor of 1.6 and 1.3 larger compared to bulk viscosities determined for acoustic frequencies.

Furthermore, SRBS experiments on dry and humid air were performed to investigate the influence of water vapor on the SRB line shape. This investigation was of special importance for atmospheric applications that utilize the SRB line shape for their data retrieval, globally including tropical atmospheres with high humidity, like for instance the future space borne lidars on ADM-Aeolus and EarthCARE. It is pointed out that humidity has no significant influence on the SRB line shape, not even for high atmospheric water vapor contents of up to 3.6 vol. % (section 3.3.4, Fig. 3.11). Thus, this result confirms that the atmospheric moisture content does not have to be considered for SRB line shape calculation within atmospheric applications.

In order to use the obtained laboratory results for the data retrieval of atmospheric applications, they were further validated by measurements in the real atmosphere under real conditions. This was done in the framework of the field campaign BRAINS (BRillouin scattering - Atmospheric INvestigation on Schneefernerhaus), where horizontal lidar measurements ($\lambda = 355$ nm, $\theta = 180°$) were performed from the environmental research station Schneefernerhaus (UFS, 2650 m), located at Germany's highest mountain - the Zugspitze, to investigate SRBS in the atmosphere. The atmospheric temperatures and pressures during BRAINS, continuously measured, monitored and provided by the Deutschen Wetterdienst (DWD), were between 250 K - 272 K and 702 hPa - 736 hPa, respectively. The PM10 aerosol particle concentration was measured by the Umwelt Bundesamt (UBA) to be below 2 $\mu g/m^3$ during the performed SRBS experiments, and therefore, a disturbance to the measured SRB line shapes due to Mie scattering could be excluded. Thus, during the BRAINS campaign several SRBS measurements were performed under accurately observed atmospheric conditions. The obtained high-precision SRB line shapes were compared to the Tenti S6 model using a specifically derived method within this thesis to compare the characteristic spectral signature of SRBS on simulated and measured spectra. With this, the influence of Brillouin scattering on the SRB line shape was shown for the first time with lidar measurements in the atmosphere (section 4.2.5, Fig. 4.14 and Fig. 4.15). As with the laboratory measurements, it is pointed out that measured SRB line shapes in air are accurately described by the Tenti S6 model also in backscattering geometry ($\theta = 180°$) and real air composition. It was verified that trace and noble gases in air do not have a significant influence on the SRB line shape and that the transport coefficients of air derived for temperatures of 297 - 300 K (Table A.1) are also applicable for temperatures down to 263 K. The results of the BRAINS campaign confirm the applicability of the Tenti S6 model for describing SRB line shapes obtained in air at atmospheric conditions.

Outlook

The presented results are of primarily importance for atmospheric applications that utilize the characteristics of the SRB line shape for their data retrieval, as for instance the ESA space missions ADM-Aeolus and EarthCARE. By applying the presented results to their retrieval algorithms, the systematic error in the retrieved data is reduced and can now certainly be estimated.

Furthermore, the presented results are fundamental for the use of SRB scattering in lidar measurements with the objective of determining atmospheric temperature. Such a kind of temperature measurement could be performed by resolving the SRB line shape and relating it to the Tenti S6 model or its quasi analytical approximation which would even enable a fast least square fit procedure to the data (appendix A 1). Such measurements would provide a unique possibility of accurate atmospheric temperature determination over a large range. To improve the duration of such measurements in comparison to the SRB experiments discussed in chapter 3 and chapter 4, it would be possible to develop a fringe-imaging Fizeau interferometer for SRB line shape resolution. With it, neither the laser frequency nor the interferometer device has to be scanned for line shape resolution, and the measurement time is reduced as it solely depends on the noise level of the measurement itself.

Despite the numerous important results concerning SRB scattering in air, there are still some open issues dealing with the understanding of SRB line shapes. However, these issues are more related to fundamental research.

The air temperature in conventional experiments that utilize the characteristics of the SRB line shape ranges from 220 K to 300 K in atmospheric applications such as lidar measurements to several hundred Kelvin in combustion measurements. To consider this wide temperature range, there is a need to investigate the temperature dependence of gas transport parameters of air, serving as input for the Tenti S6 model. In case of the bulk viscosity, it is furthermore necessary to investigate its frequency dependency (section 3.3.1).

For SRB experimental setups or lidar instruments that use polarization-sensitive detectors, it is necessary to investigate the polarization characteristics of molecular scattered light. As shown in section 2.2, the SRB line shape is mainly polarized but contains a

small contribution of depolarized light due to the rotational Raman Q-branch ($\approx 0.64\,\%$ of the total intensity of the SRB line shape in N_2). And, as shown in section 2.3.2, this contribution is not considered by the Tenti S6 model. Thus, the influence of the rotational Raman Q-branch contribution has to be investigated by analyzing both the polarized and depolarized part of the SRB line shape concerning their intensity and their spectral line shape. Such a measurement could be performed using the experimental setup discussed in chapter 3 (Fig. 3.1), extended with polarization optics.

In chapter 3.3, it is shown that the Tenti S6 model, which refers to a single-species molecular gas, can be applied to air by using effective transport coefficients of air, and the molecular mass of a fictive gas mixture of N_2 and O_2. However, this approach is not based on the microscopically correct description of the collision between two different molecules. The Tenti S6 model is a kinetic model which involves collisions between molecules expressed in a single collision integral. As gas mixtures contain different molecules with different collision cross sections, a better line shape model should explicitly involve those details. A model for gases consisting of hard sphere atoms was recently developed by Bonatto and Marques (2005), and has shown to provide a better fit to spectra of noble gas mixtures than a hydrodynamic model. However, hard-sphere models consider no internal degrees of freedom, and thus, they can not be used for the description of mixtures of molecular gases.

In section 2.3.2 it is additionally mentioned that the Tenti S6 model does not account for molecules with degenerate internal states, as they are not considered in the Wang-Chang-Uhlenbeck equation. Recently, a line shape (Q9 model) model that takes these degenerate states into account was theoretically developed by Zheng (2007). A comparison between Q9 and Tenti S6 model showed no significant differences for atmospheric relevant conditions with y parameters up to 0.5, but showed differences for y values larger 1.5. Nevertheless, up to now no comparison of the Q9 model to experimental data has been performed or rather published. To verify if the Q9 model possibly provides a better description of SRB line shapes than the Tenti S6 model, the data of the performed experiments (chapter 3.3) could be used. However, the Q9 model code is owned by the Michigan Aerospace Corporation and is not publically available yet.

Bibliography

Ansmann, A., Wandinger, U., Le Rille, O., Lajas, D., and Straume, A. (2007). Particle backscatter and extinction profiling with the spaceborne high-spectral-resolution Doppler lidar ALADIN: methodology and simulations. *Appl. Opt.*, 46(26):6606–6622.

Ansmann, A., Wandinger, U., Riebesell, M., Weitkamp, C., and Michaelis, W. (1992). Independent measurement of extinction and backscatter profiles in cirrus clouds by using a combined raman elastic-backscatter lidar. *Appl. Opt.*, 31(33):7113–7113.

Bass, H., Sutherland, L., Piercy, J., and Evans, L. (1984). Absorption of sound by the atmosphere. In *Physical acoustics: Principles and methods. Orlando, FL, Academic Press, Inc.*, volume 17, pages 145–232.

Bass, H. E., Sutherland, L. C., and Zuckerwar, A. J. (1990). Atmospheric absorption of sound - Update. *J. Acoust. Soc. Am*, 88:2019–2021.

Bass, H. E., Sutherland, L. C., Zuckerwar, A. J., Blackstock, D. T., and Hester, D. M. (1995). Atmospheric absorption of sound: Further developments. *J. Acoust. Soc. Am*, 97:680–683.

Bass, H. E., Sutherland, L. C., Zuckerwar, A. J., Blackstock, D. T., and Hester, D. M. (1996). Erratum: Atmospheric absorption of sound: Further developments [J. Acoust. Soc. Am. 97, 680-683 (1995)]. *J. Acoust. Soc. Am*, 99:1259.

Bayer-Helms, F. (1963). Analyse von Linienprofilen. I. Grundlagen und Messeinrichtungen. *Z. Angew. Phys.*, 15:330–338.

Behrendt, A., Nakamura, T., Onishi, M., Baumgart, R., and Tsuda, T. (2002). Combined Raman lidar for the measurement of atmospheric temperature, water vapor, particle extinction coefficient, and particle backscatter coefficient. *Appl. Opt.*, 41(36):7657–7666.

Bhatnagar, G., Singh, K., and Gupta, B. (1974). Transmission profile of a Fabry-Perot interferometer suffering from asymmetric surface defects. *Nouvelle Revue d'Optique*, 5:237–240.

Boley, C., Desai, R., and Tenti, G. (1972). Kinetic models and Brillouin scattering in a molecular gas. *Can. J. Phys.*, 50(18):2158–2173.

Bonatto, J. R. and Marques, W. (2005). Kinetic model analysis of light scattering in binary mixtures of monatomic ideal gases. *J. Stat. Mech.*, 9:09014.

Boon, J. and Yip, S. (1991). *Molecular hydrodynamics*. Dover Dover Pub. Inc. NewYork.

Brillouin, L. (1922). Diffusion de la lumière et des rayons X par un corps transparent homogène, influence de l'agitation thermique. *Ann. Phys*, 17:88–122.

Browell, E., Ismail, S., and Grant, W. (1998). Differential absorption lidar (DIAL) measurements from air and space. *Appl. Phys. B: Lasers and Optics*, 67(4):399–410.

Cabannes, J. and Rocard, Y. (1929). La théorie électromagnétique de Maxwell-Lorentz et la diffusion moléculaire de la lumière. *J. Phys-Paris*, 2.

Cézard, N., Dolfi-Bouteyre, A., Huignard, J.-P., and Flamant, P. H. (2009). Performance evaluation of a dual fringe-imaging Michelson interferometer for air parameter measurements with a 355 nm Rayleigh-Mie lidar. *Appl. Opt.*, 48(12):2321–2332.

Chabbal, R. (1954). Recherche des meilleures conditions d'utilisation d'un spectromètre photoélectrique Fabry-Perot. *J. Rech. Centre Nat. Rech. Sci. Lab. Bellevue (Paris)*, 24:138.

Cruz, L. S. and Cruz, F. C. (2007). External power-enhancement cavity versus intracavity frequency doubling of Ti:sapphire lasers using BIBO. *Opt. Express*, 15(19):11913–11921.

Curtiss, C. (1967). Transport Phenomena in Gases. *Annu. Rev. Phys. Chem.*, 18(1):125–151.

Dabas, A., Denneulin, M., Flamant, P., Loth, C., Garnier, A., and Dolfi-Bouteyre, A. (2008). Correcting winds measured with a Rayleigh Doppler lidar from pressure and temperature effects. *Tellus A*, 60(2):206–215.

Damzen, M. (2003). *Stimulated brillouin scattering: fundamentals and applications.* Taylor & Francis.

Donovan, D., Bird, J., Whiteway, J., Duck, T., Pal, S., and Carswell, A. (1995). Lidar observations of stratospheric ozone and aerosol above the Canadian high arctic during the 1994-95 winter. *Geophys. Res. Lett.*, 22(24):3489–3492.

Durand, Y., Chinal, E., Endemann, M., Meynart, R., Reitebuch, O., and Treichel, R. (2006). ALADIN airborne demonstrator: a Doppler Wind lidar to prepare ESA's ADM-Aeolus Explorer mission. In *Proceedings of SPIE*, volume 6296, page 62961D.

Durand, Y., Meynart, R., Endemann, M., Chinal, E., Morancais, D., Schröder, T., and Reitebuch, O. (2005). Manufacturing of an airborne demonstrator of ALADIN: The direct detection Doppler wind lidar for ADM-Aeolus. In *Proceedings of SPIE*, volume 5984, page 598401.

Einstein, A. (1910). Theorie der Opaleszenz von homogenen Flüssigkeiten und Flüssigkeitsgemischen in der Nähe des kritischen Zustandes. *Ann. Phys*, 338(16):1275–1298.

Elliott, G., Glumac, N., and Carter, C. (2001). Molecular filtered Rayleigh scattering applied to combustion. *Meas. Sci. Technol.*, 12:452.

Eloranta, E. (2005). *Lidar*, chapter 5 - High spectral resolution lidar, pages 143–163. Springer.

Emanuel, G. (1990). Bulk viscosity of a dilute polyatomic gas. *Phys.Fluids*, 2:2252–2254.

Esselborn, M., Wirth, M., Fix, A., Tesche, M., and Ehret, G. (2008). Airborne high spectral resolution lidar for measuring aerosol extinction and backscatter coefficients. *Appl. Opt.*, 47(3):346–358.

European Space Agency (European Space Research and Technology Centre, 2004). Earth Clouds, Aerosols, and Radiation Explorer. *science report, ESA-SP-1279(1).*

European Space Agency (European Space Research and Technology Centre, 2008). ADM-Aeolus. *science report, ESA-SP-1311.*

Fabelinskii, I. (1968). *Molecular Light Scattering.* Plenum Press, New York.

Figgins, R. (1971). Inelastic light scattering in liquids: Brillouin scattering. *Contemp. Phys.*, 12(3):283–297.

Fiocco, G. and DeWolf, J. B. (1968). Frequency Spectrum of Laser Echoes from Atmospheric Constituents and Determination of the Aerosol Content of Air. *J. Atmos. Sci.*, 25(3):488–496.

Flamant, P., Loth, C., Dabas, A., Denneulin, M., and Dolfi-Bouteyre, A. (2005). ILIAD: Impact of Line Shape on Wind Measurements and Correction Methods. *ESA Contract Final Report 1833404/NL/MM, ESTEC*.

Flesia, C. and Korb, C. L. (1998). Double-edge molecular technique for Doppler lidar wind measurement. In *Proceedings of SPIE*, volume 3504, pages 587–592.

Forkey, J. N. (1996). *Development and Demonstration of Filtered Rayleigh Scattering: a Laser Based Flow Diagnostic for Planar Measurement of Velocity, Temperature and Pressure*. PhD thesis, Princeton University.

Fry, E., Hu, Q., and Li, X. (1991). Single frequency operation of an injection-seeded Nd: YAG laser in high noise and vibration environments. *Appl. Opt.*, 30(9):1015–1017.

Gentry, B. M., Chen, H., and Li, S. X. (2000). Wind measurements with 355-nm molecular Doppler lidar. *Opt. Lett.*, 25:1231–1233.

Ghaem-Maghami, V. and May, A. D. (1980). Rayleigh-Brillouin spectrum of compressed He, Ne, and Ar. I. Scaling. *Phys. Rev. A*, 22:692–697.

Goldsmith, J. E. M., Blair, F. H., Bisson, S. E., and Turner, D. D. (1998). Turn-key raman lidar for profiling atmospheric water vapor, clouds, and aerosols. *Appl. Opt.*, 37(21):4979–4990.

Gombosi, T. (1994). *Gaskinetic theory*. Cambridge University Press.

Graves, R. and Argrow, B. (1999). Bulk viscosity: past to present. *J. Thermophys. Heat Transfer*, 13(3):337–342.

Greytak, T. J. and Benedek, G. B. (1966). Spectrum of Light Scattered from Thermal Fluctuations in Gases. *Phys. Rev. Lett.*, 17(4):179–182.

Grinstead, J. and Barker, P. (2000). Coherent Rayleigh scattering. *Phys. Rev. Lett.*, 85(6):1222–1225.

Gross, E. (1930). Change of Wavelength of Light due to Elastic Heat Waves at Scattering in Liquids. *Nature*, 126(3171):201–202.

Gustavsson, J. (2000). Molecular velocity distribution in air. *http://plaza.ufl.edu/jgu/public_html/UF/AirMolVelDistr.pdf*.

Hair, J. W., Caldwell, L. M., Krueger, D. A., and She, C.-Y. (2001). High-Spectral-Resolution Lidar with Iodine-Vapor Filters: Measurement of Atmospheric-State and Aerosol Profiles. *Appl. Opt.*, 40(30):5280–5294.

Hair, J. W., Hostetler, C. A., Cook, A. L., Harper, D. B., Ferrare, R. A., Mack, T. L., Welch, W., Izquierdo, L. R., and Hovis, F. E. (2008). Airborne High Spectral Resolution Lidar for profiling aerosol optical properties. *Appl. Opt.*, 47(36):6734–6752.

Hänel, D. (2004). *Molekulare Gasdynamik*. Springer Berlin, Heidelberg.

Hänsch, T. and Couillaud, B. (1980). Laser frequency stabilization by polarization spectroscopy of a reflecting reference cavity. *Opt. commun.*, 35(3):441–444.

Hara, E. H., May, A. D., and Knaap, H. F. P. (1971). Rayleigh-Brillouin scattering in compressed H_2, D_2 and HD. *Can. J. Phys.*, 49:420–431.

Hays, P. and Roble, R. (1971). A technique for recovering Doppler line profiles from Fabry-Perot interferometer fringes of very low intensity. *Appl. Opt.*, 10(1):193–200.

Henderson, S., Yuen, E., and Fry, E. (1986). Fast resonance-detection technique for single-frequency operation of injection-seeded Nd: YAG lasers. *Opt. Lett.*, 11(11):715–717.

Hernandez, G. (1966). Analytical description of a Fabry-Perot photoelectric spectrometer. *Appl. Opt.*, 5(11):1745–1748.

Hernandez, G. (1986). *Fabry-Perot Interferometers*. Cambridge University Press.

Herzfeld, K., Litovitz, T., and Yeager, E. (1959). Absorption and dispersion of ultrasonic waves. *J. Electrochem. Soc.*, 106:314C.

Hoel, P., Port, S., and Stone, C. (1962). *Introduction to mathematical statistics*, volume 6. Wiley New York.

Hua, D., Uchida, M., and Kobayashi, T. (2005). Ultraviolet Rayleigh-Mie lidar for daytime-temperature profiling of the troposphere. *Appl. Opt.*, 44(7):1315–1322.

Kittel, C. and McEuen, P. (1986). *Introduction to solid state physics*, volume 4. Wiley New York.

Knaap, H. and Lallemand, P. (1975). Light Scattering by Gases. *Annu. Rev. Phys. Chem.*, 26(1):59–82.

Krebs, K. and Sauer, A. (1953). Über die Intensitätsverteilung von Spektrallinien im Pérot-Fabry-Interferometer. *Ann. Phys.*, 448(6-8):359–368.

Landau, L. and Placzek, G. (1934). Structure of the undisplaced scattering line. *Phys. Z. Sowiet. Un*, 5:172.

Lao, Q. H., Schoen, P. E., and Chu, B. (1976). Rayleigh-Brillouin scattering of gases with internal relaxation. *J. Chem. Phys.*, 64:3547–3555.

Letamendia, L., Chabrat, J., Nouchi, G., Rouch, J., Vaucamps, C., and Chen, S. (1981). Light-scattering studies of moderately dense gas mixtures: Hydrodynamic regime. *Phys. Rev. A*, 24(3):1574–1590.

Letamendia, L., Joubert, P., Chabrat, J. P., Rouch, J., Vaucamps, C., Boley, C. D., Yip, S., and Chen, S.-H. (1982). Light-scattering studies of moderately dense gases. II. Nonhydrodynamic regime. *Phys. Rev. A*, 25:481–488.

Liu, B.-Y., Esselborn, M., Wirth, M., Fix, A., Bi, D.-C., and Ehret, G. (2009a). Influence of molecular scattering models on aerosol optical properties measured by high spectral resolution lidar. *Appl. Opt.*, 48(27):5143–5154.

Liu, Z.-S., Bi, D.-C., quan Song, X., Xia, J.-B., zhong Li, R., jun Wang, Z., and She, C.-Y. (2009b). Iodine-filter-based high spectral resolution lidar for atmospheric temperature measurements. *Opt. Lett.*, 34(18):2712–2714.

Lock, J. A., Seasholtz, R. G., and John, W. T. (1992). Rayleigh-Brillouin scattering to determine one-dimensional temperature and number density profiles of a gas flow field. *Appl. Opt.*, 31(15):2839–2848.

Long, D. (2002). *The Raman effect: a unified treatment of the theory of Raman scattering by molecules*. John Wiley & Sons Inc.

Maiman, T. (1960). Stimulated optical radiation in ruby. *Nature*, 187:493–494.

Mandelstam, L. I. (1926). Light Scattering by Inhomogeneous Media. *Zh. Russ. Fiz-Khim. Ova*, 58:381.

McGill, M., Skinner, W., and Irgang, T. (1997a). Analysis techniques for the recovery of winds and backscatter coefficients from a multiple-channel incoherent Doppler lidar. *Appl. Opt.*, 36(6):1253–1268.

McGill, M., Skinner, W., and Irgang, T. (1997b). Validation of wind profiles measured with incoherent Doppler lidar. *Appl. Opt.*, 36(9):1928–1932.

Meador, W., Miner, G., and Townsend, L. (1996). Bulk viscosity as a relaxation parameter: Fact or fiction? *Phys. Fluids*, 8:258.

Measures, R. M. (1984). *Laser remote sensing: fundamentals and applications*. Wiley.

Meijer, A., de Wijn, A., Peters, M., Dam, N., and van de Water, W. (2010). Coherent Rayleigh–Brillouin scattering measurements of bulk viscosity of polar and nonpolar gases, and kinetic theory. *J. Chem. Phys.*, 133:164315.

Miles, R. B., Lempert, W. R., and Forkey, J. N. (2001). Laser Rayleigh scattering. *Meas. Sci. Technol.*, 12(5):R33–R51.

Mountain, R. (1966). Spectral distribution of scattered light in a simple fluid. *Rev. Mod. Phys.*, 38(1):205–214.

Nicklaus, K., Morasch, V., Hoefer, M., Luttmann, J., Vierkötter, M., Ostermeyer, M., Höffner, J., Lemmerz, C., and Hoffmann, D. (2007). Frequency stabilization of Q-switched Nd: YAG oscillators for airborne and spaceborne lidar systems. In *Proceedings of SPIE*, volume 6451, page 64511L.

Paffrath, U. (2006). *Performance assessment of the Aeolus Doppler wind lidar prototype*. PhD thesis, Technical university of Munich.

Paffrath, U., Lemmerz, C., Reitebuch, O., Witschas, B., Nikolaus, I., and Freudenthaler, V. (2009). The Airborne Demonstrator for the Direct-Detection Doppler Wind Lidar ALADIN on ADM-Aeolus. Part II: Simulations and Rayleigh Receiver Radiometric Performance. *J. Atmos. Oceanic Technol.*, 26:2516–2530.

Palik, E., Boukari, H., and Gammon, R. (1996). Experimental study of the effect of surface defects on the finesse and contrast of a Fabry-Perot interferometer. *Appl. Opt.*, 35(1):38–50.

Pan, X., Shneider, M., and Miles, R. (2005). Power spectrum of coherent Rayleigh-Brillouin scattering in carbon dioxide. *Phys. Rev. A*, 71(4):45801.

Pan, X., Shneider, M., Zhang, Z., and Miles, R. (2004a). Bulk Viscosity Measurements Using Coherent Rayleigh-Brillouin Scattering. *The 42nd Aerospace Sciences Meeting and Exhibit Conference, AIAA-2004-0017.*

Pan, X., Shneider, M. N., and Miles, R. B. (2002). Coherent Rayleigh-Brillouin Scattering. *Phys. Rev. Lett.*, 89(18):183001.

Pan, X., Shneider, M. N., and Miles, R. B. (2004b). Coherent Rayleigh-Brillouin scattering in molecular gases. *Phys. Rev. A*, 69(3):033814.

Prangsma, G., Alberga, A., and Beenakker, J. (1973). Ultrasonic determination of the volume viscosity of N_2, CO, CH_4 and CD_4 between 77 and 300 K. *Physica*, 64(2):278–288.

Press, W. (2007). *Numerical recipes: the art of scientific computing.* Cambridge University Press.

Rah, K. and Eu, B. (2001). Density and temperature dependence of the bulk viscosity of molecular liquids: Carbon dioxide and nitrogen. *J. Chem. Phys.*, 114:10436–10447.

Raman, C. and Krishnan, K. (1928). A new type of secondary radiation. *Nature*, 121(3048):501.

Rayleigh, L. (1871). On the scattering of light by small particles. *Philos. Mag*, 41:447–454.

Rayleigh, L. (1881). On the electromagnetic theory of light. *Philos. Mag*, 12:81–101.

Rayleigh, L. (1899). On the transmission of light through an atmosphere containing small particles in suspension, and on the origin of the blue of the sky. *Philos. Mag*, 47(375):132.

Rayleigh, L. (1918). On the scattering of light by a cloud of similar small particles of any shape and oriented at random. *Philos. Mag*, 35:373–381.

Reichardt, J. (2000). Error analysis of raman differential absorption lidar ozone measurements in ice clouds. *Appl. Opt.*, 39(33):6058–6071.

Reitebuch, O., Chinal, E., Durand, Y., Endemann, M., Meynart, R., Morancais, D., and Paffrath, U. (2004). Development of an airborne demonstrator for ADM-AEOLUS and campaign activities. *Proceedings of the 22nd International Laser Radar Conference, ESA SP-561 (European Space Agency, 2004)*, pages 1007–1010.

Reitebuch, O., Lemmerz, C., Nagel, E., Paffrath, U., Durand, Y., Endemann, M., Fabre, F., and Chaloupy, M. (2009). The Airborne Demonstrator for the Direct-Detection Doppler Wind Lidar ALADIN on ADM-Aeolus. Part I: Instrument Design and Comparison to Satellite Instrument. *J. Atmos. Oceanic Technol.*, 26:2501–2515.

Rossing, T. (2007). *Springer handbook of acoustics*. Springer Verlag.

Rye, B. J. (1998). Molecular Backscatter Heterodyne Lidar: A Computational Evaluation. *Appl. Opt.*, 37(27):6321–6328.

Sandoval, R. P. and Armstrong, R. L. (1976). Rayleigh-Brillouin spectra in molecular nitrogen. *Phys. Rev. A*, 13:752–757.

Schmitt, R. and Rahn, L. (1986). Diode-laser-pumped Nd: YAG laser injection seeding system. *Appl. Opt.*, 25(5):629–633.

Schröder, T., Lemmerz, C., Reitebuch, O., Wirth, M., Wührer, C., and Treichel, R. (2007). Frequency jitter and spectral width of an injection-seeded Q-switched Nd: YAG laser for a Doppler wind lidar. *Appl. Phys. B: Lasers and Optics*, 87(3):437–444.

Seasholtz, R., Buggele, A., and Reeder, M. (1997). Flow measurements based on Rayleigh scattering and Fabry-Perot interferometer. *Optics and Lasers in Engineering*, 27(6):543–570.

She, C., Herring, G., Moosmüller, H., and Lee, S. (1983). Stimulated Rayleigh-Brillouin gain spectroscopy in pure gases. *Phys. Rev. Lett.*, 51(18):1648–1651.

She, C. Y., Herring, G. C., Moosmüller, H., and Lee, S. A. (1985). Stimulated rayleigh-brillouin gain spectroscopy. *Phys. Rev. A*, 31(6):3733–3740.

Shimizu, H., Lee, S. A., and She, C. Y. (1983). High spectral resolution lidar system with atomic blocking filters for measuring atmospheric parameters. *Appl. Opt.*, 22(9):1373–1381.

Shimizu, H., Noguchi, K., and She, C.-Y. (1986). Atmospheric temperature measurement by a high spectral resolution lidar. *Appl. Opt.*, 25(9):1460–1466.

Snider, R. (1960). Quantum-Mechanical Modified Boltzmann Equation for Degenerate Internal States. *J. Chem. Phys.*, 32:1051.

Stoffelen, A., Pailleux, J., Källén, E., Vaughan, J. M., Isaksen, L., Flamant, P., Wergen, W., Andersson, E., Schyberg, H., Culoma, A., Meynart, R., Endemann, M., and Ingmann, P. (2005). The Atmospheric Dynamics Mission for global wind field measurement. *Bull. Amer. Meteor. Soc.*, 86(1):73–87.

Sugawara, A. and Yip, S. (1967). Kinetic Model Analysis of Light Scattering by Molecular Gases. *Phys. Fluids*, 10:1911–1921.

Tan, D. G. H., Andersson, E., de Kloe, J., Marseille, G., Stoffelen, A., Poli, P., Denneulin, M., Dabas, A., Huber, D., Reitebuch, O., Flamant, P., Le Rille, O., and Nett, H. (2008). The ADM-Aeolus wind retrieval algorithms. *Tellus Series A*, 60:191–205.

Taxman, N. (1958). Classical Theory of Transport Phenomena in Dilute Polyatomic Gases. *Phys. Rev.*, 110:1235–1239.

Tenti, G., Boley, C. D., and Desai, R. C. (1974). On the kinetic model description of Rayleigh-Brillouin scattering from molecular gases. *Can. J. Phys.*, 52(4):285–290.

Tesche, M., Ansmann, A., Müller, D., Althausen, D., Mattis, I., Heese, B., Freudenthaler, V., Wiegner, M., Esselborn, M., Pisani, G., et al. (2009). Vertical profiling of Saharan dust with Raman lidars and airborne HSRL in southern Morocco during SAMUM. *Tellus B*, 61(1):144–164.

US Standard Atmosphere (1976). US Standard Atmosphere, 1976. *US Government Printing Office, Washington, DC. http://www.pdas.com/refs/us76.pdf*.

Van Hove, L. (1954). Correlations in space and time and Born approximation scattering in systems of interacting particles. *Phys. Rev.*, 95(1):249–262.

Vaughan, J. M. (1989). *The Fabry-Perot Interferometer*. Adam Hilger.

Vieitez, M., Ubachs, W., van Duijn, E.J. Dam, N., Meijer, A., van de Water, W., de Kloe, J., Stoffelen, A., and Aben, I. (European Space Research and Technology Centre, 2010a). A spontaneous Rayleigh-Brillouin scattering experiment for the characterization of atmospheric lidar backscatter. *final report, ESA contract 21396/07/NL/HE*, page 209.

Vieitez, M., van Duijn, E., Ubachs, W., Witschas, B., Meijer, A., de Wijn, A., Dam, N., and van de Water, W. (2010b). Coherent and spontaneous Rayleigh-Brillouin scattering in atomic and molecular gases and gas mixtures. *Phys. Rev. A*, 82(4):43836.

Vogelmann, H. and Trickl, T. (2008). Wide-range sounding of free-tropospheric water vapor with a differential-absorption lidar (DIAL) at a high-altitude station. *Appl. Opt.*, 47(12):2116–2132.

Wakeham, W. (1986). Transport properties of polyatomic gases. *Int. J. Thermophys.*, 7(1):1–15.

Waldmann, L. (1957). Die BOLTZMANN-Gleichung für Gase mit rotierenden Molekülen. *Zeitschrift Naturforschung Teil A*, 12:660.

Wandinger, U. (2005). *Lidar*, chapter 9 - Raman lidar, pages 241–271. Springer.

Wang Chang, C., Uhlenbeck, G., and De Boer, J. (1964). The heat conductivity and viscosity of polyatomic gases. *Studies in Statistical Mechanics*, 2:243–268.

Weast, R. and Company, C. R. (1973). *CRC handbook of chemistry and physics*. CRC press Boca Raton, FL.

Weinberg, M., Kapral, R., and Desai, R. (1973). Light-Scattering Experiments and Generalized Transport Coefficients. *Phys. Rev. A*, 7(4):1413–1419.

Weitkamp, C. (2005). *Lidar: range-resolved optical remote sensing of the atmosphere*. Springer Verlag.

Wilksch, P. (1985). Instrument function of the Fabry-Perot spectrometer. *Appl. Opt.*, 24(10):1502–1511.

Witschas, B. (2007). Characterisation of beam profile and frequency stability of an injection-seeded Nd: YAG laser for a Doppler wind lidar system. Master's thesis, Department of Technical Physics, University of Applied Sciences Munich.

Witschas, B. (2011). Analytical model for Rayleigh–Brillouin line shapes in air. *Appl. Opt.*, 50(3):267–270.

Witschas, B., Vieitez, M. O., van Duijn, E.-J., Reitebuch, O., van de Water, W., and Ubachs, W. (2010). Spontaneous Rayleigh–Brillouin scattering of ultraviolet light in nitrogen, dry air, and moist air. *Appl. Opt.*, 49(22):4217–4227.

Young, A. (1980). On the Rayleigh-Scattering Optical Depth of the Atmosphere. *J. Appl. Meteorol.*, 20:328–329.

Young, A. T. (1981). Rayleigh scattering. *Appl. Opt.*, 20(4):533–535.

Young, A. T. and Kattawar, G. W. (1983). Rayleigh-scattering line profiles. *Appl. Opt.*, 22(23):3668–3670.

Zheng, Q. (2004). *On the Rayleigh-Brillouin scattering in air*. PhD thesis, University of New Hampshire.

Zheng, Q. (2007). Model for polarized and depolarized Rayleigh Brillouin scattering spectra in molecular gases. *Appl. Opt.*, 15:14257–14265.

Appendix

A 1 Analytical model for Rayleigh-Brillouin line shapes in air

In the following, an analytical model for describing spontaneous Rayleigh-Brillouin (SRB) line shapes is developed. The entire model derivation and a comparison to the Tenti S6 model can be found in Witschas (2011).

The mathematically complex, non-analytical closed form of the Tenti S6 model (section 2.3.1) makes the application to measured data quite circuitous. For example, deriving the temperature from the measured SRB line shape can only be performed by complicated numerical fit procedures, instead of using ordinary least square fit routines as it is common for analytical functions. For the wind retrieval in the frame of the ADM-Aeolus mission, extensive look-up tables for SRB line shapes at different y values has to be calculated. In addition, further processing of the Tenti S6 modeled spectra, e.g. convolution with the instrument function of the measurement system is only numerically possible. To overcome this situation, an easy processable analytical representation of the Tenti S6 model is empirically derived for SRB spectra in air.
The basic concept of the analytical model is to describe the SRB spectrum $\mathcal{S}(x, y)$ in the style of the hydrodynamic regime (Fig. 2.3, section 2.1.3) by superposing a central Gaussian line with standard deviation σ_R and integrated intensity $\mathcal{A}$ to represent the Rayleigh peak, and two shifted Gaussian lines at $\pm x_B$ with standard deviation σ_B and integrated intensity $(1-\mathcal{A})/2$ to represent the Brillouin doublet (see Fig. A.1). With $0 \leq \mathcal{A} \leq 1$, the analytically calculated spectrum $\mathcal{S}(x, y)$ is normalized to unity integrated intensity and can be written as:

$$\begin{aligned} \mathcal{S}(x,y) \;=\; & \frac{1}{\sqrt{2\,\pi}\,\sigma_R}\,\mathcal{A}\,\exp\left[-\frac{1}{2}\left(\frac{x}{\sigma_R}\right)^2\right] \\ & + \frac{1-\mathcal{A}}{2\,\sqrt{2\,\pi}\,\sigma_B}\,\exp\left[-\frac{1}{2}\left(\frac{x+x_B}{\sigma_B}\right)^2\right] \\ & + \frac{1-\mathcal{A}}{2\,\sqrt{2\,\pi}\,\sigma_B}\,\exp\left[-\frac{1}{2}\left(\frac{x-x_B}{\sigma_B}\right)^2\right]. \end{aligned} \tag{A.1}$$

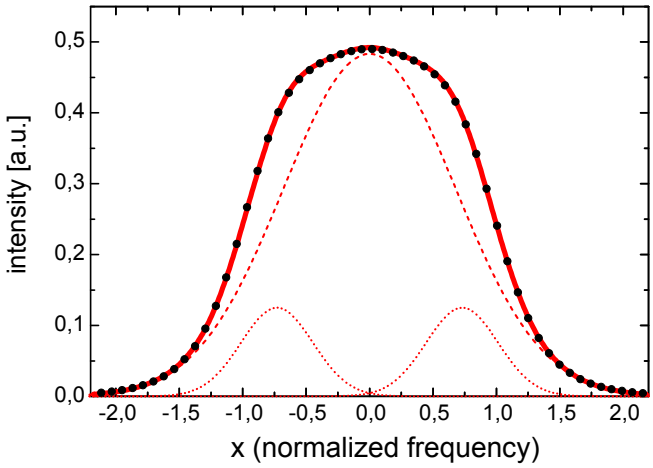

Figure A.1: Spectrum of SRB scattered light in air for $y = 0.652$ according to the Tenti S6 model (Black dots). The red line represents the superposition of a central Gaussian line with standard deviation $\sigma_R = 0.68$ and integrated intensity $\mathcal{A} = 0.82$ (dashed red line) and two shifted Gaussian lines at $\pm x_B = 0.73$ with standard deviation $\sigma_B = 0.28$ and integrated intensity $(1 - \mathcal{A})/2 = 0.09$ (doted red lines). The Tenti modeled line shape as well as the superposition of the Gaussians is normalized to yield unity integrated intensity.

In contrast to similar approaches as introduced by Gustavsson (2000) and Zheng (2004), the parameters $\mathcal{A}$, σ_R, σ_B and x_B are now determined solely empirically to obtain best accordance between $\mathcal{S}(x, y)$ and the Tenti S6 model.

Actually, the S6 spectrum depends on 4 dimensionless parameter (Eq. 2.23). However, for atmospheric applications, z and f can be approximated to be constant with respect to temperature (Rossing, 2007; Shimizu et al., 1986), although there is a strong demand to prove this approximation with measurements. Taking the transport coefficients of air ($M = 4.789 \cdot 10^{-26}\,\mathrm{kg}$, $\eta = 1.846 \cdot 10^{-5}\,\mathrm{Pa\,m^{-1}\,s^{-1}}$, $\eta_B = 1.4 \cdot 10^{-5}\,\mathrm{Pa\,m^{-1}\,s^{-1}}$, $\kappa = 2.624 \cdot 10^{-2}\,\mathrm{W\,m^{-1}\,K^{-1}}$, $\gamma = 1.4$) (Rossing, 2007; Witschas et al., 2010), $z = 1.231$ and $f = 4.934$. Now, a set of Tenti spectra is calculated for atmospheric conditions representing y values between 0 and 1.027. After that, these spectra are fitted with Eq. A.1 in a least square fit procedure to find best fit values for $\mathcal{A}$, σ_R, σ_B and x_B, respectively. For the special case where $y = 0$, $\mathcal{A}$ is restricted to be unity, and therefore, $\mathcal{S}(x, y)$ is only composed of the central Gaussian line with a standard deviation σ_R of the Maxwellian velocity distribution. This approach results in a set of $\mathcal{A}$, σ_R, σ_B and x_B values, depending on y (Fig. A.2, symbols). Now, these values are fitted with appropriate mathematical functions which results in:

$$\mathcal{A}(y) = 0.18526 \cdot \exp\left[-1.31255\,y\right] + 0.07103 \cdot \exp\left[-18.26117\,y\right] + 0.74421 \tag{A.2}$$

$$\sigma_R(y) = 0.70813 - 0.16366\,y^2 + 0.19132\,y^3 - 0.07217\,y^4 \tag{A.3}$$

$$\sigma_B(y) = 0.07845 \cdot \exp\left[-4.88663\,y\right] + 0.80400 \cdot \exp\left[-0.15003\,y\right] - 0.45142 \tag{A.4}$$

$$x_B(y) = 0.80893 - 0.30208 \cdot 0.10898^{y} \tag{A.5}$$

The obtained best fit values for $\mathcal{A}$, σ_R, σ_B and x_B as well as the describing model functions (Eq. A.2 - A.5) are sketched in Fig. A.2.

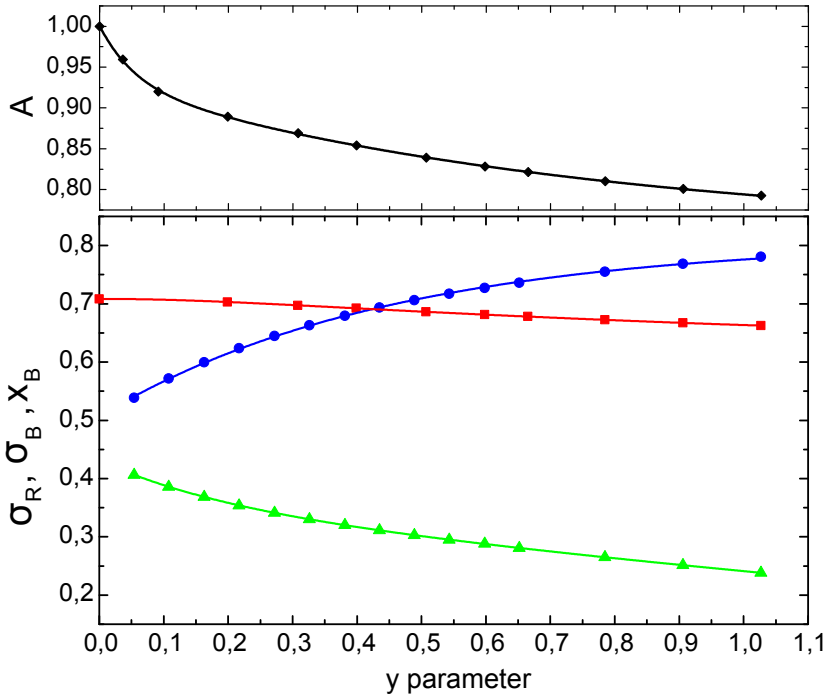

Figure A.2: Integrated intensity $\mathcal{A}$ of the central peak (top, black diamonds), the standard deviation σ_R of the central peak (bottom, red squares), the standard deviation σ_B of the side peaks (bottom, green triangles) and the frequency shift x_B of the side peaks (bottom, blue circles), determined by applying Eq. A.1 to a set of Tenti S6 modeled line shapes ($y = 0 - 1.027$) in a least square fit procedure. The colored lines depict well fitting functions which are given by Eq. A.2 - A.5, respectively.

Applying Eq. A.2 - A.5 to Eq. A.1, an analytical formula for describing SRB line shapes in air valid for $y = 0 - 1.027$ is introduced. It is worth mentioning, that this method can also be performed for other gases, and therefore, gives the possibility to derive an analytical model for SRB line shapes for respective applications.

In conclusion, an easy processable analytical model for the description of SRB line shapes in air was derived. The model is valid for $y = 0 - 1.027$ and the deviations to the Tenti S6 model are smaller than 0.85 % within that region (the prove of this statement is shown in (Witschas, 2011)). Therefore, the model was derived using the dimensionless parameters x and y, it can be applied to various applications with different setup configurations. In near future, the presented model is going to be applied to A2D lidar data aiming to derive the atmospheric temperature over a large range.

A 2 Synoptic tables

Table A.1 summarizes the gas transport coefficients of N_2 and air as they are used for Tenti S6 model line shape calculation within this thesis.

Table A.1: Gas transport coefficients used for Tenti S6 model calculation

		$\mathbf{N_2}$	**Air**
molar mass m	[g mol^{-1}]	28.013	28.850
mass of one molecule M	[kg]	$4.65 \cdot 10^{-26}$	$4.79 \cdot 10^{-26}$
shear viscosity η	[kg m^{-1}s^{-1}]	$(1.79 \cdot 10^{-5})^a$	$(1.846 \cdot 10^{-5})^b$
bulk viscosity η_b	[kg m^{-1}s^{-1}]	$(2.1 \cdot 10^{-5})^c$	$(1.4 \cdot 10^{-5})^c$
thermal conductivity κ	[W m^{-1}K^{-1}]	$(25.5 \cdot 10^{-3})^a$	$(26.24 \cdot 10^{-3})^b$
heat capacity ratio γ		1.4	1.4

[a] Valid at reference temperature 300 K. Taken from Weast and Company (1973).
[b] Valid at reference temperature 300 K. Taken from Rossing (2007).
[c] Valid at reference temperature 297 K, and frequency 1.3 GHz. Taken from measurements (section 3.3.1).

Table A.2 summarizes the conditions used to perform the Tenti S6 model sensitivity analysis (section 2.3.3).

Table A.2: Conditions used for Tenti S6 model sensitivity analysis

y (Eq. 2.14)	**p** [hPa]	**T** [K]	θ	λ [nm]
0.126	300	228.0	180	355.0
0.201	500	251.0	180	355.0
0.376	1000	288.0	180	355.0
0.751	2000	288.0	180	355.0
1.127	3000	288.0	180	355.0

Table A.3 summarizes the experimental conditions of the performed laboratory spontaneous Rayleigh-Brillouin scattering experiments discussed in chapter 3.

Table A.3: Measurement conditions and y-parameter for the SRB experiments

	p [hPa]	**T** [K]	λ [nm]	**y** (Eq. 2.14)	θ	**Figure**
$\mathbf{N_2}$	300 ± 5	298.6 ± 0.6	366.501	0.168 ± 0.005	$90 \pm 0.6°$	3.9 (d)
	2066 ± 31	295.5 ± 0.6	366.514	1.154 ± 0.024	$90 \pm 0.6°$	3.8 (a), 3.9 (a)
	3030 ± 45	296.9 ± 0.6	366.512	1.689 ± 0.036	$90 \pm 0.6°$	3.8 (b)
	3500 ± 53	300.4 ± 0.6	366.490	1.939 ± 0.041	$90 \pm 0.6°$	3.8 (c)
Dry air	300 ± 5	298.0 ± 0.6	366.510	0.163 ± 0.004	$90 \pm 0.6°$	3.9 (e), 3.10 (a)
	504 ± 8	298.0 ± 0.6	366.510	0.273 ± 0.006	$90 \pm 0.6°$	3.10 (b)
	725 ± 11	298.6 ± 0.6	366.523	0.392 ± 0.009	$90 \pm 0.6°$	3.10 (c)
	1040 ± 15	299.4 ± 0.6	366.496	0.560 ± 0.013	$90 \pm 0.6°$	3.10 (d), 3.11 (a)
	2015 ± 30	297.5 ± 0.6	366.533	1.094 ± 0.025	$90 \pm 0.6°$	3.8 (j), 3.9 (b)
	3050 ± 46	297.5 ± 0.6	366.531	1.656 ± 0.037	$90 \pm 0.6°$	3.8 (k)
	3006 ± 45	296.7 ± 0.6	366.456	1.638 ± 0.037	$90 \pm 0.6°$	3.8 (l)
Moist air	1040 ± 15	301.2 ± 0.6	366.496	0.556 ± 0.013	$90 \pm 0.6°$	3.11 (b)

Table A.4 summarizes the experimental conditions of the performed atmospheric spontaneous Rayleigh-Brillouin scattering experiments discussed in chapter 4.

Table A.4: Measurement conditions Schneefernerhaus

Date	Time [UTC]	**p** [hPa]	**T** [K]	λ [nm]	**y** (Eq. 2.14)
26.01.09	19:23	717.5 ± 15	263 ± 1.5	354.890	0.28 ± 0.01
31.01.09	15:30	724.0 ± 15	264 ± 1.5	354.890	0.28 ± 0.01
31.01.09	17:00	722.0 ± 15	262 ± 1.5	354.890	0.28 ± 0.01

Table A.5 summarizes the Fabry-Perot interferometer parameters obtained from measurement and used for atmospheric signal simulation (section 4.2.5).

Table A.5: FPI parameters used for simulating the atmospheric signal

Date	Time [UTC]	$\mathbf{f}_0$ [THz]	Γ_{FSR} [MHz]	**R**	σ_g [MHz]
26.01.09	19:23	844.748320	10934 ± 23	0.664	296
31.01.09	15:30	844.748364	10934 ± 23	0.656	257
31.01.09	17:00	844.748363	10934 ± 23	0.656	270

A 3 Abbreviations and symbols

Abbreviations

A2D	ALADIN airborne demonstrator
ACCD	Accumulation charge coupled device
ADM	Atmospheric dynamics mission
ALADIN	Atmospheric laser Doppler lidar instrument
ALOMAR	Arctic lidar observatory for middle atmosphere research
BRAINS	Brillouin scattering - atmospheric investigation on Schneefernerhaus
CRB	Coherent Rayleigh-Brillouin
DAQ	Data acquisition
DLR	Deutsches Zentrum für Luft- und Raumfahrt
DWD	Deutscher Wetterdienst (German weather service)
DWL	Doppler wind lidar
EADS	European Aeronautic Defence and Space Company
EarthCARE	Earth Clouds, Aerosols, and Radiation Explorer
ESA	European Space Agency
FPI	Fabry-Perot interferometer
FSR	Free spectral range
FWHM	Full width half maximum
HCS	Hänsch-Couillaud stabilization
He-Ne	Helium-Neon
HSRL	High spectral resolution lidar
ILIAD	Impact of line shape on ADM-Aeolus Doppler estimates
Laser	Light amplification by stimulated emission of radiation
Lidar	Light detection and ranging
Nd:YAG	Neodymium-doped Yttrium Aluminum Garnet
PD	Photo diode
PMT	Photo multiplier
PM10	Particulate matter with diameters up to 10 μm
PZT	Piezo-electrical translator
SC	Scattering cell
SHG	Second harmonic generation
SRB	Spontaneous Rayleigh-Brillouin
SRBS	Spontaneous Rayleigh-Brillouin scattering
UBA	Umweltbundesamt (Federal environmental agency)
UFS	Umweltforschungsstation (Environmental research station) Schneefernerhaus
UTC	Coordinated Universal Time
UV	Ultraviolet
WCU	Wang-Chang-Uhlenbeck

Symbols

Symbol	Meaning	Unit
α	Polarizability	C m^2 V^{-1}
α_{tot}	Total absorption coefficient	m^{-1}
$\boldsymbol{E}$	Electric field vector	-
$\boldsymbol{J}$	Collision operator	-
$\boldsymbol{k}$	Wave vector	-
$\boldsymbol{p}$	Dipole moment vector	-
Δf_{FWHM}	Full width at half maximum	Hz
ϵ_0	Vacuum permittivity	$\epsilon_0 = 8.8541 \cdot 10^{-12}$ A s / V m
η	Shear viscosity	kg m^{-1} s^{-1}
η_b	Bulk viscosity	kg m^{-1} s^{-1}
γ	Anisotropy	m^3
Γ_{FSR}	Free spectral range	Hz
κ	Thermal conductivity	W m^{-1} K^{-1}
λ	Wavelength	m
ω	Angular frequency	rad s^{-1}
$\partial\Omega$	Solid angle element	-
$\partial\sigma/\partial\Omega$	Differential scattering cross section	-
$\phi_0(v)$	Maxwell velocity distribution	-
ρ	Density	kg m^{-3}
θ	Scattering angle	$^\circ$
$h_i(\boldsymbol{v}, \boldsymbol{r}, t)$	Dimensionless deviation from equilibrium	-
a	Mean polarizability	-
c	Velocity of light in vacuum	$c = 299792458$ m s^{-1}
c_{p}	Specific heat at constant pressure	kJ kg^{-1} K^{-1}
c_{v}	Specific heat at constant volume	kJ kg^{-1} K^{-1}
c_s	Sound velocity	m s^{-1}
E	Electric field	V m^{-1}
f	Frequency	Hz
h	Planck's constant	$h = 6.625 \times 10^{-34}$ J s
k_B	Boltzmann's constant	$k_B = 1.38065 \times 10^{-23}$ J K^{-1}
M	Mass of a molecule	Kg
m	Molar mass	Kg mol^{-1}
n	Index of refraction	-
p	Pressure	hPa
T	Temperature	K
v_{th}	Thermal velocity	m/s
v_0	Most probable thermal velocity	m/s
y	Ratio of the scattering wavelength to the mean free path of collisions	-

Acknowledgments

I would like to thank everyone whose moral and active support during the last three years has made this thesis possible. I would especially like to express my gratitude to

- Prof. Andreas Tünnermann for accepting me as a nonresident doctoral student in his Institute of Applied Physics at the Friedrich-Schiller-University Jena, for providing excellent support in organizational and subject-specific affairs, and for making very useful suggestions concerning the structure and content of this thesis,
- Prof. Ulrich Schumann for reviewing this thesis, for providing very helpful comments and for energetically supporting my work at DLR during the last four years,
- Oliver Reitebuch for being my mentor, for providing permanent and great support in every respect, and for supplying an enormous amount of helpful suggestions in the course of my research work,
- Prof. Wim Ubachs, Maria Ofelia Vieitez, the entire Laser-Centre group at the free university in Amsterdam, and Prof. Willem van de Water for their marvelous support and the interesting discussions during the laboratory study on spontaneous Rayleigh-Brillouin scattering at the free university in Amsterdam,
- Christian Lemmerz for his readiness of discussion and for being a fabulous next-door neighbor,
- Engelbert Nagel for his unique technical support in performing the BRAINS campaign,
- the Colleagues of the Lidar group at Deutsches Zentrum für Luft- und Raumfahrt and its head Gerhard Ehret for the distinguished working atmosphere,
- Prof. Ulrike Paffrath, Prof. Ines Nikolaus and Uwe Marksteiner, for fruitful discussions concerning LabVIEW programming and the behavior of Fabry-Perot interferometers,
- Martin Endemann, Michael Vaughan, Ad Stoffelen, Anne-Grete Straume, Olivier LeRille, Alain Dabas and Herbert Nett for giving valuable comments within the framework of the ADM-Aeolus Campaigns Progress meetings,
- Thomas Trickl and Hannes Vogelmann from the Institute for Meteorology and Climate Research in Garmisch and the entire Schneefernerhaus-team for planning and conducting the BRAINS campaign, and Ludwig Ries from the Umweltbundesamt for providing the PM10 particle concentration data,
- Jaime Arndt for her help with my English,
- my Bands for showing understanding for my physical and psychological absence during the last three years,
- my grandma Hildegard, my parents Klaus and Dagmar, my brother Florian and the rest of my entire, marvelous family for their emotional, financial and social support,
- and last but not least my girlfriend Michaela for the motivation, vital energy and loving support she has given me.

Curriculum vitae

von **Dipl. Ing. (FH) Benjamin Witschas**
geboren am 08.03.1982 in München

Wissenschaftliche Ausbildung

seit 03/2008	Doktorand am Deutschen Zentrum für Luft- und Raumfahrt (DLR), Oberpfaffenhofen und der Friedrich-Schiller-Universität, Jena. Titel der Doktorarbeit: "Experiments on spontaneous Rayleigh-Brillouin scattering in air"
03/2007–03/2008	Diplomand am Deutschen Zentrum für Luft- und Raumfahrt (DLR), Oberpfaffenhofen. Titel der Diplomarbeit: "Characterization of beam profile and frequency stability of an injection-seeded Nd:YAG laser for a Doppler wind lidar system" (1.3)
03/2008	Diplom physikalischen Technik, Fachrichtung technische Physik, an der Hochschule für angewandte Wissenschaften, München (1.8)
10/2004–03/2008	Studium der physikalischen Technik, Fachrichtung technische Physik an der Hochschule für angewandte Wissenschaften in München
10/2003–10/2004	Studium der Physik an der Ludwig-Maximilians-Universität, München
09/2001–09/2003	Berufsoberschule, München

Technische Ausbildung

09/2006–02/2007	Praxissemester bei der BMW Group, München (Motorapplikation)
09/2001	Gesellenbrief, Industriemechaniker, Fachrichtung Maschinen- und Systemtechnik bei der BMW Group, München
09/1998–09/2001	Berufsausbildung zum Industriemechaniker, Fachrichtung Maschinen- und Systemtechnik bei der BMW Group, München

Martinsried, den 06. April 2011

_____

Benjamin Witschas

Aus Prioritätsgründen wurden Teilergebnisse der vorliegenden Arbeit bereits vorab veröffentlicht:

Publikationen

- **B. Witschas**, M. O. Vieitez, E.-J. van Duijn, O. Reitebuch, W. van de Water, and W. Ubachs, "Spontaneous Rayleigh–Brillouin scattering of ultraviolet light in nitrogen, dry air, and moist air," Applied Optics **49**, 4217–4227 (2010).
- M. O. Vieitez, E.-J. van Duijn, W. Ubachs, **B. Witschas**, A. Meijer, A. S. de Wijn, N. J. Dam, and W. van de Water, "Coherent and spontaneous Rayleigh-Brillouin scattering in atomic and molecular gases, and gas mixtures," Physical Review A **82**, 1–14 (2010).
- **B. Witschas**, "Analytical model for Rayleigh-Brillouin line shapes in air," Applied Optics **50**, 267–270 (2011).

Konferenzbeiträge

- O. Reitebuch, C. Lemmerz, U. Marksteiner, **B. Witschas**, U. Schumann, Z. Li, and Z. Liu, "Pre-Launch validation of the Wind-Lidar on ADM-Aeolus," presented at the 2010 DRAGON 2 Mid Term Results Symposium, Yangshou, Guilin, P. R. CHINA, 17-21 May 2010.
- O. Le Rille, A.-G. Straume, M. O. Vieitez, W. Ubachs, **B. Witschas**, G.-J. Marseille, J. de Kloe, A. Stoffelen, K. Houchi, H. Körnich, and H. Schyberg, "ESA's wind Lidar mission ADM-AEOLUS: On-going scientific activities related to calibration, retrieval and instrument operation," presented at the 25^{th} Int. Laser and Radar Conference (ILRC 2010), St. Petersburg, Russia, 5-9 July 2010.

Poster

- B. Witschas, O. Reitebuch, C. Lemmerz, E. Nagel, "Lidar measurements for the investigation of Rayleigh-Brillouin scattering in the atmosphere," presented at the 2010 DRAGON 2 Mid Term Results Symposium, Yangshou, Guilin, P. R. CHINA, 17-21 May 2010.
- B. Witschas, O. Reitebuch, C. Lemmerz, E. Nagel, M. O. Vieitez, E.-J. van Duijn, W. van de Water, W. Ubachs, "Laser spectroscopy and Lidar measurements for the investigation of Rayleigh-Brillouin scattering (RBS) in air," presented at French-German workshop on occasion of the 50^{th} anniversary of the laser, Berlin, Germany, 5-6 November 2010.

Ehrenwörtliche Erklärung

Ich erkläre hiermit ehrenwörtlich, dass ich die vorliegende Arbeit selbständig, ohne unzulässige Hilfe Dritter und ohne Benutzung anderer als der angegebenen Hilfsmittel und Literatur angefertigt habe. Die aus anderen Quellen direkt oder indirekt übernommenen Daten und Konzepte sind unter Angabe der Quelle gekennzeichnet.

Bei der Auswahl und Auswertung folgenden Materials haben mir die nachstehend aufgeführten Personen in der jeweils beschriebenen Weise unentgeltlich geholfen:

1. Prof. Dr. Andreas Tünnermann als betreuender Hochschullehrer an der Friedrich-Schiller-Universität Jena
2. Dr. Oliver Reitebuch als Mentor am Deutschen Zentrum für Luft- und Raumfahrt, Oberpfaffenhofen
3. Prof. Willem van de Water bei der Anpassung des Tenti S6 codes
4. Dr. Maria Ofelia Vieitez bei der Durchführung und Interpretation der Laborexperimente, aufgeführt in Kapitel 3

Weitere Personen waren an der inhaltlich-materiellen Erstellung der vorliegenden Arbeit nicht beteiligt. Insbesondere habe ich hierfür nicht die entgeltliche Hilfe von Vermittlungs- bzw. Beratungsdiensten (Promotionsberater oder andere Personen) in Anspruch genommen. Niemand hat von mir unmittelbar oder mittelbar geldwerte Leistungen für Arbeiten erhalten, die im Zusammenhang mit dem Inhalt der vorgelegten Dissertation stehen.

Die Arbeit wurde bisher weder im In- noch im Ausland in gleicher oder ähnlicher Form einer anderen Prüfungsbehörde vorgelegt.

Die geltende Promotionsordnung der Physikalisch-Astronomischen Fakultät ist mir bekannt.

Ich versichere ehrenwörtlich, dass ich nach bestem Wissen die reine Wahrheit gesagt und nichts verschwiegen habe.

Martinsried, den 06. April 2011

Benjamin Witschas